Master–THESIS

Black Holes in the Magneticum Pathfinder Simulations

Schwarze Löcher in den Magneticum Pathfinder Simulationen

Ludwigs–Maximilians Universität München
Universitäts-Sternwarte München

vorgelegt von

Lisa Bachmann

München, 2014

Supervisor: PD Dr. Klaus Dolag

Contents

Abstract

Over the last years it has been generally accepted that black holes are essential to understand the formation and evolution of galaxies. But the detailed connection between the growth and evolution of black holes and their host galaxies as well as the observed, fundamental scaling relations between them are currently only poorly understood. By following the growth of black holes within cosmological simulations, one can clarify open questions like how black holes and their host galaxies evolve during time and how this is connected to the activity of Active Galactic Nuclei (AGN). Thus, AGN trigger mechanisms can be studied.

In this thesis the Magneticum Pathfinder simulations (Dolag et al. in prep.) are analysed quantitatively and qualitatively. They have been performed using the SPH (smoothed particle hydrodynamics) code P-GADGET3, which is an updated version of the code GADGET-2 by Springel (2005). Besides detailed models for star formation and supernova feedback (Tornatore et al., 2007) it includes an extended black hole model based on Springel et al. (2005).

Resolving galaxies and AGN feedback in cosmological simulations allows challenging the understanding of galaxy formation and its connection to black hole physics. In this thesis the reliability of the current black hole model will be demonstrated by comparing the simulation with observations, i.e. the relation between the black hole mass and the stellar mass, the M-σ-relation, the stellar mass functions or the luminosity functions at various redshifts.

The simulations in general are very successful in reproducing these relations. Thus it is possible to investigate in detail how black holes grow, how their luminosity evolves over cosmic time and what their environment looks like. It will be shown that galaxy mergers play an important role for the black hole growth and thus for the appearance of AGN.

In the last section, AGN feedback and black hole accretion is studied in more detail. Therefore, critical parameters and how to model them are examined in a detailed parameterstudy. Thus the simulation could be improved by implementing a radiative efficiency of the AGN feedback, which depends on the black hole mass. It is also demonstrated that an even more detailed description of black hole accretion and AGN feedback should be implemented in the future to further improve the underlying black hole model.

1 Introduction

The idea of black holes already came up in 1795 when Laplace conjectured that objects might exist, which are so compact, that even light can not escape. The reason is that if you decrease the radius of an object with mass M, the escape velocity v_{esc} increases. v_{esc} is the velocity which is necessary to escape from the gravitational field of the object:

$$v_{\mathrm{esc}} = \sqrt{\frac{2GM}{r}}. \tag{1}$$

The Schwarzschild radius r_{S} is defined as the radius where v_{esc} equals the speed of light c, so that from equation (1) follows:

$$r_{\mathrm{S}} = \frac{2GM}{c^2}. \tag{2}$$

Consequently, even light can not escape if $r < r_{\mathrm{S}}$. This means that such objects are invisible. Thus, they are called black holes.

Black holes can be the products of the complete gravitational collapse of stars (Hoyng 2006). Thus, one would expect that the masses of black holes should be of the same order of magnitude than the masses of stars. Because of that their mass should be smaller than $\sim 10^2 M_{\odot}$. Indeed stellar mass black holes can be observed indirectly in binary systems, where they interact gravitationally with other objects.

Nevertheless, there is another type of black holes. They are called supermassive black holes (SMBHs) having masses between $\sim 10^6 M_{\odot}$ and $\sim 10^{10} M_{\odot}$. They are generally located in the centers of galaxies. The idea of SMBHs was driven forward by Kormendy & Richstone (1995). Subsequently it was constrained by many authors, e.g. Bender et al. (1996) or Magorrian et al. (1998), who measured the dynamics in the innermost parts of galaxies. The latter found that galaxy properties are correlated with the black hole masses.

In recent years it was possible to fill the gap between stellar mass black holes and SMBHs with intermediate mass black holes (IMBHs). They are located in the centers of globular clusters and dwarf galaxies and have been observed amongst others by Gebhardt et al. (2005), Noyola et al. (2010) and Lützgendorf et al. (2011). This is an important hint for the origin of SMBHs, which is still not understood. Thus, SMBHs might have evolved out of stellar mass black holes that have merged with each other and have accreted a huge amount of surrounding matter.

Further puzzling observations concern AGN, which are very bright sources in the centers

Figure 1: This colour composite image of Centaurus A was taken from ESO: www.eso.org/public/images/eso0903a

of galaxies. The engine, which delivers such a huge amount of energy, has to be a black hole, because the mass remaining in the object due to the limited efficiency leads to a Schwarzschild radius of the same order of magnitude as the size of the central source. Thus, the energy can not originate from nuclear fusion. Further details have been reviewed by Schneider (2006).

The energy output occurs in the form of two jets. One example for the observation of jets is the galaxy Centaurus A (e.g. Alvarez et al. 2000). Figure 1 shows a colour composite image of Centaurus A. It clearly visualizes the jets of this galaxy.

In general there are different types of AGN. Due to the unified model of AGN, which was reviewed amongst many others by Urry & Padovani (1995), Schneider (2006) and Frank et al. (1992), all AGN have the same structure, but they are seen from different points of view. This is depicted in figure 2. Seyfert galaxies are spiral galaxies hosting an AGN. They have first been observed by Seyfert (1943). Very broad lines can be observed for Seyfert 1 (Sey 1) galaxies, while Seyfert 2 (Sey 2) galaxies have only narrow lines.

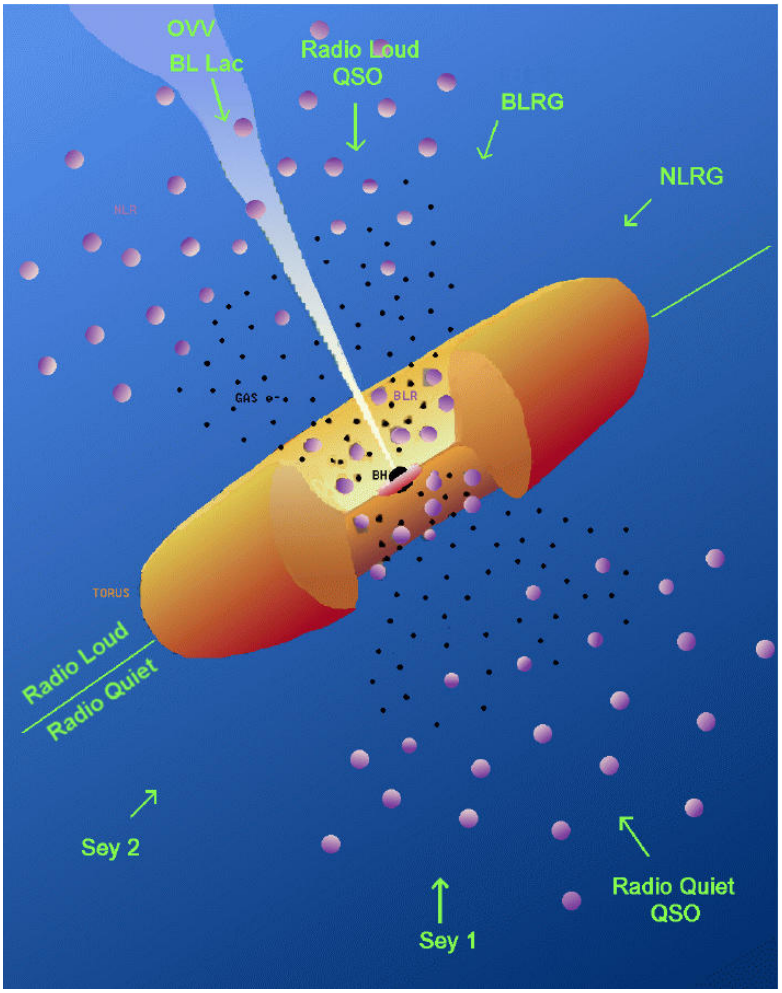

Figure 2: This sketch depicts the unified model of AGN. It was taken from http://www.cv.nrao.edu/course/astr534/ExtraGalactic.html. They have adopted the figure of Urry & Padovani (1995).

Due to the unified model there is a torus around the black hole. Between the torus and the black hole there is the so-called broad line region (BLR), in which the gas moves faster than in the outer parts and thus broader emission lines can be observed. Whether broad lines can be seen or not depends on whether the observer sees the broad line region or only the so-called narrow line region (NLR), which is further away from the torus. In addition to Seyfert galaxies, there are radio loud elliptical galaxies, with (BLRG) or without (NLRG) broad lines. The brightest AGN are quasars (QSO), because here the observer looks directly onto the jet. Thus, they can be observed at very high redshifts. They can also be radio loud or radio quiet. There is another class of AGN called BL Lac objects. In contrast to quasars they have only very faint to no emission lines.

It is assumed that the appearance of broad emission lines depends on whether the central region is obscured by dust or not. Thus, AGN contain a torus of dust surrounding the black hole. In recent studies (e.g. Hönig et al., 2013) the obscuration by dust could be observed by measuring the mid-infrared emission on parsec-scales. Nevertheless, they could not find the toroidal structure predicted by the unified model. Actually it can not be excluded that the dust is near the black hole by chance.
In contrast to the unified model there are studies, e.g. by Hopkins et al. (2008), which claim the existence of two different modes: the radio-mode and the quasar-mode. In this model only the accretion rate and the mass of the black hole decide whether a black hole is a quasar or not. Hirschmann et al. (2013) showed that the Magneticum Pathfinder simulations are consistent with this model.
The same simulations were used in this thesis. They are a set of cosmological simulations and will be described in section 3. The particles in the simulations used in this study have masses up to $\sim 10^9 M_\odot$. Thus, the black holes have to be seeded as soon as the resolution allows it. The black hole model used is based on the studies by (Springel et al., 2005). Once the black holes are seeded they grow by accreting gas and by merging with each other. Furthermore, a feedback model is implemented.
This offers the possibility to analyse the evolution of black holes and to investigate the main trigger mechanisms for AGN activity. Furthermore, the connection of black holes and their host galaxies as well as the importance of the AGN feedback and the accretion model can be studied.
This thesis is structured as follows: In chapter 2 the theoretical background of black hole physics will be explained in general. Chapter 3 gives an overview of the Magneticum simulations. The black hole model is described in more detail. In chapter 4 AGN statistics are studied, whereas chapter 5 contains a more detailed analysis of the galaxies in a high resolved run of the Magneticum simulations. They are classified and dynamically analysed. In chapter 6 black holes were traced back in time to study AGN trigger mechanisms. Finally the parameterstudy in chapter 7 shows the impact of different parameters onto the simulation. This is necessary to improve the black hole model.

2 Black Holes from a Relativistic Point of View

Because of the huge gravitational forces a relativistic point of view is necessary to understand black hole physics. All equations used in this section were taken from Raychaudhuri et al. (1992), Hoyng (2006) and Weinberg (1972). In the theory of relativity time and space coordinates are not independent from each other like in the physics of Galileo and Newton. But Einstein postulated a new invariant

$$\mathrm{d}s^2 = g_{\mu\nu}\mathrm{d}x^\mu \mathrm{d}x^\nu \tag{3}$$

containing the metric tensor $g_{\mu\nu}$ which represents the gravitational field. $\mathrm{d}s^2$ is called the line element. It is the interval between two events x^α and $x^\alpha + \mathrm{d}x^\alpha$. The spacetime is curved whereas the relation between the total curvature

$$R = g^{\nu\mu}R_{\mu\nu} \tag{4}$$

and the energy density is described by Einstein's field equations

$$R_{\mu\nu} - \frac{1}{2}g_{\mu\nu}R = -\frac{8\pi G}{c^2}T_{\mu\nu}, \tag{5}$$

where

$$G_{\mu\nu} = -\frac{8\pi G}{c^2}T_{\mu\nu} \tag{6}$$

is the Einstein tensor and

$$R_{\mu\nu} = \Gamma^\alpha_{\mu\alpha,\nu} - \Gamma^\alpha_{\mu\nu,\alpha} - \Gamma^\alpha_{\mu\nu}\Gamma^\beta_{\alpha\beta} + \Gamma^\alpha_{\mu\beta}\Gamma^\beta_{\nu\alpha} \tag{7}$$

is the Ricci tensor. It can be derived with the Christoffel symbols

$$\Gamma^\mu_{\nu\sigma} = \frac{1}{2}g^{\mu\lambda} = (g_{\lambda\nu,\sigma} + g_{\lambda\sigma,\nu} - g_{\nu\sigma,\lambda}). \tag{8}$$

Albert Einstein himself wrote that general relativity means that

'gravity is not a foreign and physical force transmitted through space and time. It is a manifestation of the curvature of spacetime.' (Einstein 1955)

In the following subsections black holes are described relativistically. They have three properties: Mass, spin and charge. The Schwarzschild metric contains only the mass, whereas the Kerr metric takes the mass and the spin into account. These two cases are

described in section 2.1 and 2.2. In this thesis the charge will not be considered, for this one would have to use the Kerr-Newman metric describing a black hole with mass, spin and charge.

2.1 The Schwarzschild Black Hole

Equation (3) can be simplified using spherical coordinates $x^0 = ct$, $x^1 = r$, $x^2 = \theta$ and $x^3 = \phi$ as follows: The time invariance and the spherical symmetry imply

$$g_{0i} = g_{r\theta} = g_{r\phi} = g_{\theta\phi} = 0. \tag{9}$$

So only the diagonal components remain. Thus, the metric is of the form

$$\mathrm{d}s^2 = Ac^2\mathrm{d}t^2 - B\mathrm{d}r^2 - Cr^2\mathrm{d}\theta^2 - Dr^2\sin^2\theta\mathrm{d}\phi^2. \tag{10}$$

$C = D$ because of the spherical symmetry of the sphere $\mathrm{d}l^2 = r^2(C\mathrm{d}\theta^2 + D\sin^2\theta\mathrm{d}\phi^2)$. You can choose $C = 1$ by using appropriate units. Then the components of the metric tensor are

$$g_{00} = e^{2\nu}, \quad g_{11} = -e^{2\lambda}, \quad g_{22} = -r^2 \quad and \quad g_{33} = -r\sin^2\theta, \tag{11}$$

where ν and λ depend on r.
To derive the Schwarzschild metric one needs two components of the Einstein tensor,

$$G_{00} = -\frac{e^{2\nu}}{r^2}\frac{\mathrm{d}}{\mathrm{d}r}r(1 - e^{-2\lambda}) = 0 \tag{12}$$

and

$$G_{11} = \frac{1}{r^2}(e^{2\lambda} - 1) - \frac{2\nu'}{r} = 0. \tag{13}$$

From equation (12) we get

$$e^{2\lambda} = \frac{1}{1 - \frac{b}{r}}, \tag{14}$$

where b is a constant. By inserting equation (14) into equation (13) we find

$$e^{2\nu} = A\left(1 - \frac{b}{r}\right), \tag{15}$$

where $A = 1$ because the Schwarzschild metric must be the Lorentz metric for $r \to \infty$ (Hoyng 2006). From the weak field approximation (e.g. Raychaudhuri et al. 1992) you

get $g_{00} = 1 + 2\phi$ and thus $b = r_\mathrm{S}$. So the line element of the Schwarzschild metric is

$$\mathrm{d}s^2 = \left(1 - \frac{r_\mathrm{S}}{r}\right) c^2 \mathrm{d}t^2 - \frac{\mathrm{d}r^2}{1 - \frac{r_\mathrm{S}}{r}} - r^2(\mathrm{d}\theta^2 + \sin^2\theta \mathrm{d}\phi^2). \tag{16}$$

To derive the binding energy and the angular momentum of a test particle in the gravitational field of the black hole one can use the formalism of Lagrange. For $\theta = \pi/2$ and $\ddot{r} = \dot{r} = 0$ (circular orbits) the Lagrangian corresponding to the Schwarzschild metric is

$$L = \left(1 - \frac{r_\mathrm{S}}{r}\right) c^2 \dot{t}^2 - r^2 \dot{\phi}^2. \tag{17}$$

Using the Euler Lagrange equations for t and ϕ one finds

$$\left(1 - \frac{r_\mathrm{S}}{r}\right) c\dot{t} := e = \text{const} \quad \text{and} \quad r^2 \dot{\phi} := h = \text{const}, \tag{18}$$

where e is the binding energy in units of $m_0 c^2$ (m_0 is the mass of the test particle) and h is the angular momentum. Inserting the equations (18) and using $L = 1$ for massive particles we can deviate an expression for e:

$$e^2 = \left(1 - \frac{r_\mathrm{S}}{r}\right) \left(\frac{h^2}{r^2} + 1\right). \tag{19}$$

A circular orbit is only possible at the maximum

$$\frac{r_+}{r_\mathrm{S}} = \frac{h^2}{r_\mathrm{S}^2} \left(1 + \sqrt{1 - 3\frac{r_\mathrm{S}^2}{h^2}}\right) \tag{20}$$

(Hoyng 2006). For $r = r_+$ we have

$$\frac{h^2}{r^2} = \frac{1}{2(r/r_\mathrm{S}) - 3} \tag{21}$$

$$\Rightarrow e^2 = \left(1 - \frac{r_\mathrm{S}}{r}\right) \left(\frac{1}{2(r/r_\mathrm{S}) - 3} + 1\right). \tag{22}$$

From equation (20) we know that $r = 3r_\mathrm{S}$ is the smallest possible radius. Now the difference between the binding energy at $r = \infty$ and $r = r_+ = 3r_\mathrm{S}$ can be calculated:

$$e(\infty) m_0 c^2 - e(3r_\mathrm{S}) m_0 c^2 \approx 0.057 m_0 c^2. \tag{23}$$

The value 0.057 is the radiative efficiency for a non-rotating black hole (e.g. Novikov & Thorne 1973). It will be mentioned later and will play a major role in this thesis.

2.2 The Rotating Black Hole

In general the assumptions (9) are not fulfilled because black holes are rotating. The following expressions are taken from Bardeen et al. (1972) who have described this scenario. In contrast to non-rotating black holes there has to be an additional component $g_{02} = g_{20}$ in the metric:

$$\mathrm{d}s^2 = -e^{2\nu}\mathrm{d}t^2 + e^{2\psi}(\mathrm{d}\phi - \omega\mathrm{d}t)^2 + e^{2\mu_1}\mathrm{d}r^2 + e^{2\mu_2}\mathrm{d}\theta^2. \tag{24}$$

The metric used for the description of rotating black holes is called the Kerr metric. Its components depend on the radius r and the spin a. For $\theta = \pi/2$ one can write the line element of the Kerr metric as

$$\mathrm{d}s^2 = \frac{r^2\Delta}{A}\mathrm{d}t^2 + \frac{A}{r^2}(\mathrm{d}\phi - \omega\mathrm{d}t)^2 + \frac{r^2}{\Delta}\mathrm{d}r^2 + r^2\mathrm{d}\theta^2 \tag{25}$$

with

$$\Delta \equiv r^2 - 2Mr + a^2, \tag{26}$$

$$A = (r^2 + a^2)^2 - a^2\Delta \tag{27}$$

and

$$\omega = \frac{2Mar}{A}. \tag{28}$$

The gravitational binding energy for the Kerr metric can be written down by using the dimensionless parameters $r_* = r/M$ and $a_* = a/M$ like Novikov & Thorne (1973):

$$e = \left(1 - \frac{2}{r_*} + \frac{a_*}{r_*^{3/2}}\right)\left(1 - \frac{3}{r_*} + \frac{2a_*}{r_*^{3/2}}\right)^{-1/2}. \tag{29}$$

This shows that the radiative efficiency strongly depends on the spin.
Bardeen et al. (1972) showed that the marginally stable orbit is

$$r_{\mathrm{ms}}/M = 3 + Z_2 \mp [(3 - Z_1)(3 + Z_1 + 2Z_2)]^{1/2} \tag{30}$$

with

$$Z_1 \equiv 1 + (1 - a_*^2)^{1/3}[(1 + a_*)^{1/3} + (1 - a_*)^{1/3}] \quad \text{and} \quad Z_2 \equiv (3a_*^2 + Z_1^2)^{1/2}. \tag{31}$$

The radiative efficiency can be calculated analogue to equation (23). For $a_* \to 1$ it converges to its theoretical upper limit 0.42.

3 The Magneticum Pathfinder Simulations

The cosmological simulations used in this thesis are called Magneticum Pathfinder simulations (Dolag et al., in prep.), subsequently called the Magneticum simulations. They are based on the code P-GADGET3 which is the newest version of the parallel TreeSPH code GADGET-2 by Springel (2005). In this section it is explained what cosmological simulations are in general. Furthermore, the Magneticum simulations and their black hole module will be described.

3.1 Cosmological Simulations

In general, the setting of a cosmological simulation is a box with periodic boundary conditions. Inside this box a specific cosmology evolves. In the Magneticum simulations the ΛCDM (Λ cold dark matter) cosmology is adopted as described e.g. by Peebles (1993). Λ is the cosmological constant. It was introduced by Einstein to modify the field equations (equation 5) to avoid a negative pressure of the world matter:

$$R_{\mu\nu} - \frac{1}{2} g_{\mu\nu} R - \Lambda g_{\mu\nu} = -\frac{8\pi G}{c^2} T_{\mu\nu}. \tag{32}$$

In the following equations $c = 1$ is used. The equations of motion for the accelerated expansion of the universe are

$$\frac{\ddot{a}}{a} = -\frac{4}{3}\pi G(\rho_\mathrm{b} + 3p_\mathrm{b}) + \frac{\Lambda}{3} \tag{33}$$

and

$$\left(\frac{\dot{a}}{a}\right)^2 = \frac{8}{3}\pi G\rho_\mathrm{b} \pm \frac{1}{a^2 R^2} + \frac{\Lambda}{3}, \tag{34}$$

where $a = (1+z)^{-1}$ is the scale factor and R is a constant corresponding to the curvature. ρ_b and p_b are the density and the pressure of baryonic matter. The Hubble parameter H is defined as the expansion rate of the universe:

$$H(t) = \frac{\dot{a}(t)}{a(t)}. \tag{35}$$

At $z = 0$ it has the value H_0, which is called the Hubble constant. In simulations the calculations are made in co-moving units. Thus the box size is constant. Physical units can be calculated by dividing the internal unit by $1 + z$. In the Magneticum simulations the value $h = 0.7$ is used for the Hubble constant $H_0 = 100h$ km s^{-1} Mpc^{-1}.

Equation (34) can also be written by using the three cosmological parameters Ω, Ω_R and Ω_Λ. The first one is the density parameter

$$\Omega = \frac{8\pi G\rho_0}{3H_0^2} \tag{36}$$

and the second one the curvature parameter

$$\Omega_R = \frac{1}{(a_0 H_0 R)^2}. \tag{37}$$

The third parameter depends on Λ and describes the dark energy

$$\Omega_\Lambda = \frac{1}{3H_0^2}. \tag{38}$$

Thus, with the equations (35) - (38) one can write equation (34) as:

$$H^2 = H_0^2[\Omega(1+z)^3 + \Omega_r(1+z)^2 + \Omega_\Lambda]. \tag{39}$$

A cosmological box has a certain initial number of particles, whereas there are different particle types: Dark matter, gas, stars and black holes.
The GADGET-2 code contains two basic principles, which have been described by Springel (2005):

- **Gravitation:** To calculate the gravitational forces an N-body problem has to be solved. Therefore Springel (2005) uses the TreePM method, which is a combination of a tree method and a particle mesh (PM) method. The gravitational potential is splitted in Fourier space into a long-term part, which is calculated with mesh-based Fourier methods, and a short-term part, for which the tree method is used.

- **Hydrodynamics:** In smoothed particle hydrodynamics (SPH) continuous fluid quantities like the gas density can be calculated by explicitly solving the hydrodynamical equations, e.g. the equation of continuity and the Euler equations, which describe the conservation of mass, momentum and energy.

3.2 Boxes and Resolutions of the Magneticum Simulations

The different Magneticum simulations have box sizes from $(12\ \mathrm{Mpc})^3$ (Box6) up to $(896\ \mathrm{Mpc})^3$ (Box1) with different resolutions: medium (mr), high (hr), ultra high (uhr)

and extremely high (xhr). In this thesis three boxes have been used:

- **Box3 hr** was used for the statistical analysis in section 4. It is large enough to get a statistically representative amount of black holes. It also consists of more massive black holes than Box4 and thus allows investigating the high mass end in the luminosity functions.
- **Box4 uhr** was used in section 5 and 6. With that resolution it is possible to resolve galaxies. So they can be morphologically classified. By tracing black holes back in time it can be studied how merger events and gas accretion contribute to AGN activity.
- **Box4 hr** was used in section 7 to perform several test runs in an appropriate amount of time. The size of the box is large enough to compare the simulations with fundamental observed relations like the relation between the black hole mass and the stellar mass of the bulge.

Table 1 summarizes the most important properties of these simulations. They were taken from Hirschmann et al. (2013).

	V/(Mpc/h)^3	initial particle number	$M_{\mathrm{dm}}/M_\odot$	$M_{\mathrm{gas}}/M_\odot$	$M_{\mathrm{stars}}/M_\odot$
Box3 hr	128^3	$2 \cdot 576^3$	$6.9 \cdot 10^8$	$1.4 \cdot 10^8$	$3.5 \cdot 10^7$
Box4 uhr	48^3	$2 \cdot 576^3$	$3.6 \cdot 10^7$	$7.3 \cdot 10^6$	$1.8 \cdot 10^5$
Box4 hr	48^3	$2 \cdot 216^3$	$6.9 \cdot 10^8$	$1.4 \cdot 10^8$	$3.5 \cdot 10^7$

Table 1: Important properties of the simulations used in this study. V is the volume and M_{dm}, M_{gas} and M_{stars} are the initial masses of one dark matter, gas and star particle.

3.3 Black Holes in Magneticum

This section focusses on the black hole module used in the Magneticum simulations. It was introduced by Springel et al. (2005) and improved by Fabjan et al. (2010). To simulate black holes one has to consider four mechanisms:

- black hole seeding,
- gas accretion,
- black hole mergers and

- AGN feedback.

They will be described in the following subsections.

3.3.1 Black Hole Seeding

In the Magneticum simulations a group of the nearest star particles is identified using the so called FoF (friends-of-friends) algorithm (Dolag et al. 2009, Springel et al. 2001). When the mass of the FoF group exceeds a certain value, a black hole is seeded in the potential minimum of the FoF group.
In the simulations used in section 4 and 5 the minimum stellar mass is $10^{10} M_\odot/h$ and the seeding mass of the black holes is $2 \cdot 10^5 M_\odot/h$ (Hirschmann et al. 2013).
One might wonder why this does not lie on the observed relation between the black hole mass and the stellar mass M_* of the bulge. This relation was observed by many authors, amongst others by McConnell & Ma (2013). They found

$$\log_{10}(M_{\rm bh}/M_\odot) = 8.46 + 1.05 \log_{10}(M_*/10^{11} M_\odot). \tag{40}$$

The reason for the low black hole seeding mass is that in the simulations a galaxy evolves without a black hole until it is seeded. In reality, the black holes do not appear immediately. Thus, they have already accreted matter and influenced the surrounding medium. This can be compensated with a low seeding mass. After the seeding, a black hole grows until it reaches the $M_{\rm bh} - M_*$-relation.
To compensate the fact that a black hole is too light during this process, it has two masses: the real mass and the dynamical mass. The real mass is used for the accretion process, whereas the dynamical mass is used to calculate the gravitational forces as long as it is larger than the real mass.
The black holes are treated as collision-less sink particles like in other hydrodynamical simulations including black holes (e.g. Springel et al. 2005 or Di Matteo et al. 2008). The difference between the Magneticum simulations and other simulations is that the black holes are not repositioned in the potential minimum of their host galaxy once they are seeded (Hirschmann et al. 2013).

3.3.2 Black Hole Accretion

The accretion model used in the Magneticum simulations is based on the Bondi-Hoyle-Lyttleton model (Hoyle & Lyttleton 1939, Bondi & Hoyle 1944, Bondi 1952).

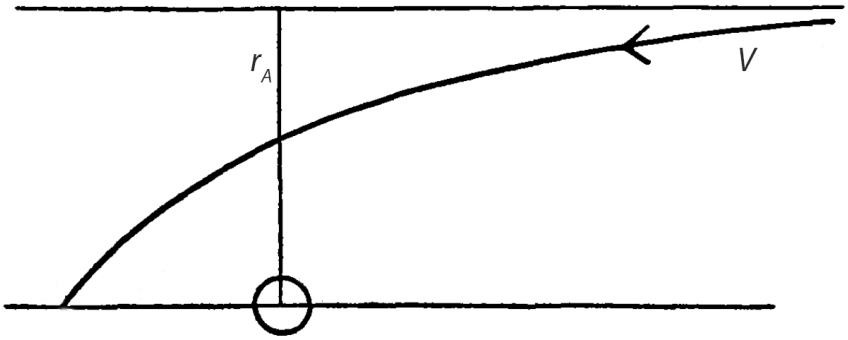

Figure 3: Sketch of the accretion model of Hoyle and Lyttleton (1939)

Hoyle & Lyttleton (1939) were the first pioneers of this accretion model. They calculated the accretion rate $\dot{M}$ of a star. Figure 3 shows a sketch of their accretion model. It was copied directly from Hoyle & Lyttleton (1939), where the notation used in this thesis was inserted. They argued that the number of accreted particles per second is the number of particles crossing an area bound by a circle of radius r_{A}. This accretion radius is perpendicular to the velocity v of the test particles and can be expressed by

$$r_{\mathrm{A}} = \frac{2GM}{v^2}. \tag{41}$$

Thus, Hoyle & Lyttleton (1939) concluded

$$\dot{M} = \pi r_{\mathrm{A}}^2 \rho v = \frac{4\pi G^2 M^2 \rho}{v^3}, \tag{42}$$

where ρ is the gas density.
A few years later Bondi & Hoyle (1944) noticed that forces due to gas pressure have to be considered. So they multiplied equation (42) by a factor α_{HL}. With numerical calculations they found $\alpha_{\mathrm{HL}} = 1.25$ and concluded

$$\dot{M} = \pi \alpha_{\mathrm{HL}} r_{\mathrm{A}}^2 \rho v = \frac{2.5\pi G^2 M^2 \rho}{v^3}. \tag{43}$$

Later Bondi (1952) calculated an accretion rate considering the effects of pressure. Therefore he assumed that the gas is ideal and adiabatic. The calculation is based on the equation of continuity

$$4\pi r^2 \rho v = \mathrm{const} = \dot{M} \tag{44}$$

and on Bernoulli's equation

$$\frac{v^2}{2} + \int_{p_\infty}^{p} \frac{\mathrm{d}p}{\rho} - \frac{GM}{r} = \mathrm{const}(= 0). \tag{45}$$

The constant equals zero if the boundary conditions are at infinity. With

$$\frac{p}{p_\infty} = \left(\frac{\rho}{\rho_\infty}\right)^\gamma \tag{46}$$

one can write equation (45) as

$$\frac{v^2}{2} + \frac{\gamma}{\gamma - 1}\frac{p_\infty}{\rho_\infty}\left[\left(\frac{\rho}{\rho_\infty}\right)^{\gamma-1} - 1\right] = \frac{GM}{r}, \tag{47}$$

where γ is the adiabatic index. At that point Bondi (1952) introduces three non-dimensional variables x, y and z to replace r, v and ρ:

$$r = \frac{xGM}{c_\mathrm{s}^2}, \tag{48}$$

$$v = yc_\mathrm{s}, \tag{49}$$

$$\rho = z\rho_\infty. \tag{50}$$

c_s is the sound speed and ρ_∞ the density at infinity. Then one can write equation (44) as

$$\dot{M} = \frac{4\pi\lambda G^2 M^2 \rho_\infty}{c_\mathrm{s}^3} \tag{51}$$

with $x^2yz = \lambda$. Using

$$c_\mathrm{s}^2 = \gamma\frac{p_\infty}{\rho_\infty} \tag{52}$$

equation(47) can be written as

$$\frac{1}{2}y^2 + \frac{z^{\gamma-1} - 1}{\gamma - 1} = \frac{1}{x}. \tag{53}$$

From equation (51) and (53) Bondi (1952) calculated the maximum value of λ:

$$\lambda_c = \left(\frac{1}{2}\right)^{\frac{\gamma+1}{2(\gamma-1)}} \left(\frac{5-3\gamma}{4}\right)^{-\frac{5-3\gamma}{2(\gamma-1)}}. \tag{54}$$

Thus, the accretion rate depends on γ. In our simulations $\gamma = 5/3$ was used. This would mean

$$\dot{M} = \pi G^2 M^2 \frac{\rho_\infty}{c_\mathrm{s}^3}. \tag{55}$$

This defines the Bondi-Hoyle radius as it is mentioned for example by Booth & Schaye (2009) and Edgar (2004):

$$r_\mathrm{B} = \frac{GM_\mathrm{bh}}{c_\mathrm{s}^2}. \tag{56}$$

In the literature different values for γ have been used. For the interstellar medium with $\gamma = 1.4$ (Frank et al. 1992) equation (51) would become $\dot{M} = 2.5\pi G^2 M^2 \frac{\rho_\infty}{c_\mathrm{s}^3}$. In contrast to that Bondi (1952) used the value $\gamma = 3/2$ and concluded

$$\dot{M} = 2\pi G^2 M^2 \frac{\rho_\infty}{c_\mathrm{s}^3}. \tag{57}$$

According to Bondi (1952) this is the temperature-limited case in contrast to the velocity-limited case given by equation (43). He concluded that the real accretion rate had to be an interpolation between these two cases which might be

$$\dot{M} = \frac{2\pi G^2 M^2 \rho_\infty}{(v^2 + c_\mathrm{s}^2)^{3/2}}. \tag{58}$$

This equation would contain dynamical effects as well as the effects of pressure. Later Shima et al. (1985) showed that the best interpolation is different by the factor 2:

$$\dot{M} = \frac{4\pi G^2 M^2 \rho_\infty}{(v^2 + c_\mathrm{s}^2)^{3/2}}. \tag{59}$$

Therefore they introduced the effective accretion radius r_Ae:

$$\dot{M} = \pi r_\mathrm{Ae} \rho_\infty v. \tag{60}$$

Combining equation (60) with equation (58), which is the equation suggested by Bondi (1952), gives

$$r_\mathrm{Ae} = \frac{2^{1/2} \cdot GM}{(v^2 + c_\mathrm{s}^2)^{3/4} \cdot v^{1/2}}. \tag{61}$$

Shima et al. (1985) argued that $r_{\mathrm{Ae}}/r_{\mathrm{A}}$ had to approach unity for large Mach numbers M_∞ at infinity. From the equations (41) and (61) one gets

$$\frac{r_{\mathrm{Ae}}}{r_{\mathrm{A}}} = 2^{-1/2}\left(\frac{M_\infty^2}{M_\infty^2+1}\right)^{3/4}. \tag{62}$$

Thus, Shima et al. (1985) concluded that equation (62) had to be multiplied by $2^{1/2}$. This explains equation (59). For $v = c_{\mathrm{s}}$ equation (61) becomes the Bondi radius as given by Choi et al. (2012):

$$r_{\mathrm{B}} = \frac{2GM_{\mathrm{bh}}}{c_{\mathrm{s}}^2+v^2}. \tag{63}$$

Consequently the Bondi radius is the threshold between subsonic and supersonic flows. Equation (59) is the origin of the formula for the Bondi accretion rate $\dot{M}_B$ used in the GADGET code:

$$\dot{M}_{\mathrm{B}} = \frac{4\pi\alpha G^2 M_{\mathrm{bh}}^2\rho}{(c_{\mathrm{s}}^2+v^2)^{3/2}}. \tag{64}$$

In the simulation v is the relative velocity between the black hole and its surrounding gas particles and α is a boost factor introduced by Springel et al. (2005). Booth & Schaye (2009) verify this parameter by two arguments. The first is the uncertainty in the estimation of the temperature of the accreted gas and thus of the sound speed c_{s} of the interstellar medium (ISM). The reason for that is the limited resolution but also the uncertainty in the physics of the cold-phase of the ISM. Booth & Schaye (2009) argue that the temperature might be overestimated which justifies large values of α. Their second argument for introducing α is that the Jeans length is not resolved in low-resolution simulations. The Jeans length λ_{J} is the length at which pressure and gravitational forces are in equilibrium (Peebles 1993). Thus, the gravitational growth time $t_{\mathrm{g}} \sim (G\rho_0)^{-1/2}$ is comparable to the time $t_{\mathrm{J}} \sim \lambda_{\mathrm{J}}/c_{\mathrm{s}}$ for a pressure wave to move across the Jeans length (Peebles 1993). The Jeans mass M_{J} is the mass within a sphere of diameter λ_{J} and density ρ_0:

$$M_{\mathrm{J}} = \frac{4\pi}{3}\rho_0\left(\frac{1}{2}\lambda_{\mathrm{J}}\right)^3 \tag{65}$$

(Binney & Tremaine 2008). So the Jeans length can be expressed as

$$\lambda_{\mathrm{J}} \sim \sqrt{\frac{c_{\mathrm{s}}^2}{G\rho}} \sim \frac{GM_{\mathrm{J}}}{c_{\mathrm{s}}^2}. \tag{66}$$

The equations (56) and (66) show that for $M_{\rm bh} > M_{\rm J}$ the Bondi radius is resolved if the Jeans length is resolved. Thus, the above argument that the Jeans length is not resolved at low resolutions leads to an underestimation of the density at the Bondi radius.
In most simulations (e.g. Springel et al. 2005 or Di Matteo et al. 2008) as well as in the simulations analysed in this study a constant value of $\alpha = 100$ was used for the accretion factor. Nevertheless, it is worth mentioning that Booth & Schaye (2009) concluded from the above arguments that it would be better to choose α as a function of the density:

$$\alpha = f(n) = \begin{cases} 1, & \text{if } n_{\rm H} < n_{\rm H}^*, \\ \left(\frac{n_{\rm H}}{n_{\rm H}^*}\right)^{\beta}, & \text{otherwise} \end{cases} \tag{67}$$

where $n_H^* = 0.1\mathrm{cm}^{-3}$. $n_{\rm H}^*$ is the threshold density above which a cold interstellar gas phase forms. This guarantees that the accretion is described correctly when the resolution allows it and that the accretion rate is increased artificially by α when not.
Although this makes the accretion more realistic rather than using a constant α there is still one free parameter. β is also an empirical parameter. The values of both parameters are not motivated physically and up to now nobody has shown the origin of these parameters. Nevertheless, this model is not relevant for large cosmological simulations because of the limited resolution due to the current computational power.
In the code used for the Magneticum simulations the accretion rate is calculated for every black hole. Since equation (59) depends on the properties of the surrounding gas a mean value of the accretion rate has to be calculated. Therefore, one has to choose a number of neighbouring particles. With the mean values of ρ, $c_{\rm s}$ and v of these particles the accretion rate can be estimated:

$$\dot{M}_{\rm B} = \frac{4\pi\alpha G^2 M_{\rm bh}^2 \langle\rho\rangle}{(\langle c_{\rm s}\rangle^2 + \langle v\rangle^2)^{3/2}}. \tag{68}$$

Following equation (68) the mass of the black holes increases. To compensate the mass loss of the gas, neighbouring gas particles are taken out of the simulation. These particles are selected by chance. Every gas particle can be divided in four slices, which can be taken out separately.
However, the black hole accretion rate is limited by the Eddington rate. This means that matter can only be radiated if the radiation force is smaller than the gravitational force

for an electron proton pair:

$$\frac{\sigma_{\mathrm{T}} L}{4\pi r^2 c} < \frac{G M_{\mathrm{bh}}(m_{\mathrm{p}} + m_{\mathrm{e}})}{r^2}, \tag{69}$$

where m_{p} is the proton mass, m_{e} the electron mass, and σ_{T} the Thompson scattering cross section. Using the approximation $m_{\mathrm{p}} + m_{\mathrm{e}} \approx m_{\mathrm{p}}$ and solving equation (69) for L defines the Eddington luminosity:

$$L_{\mathrm{Edd}} := \frac{4\pi G c m_{\mathrm{p}} M_{\mathrm{bh}}}{\sigma_{\mathrm{T}}}. \tag{70}$$

With $L = \epsilon_{\mathrm{r}} \dot{M} c^2$, the Eddington accretion rate is given by:

$$\dot{M}_{\mathrm{Edd}} = \frac{L_{\mathrm{Edd}}}{\epsilon_{\mathrm{r}} c^2} = \frac{4\pi G M_{\mathrm{bh}} m_{\mathrm{p}}}{\epsilon_{\mathrm{r}} \sigma_{\mathrm{T}} c}, \tag{71}$$

where

$$\epsilon_{\mathrm{r}} = \frac{L}{\dot{M} c^2} \tag{72}$$

(Springel et al. 2005) is the radiative efficiency. It will be explained later in more detail. Thus in the GADGET code, the black hole accretion rate $\dot{M}$ is limited to $\dot{M}_{\mathrm{Edd}}$ like in Springel et al. (2005):

$$\dot{M} = \min(\dot{M}_{\mathrm{B}}, \dot{M}_{\mathrm{Edd}}). \tag{73}$$

3.3.3 Black Hole Mergers

In addition to gas accretion, black holes can also grow by merging with each other. In the simulations used in section 4 - 6, two criteria for black hole mergers have been used:

- The two black holes have to see each other, i.e. they have to be within the smoothing length.
- The relative velocity to each other may not exceed 50 % of the sound speed.

The resulting black hole is positioned at the center of mass of the two merging black holes. In contrast to the original code the Magneticum simulations contain a dynamical friction force as described by Hirschmann et al. (2013). This helps the black holes to stay within their host galaxy, even when they are satellites of a larger galaxy.
In the simulations used in section 7 a maximum relative distance of the black holes to each other was implemented as another criterium. This helps to keep the black holes in the center of the host galaxy during merger events.

3.3.4 AGN Feedback

Due to the gas accretion, black holes release energy to the surrounding medium, generally referred to as AGN feedback. It can be calculated by using Einstein's famous formula $E = Mc^2$. As described in section 2, the released gravitational energy is $\epsilon_\mathrm{r} M_\mathrm{bh} c^2$. This has to be multiplied by a factor ϵ_f called the feedback efficiency. As explained by Booth & Schaye (2009), it is the efficiency with which the energy radiated from the black hole is coupled to the ISM. Thus, the feedback energy per time is

$$\dot{E}_\mathrm{feed} = \epsilon_\mathrm{f} \epsilon_\mathrm{r} \dot{M} c^2 \tag{74}$$

(Springel et al. 2005). In the simulations analysed in section 4 and 5 the constant value $\epsilon_\mathrm{r} = 0.1$ was adopted from the studies by Springel et al. (2005). This is the mean value found by Shakura & Sunyaev (1973). In section 2.2 it was already shown that the radiative efficiency might not be constant due to the spin of the black hole. There is also significant observational evidence (e.g. Davis & Laor 2011, Chelouche 2013) for the dependence of ϵ_r on the mass. For that reason the influence of ϵ_r on the evolution of black holes and galaxies will be studied in section 7.
For the feedback efficiency the value $\epsilon_\mathrm{f} = 0.1$ was used. This value is slightly higher than the value $\epsilon_\mathrm{f} = 0.05$ suggested by Springel et al. (2005) to be in agreement with the observed $M_\mathrm{bh} - M_*$-relation. In the Magneticum Simulations, the black hole accretion switches from a quasar-mode to a radio-mode when $\dot{M}/\dot{M}_\mathrm{Edd} < 10^{-2}$. During the radio-mode the feedback efficiency is four times higher than it is during the quasar-mode (Hirschmann et al. 2013).
Churazov et al. (2005) indeed suggested that the value of ϵ_f might not be constant. For that reason the importance of ϵ_f will be discussed in section 7 in more detail.

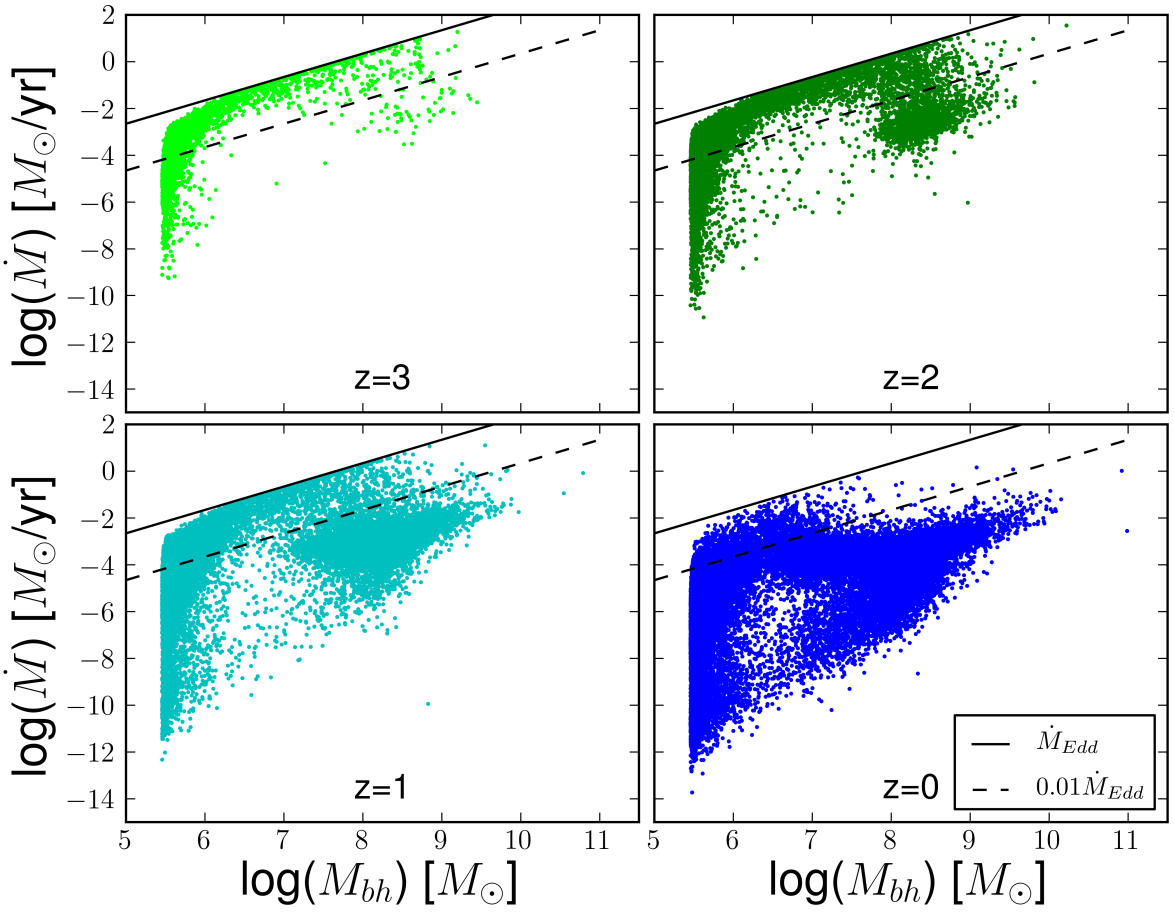

Figure 4: Masses and accretion rates of all black holes in Box3 hr of the Magneticum Simulations at different redshifts.

4 Statistical Black Hole and AGN Properties

Cosmological simulations including black hole growth have the big advantage that they facilitate a statistical analysis of black holes and AGN over cosmic time. To probe a large amount of massive black holes, the Box3 hr of the Magneticum simulations was used, providing the largest cosmological volume $(128\ \mathrm{Mpc}/h)^3$ run down to $z = 0$ used till now.

4.1 Evolution of the Accretion Rate of Black Holes

The two most important parameters to describe the growth of black holes are their mass M_{bh} and their accretion rate $\dot{M}$. Figure 4 shows the evolution of these two parameters and their relation to each other.

Once the black holes are seeded their accretion rate rises rapidly until they approach the Eddington limit. When they cross the limit $0.01\dot{M}_{\rm Edd}$ they switch from the radio-mode to the quasar-mode. This means that the feedback efficiency is four times smaller. Nevertheless, $\dot{M}$ can still grow because the Eddington accretion rate increases with the black hole mass. The black holes grow until the AGN feedback has heated the surrounding gas so much, that the accretion rate decreases rapidly. Another reason for the decrease is the gas consumption as a consequence of star formation over cosmic time. For lower redshifts a large amount of black holes is accreting at low Eddington ratios $f_{\rm Edd} = \dot{M}/\dot{M}_{\rm Edd}$. Massive black holes are not accreting close to the Eddington rate anyway. The reason is that the amount of gas is decreasing with cosmic time. The higher gas fractions in high-redshift galaxies can be seen as an explanation for the fact that most quasars are observed at high redshifts.

4.2 Evolution of the Luminosity Function

Out of the accretion rate and the radiative efficiency one can calculate the luminosity L. Due to the definition of $\epsilon_{\rm r}$ used by Hirschmann et al. (2013) the formula which was used to calculate the luminosity is

$$L = \frac{\epsilon_{\rm r}}{1-\epsilon_{\rm r}}\dot{M}c^2. \tag{75}$$

The luminosity function $\Phi(L)$ can be estimated by counting all AGN in a certain luminosity range $[L, L + {\rm d}L]$ per volume and dividing this number by dL. Figure 5 shows the Luminosity function for different redshifts in Box3 hr. Their shape can be understood by comparing it with a plot of the masses of the black holes over the luminosities shown in figure 6. The peak at $\log L_{\rm bol}[{\rm erg/s}] \approx 35$ for $z = 0.0$ is due to the artificial seeding mechanism. Then the gap in the L-M-diagram appears which leads to a minimum in the luminosity function between $\log L_{\rm bol}[{\rm erg/s}] \approx 36$ and 37. For higher luminosities the number of AGN increases. For $z = 0.0$ the gap in the L-M-diagram ends at $\log L_{\rm bol}[{\rm erg/s}] \approx 41$. This is where the luminosity function flattens. Between $\log L_{\rm bol}[{\rm erg/s}] \approx 41$ and 42 there is an increase in the black hole number until the maximum is reached at $\log L_{\rm bol}[{\rm erg/s}] \approx 42$. For larger luminosities the AGN feedback and the gas consumption due to star formation leads to a strong decrease in the number of black holes. One should remark that the behaviour below 10^{42}erg/s is limited by the resolution. A higher resolution would significantly increase the amount of faint AGN.
To test the black hole model of the Magneticum simulation the luminosity functions are compared with observations. Therefore, the observed bolometric luminosities of

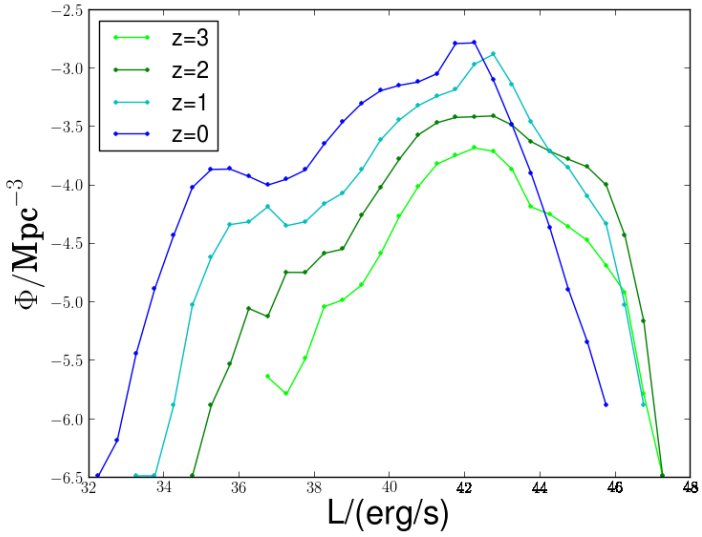

Figure 5: Bolometric luminosity functions at four redshifts (different colors) in Box3 hr.

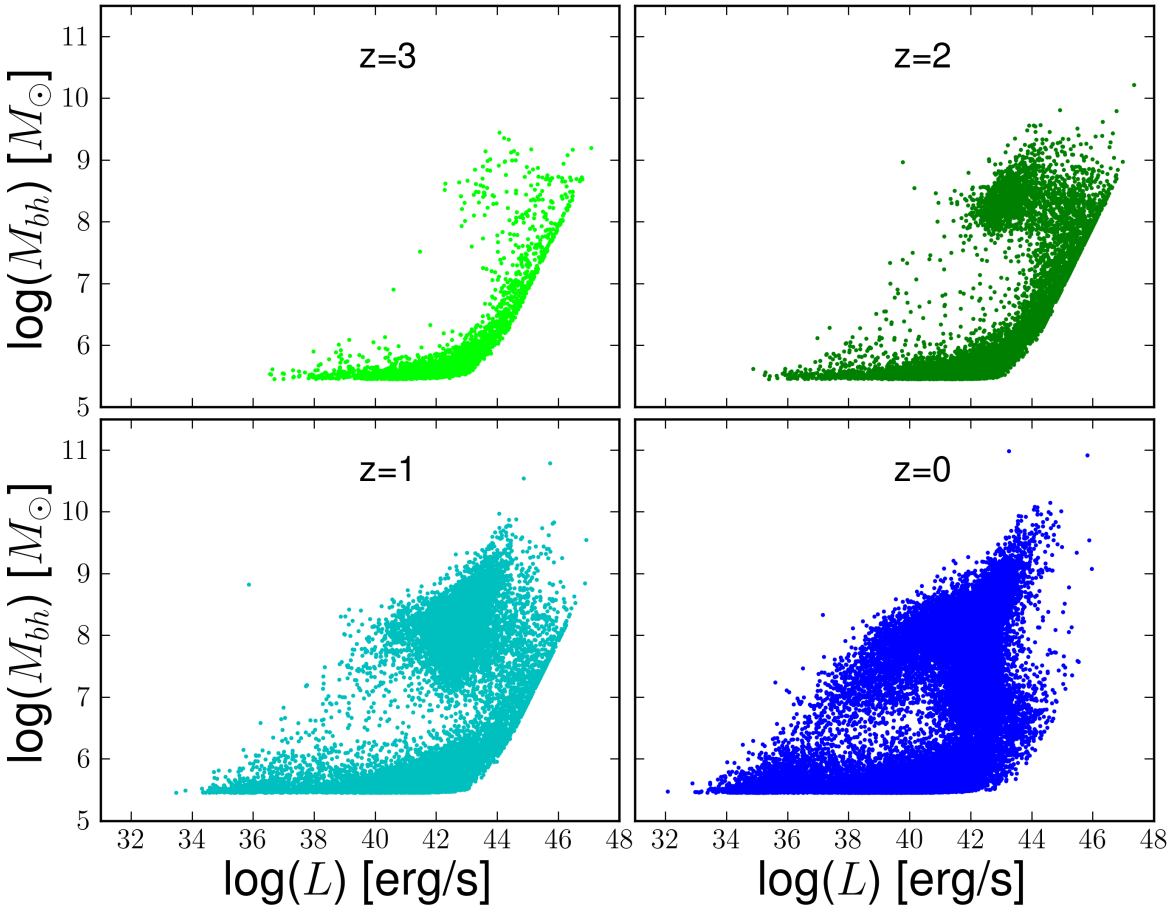

Figure 6: Black hole masses versus bolometric luminosity at four redshifts in Box3 hr.

Hopkins et al. (2007) and the soft X-ray (SXR) luminosities of Hasinger et al. (2005) are considered.
To estimate the SXR luminosities in the simulation the technique used by Hirschmann et al. (2013) is adopted. They use the approximation by Marconi et al. (2004):

$$\log(L_{\mathrm{SXR}}/L_{\mathrm{bol}}) = -1.65 - 0.22\mathcal{L} - 0.012\mathcal{L}^2 + 0.0015\mathcal{L}^3 \tag{76}$$

with $\mathcal{L} = \log(L_{\mathrm{bol}}/L_{\odot}) - 12$.
Furthermore, observations (e.g. by Hasinger 2008) indicate that a fraction of all AGN is obscured in the SXR range. It is generally accepted that this fraction depends on the luminosity, but whether it depends on the redshift is still a matter of debate (Hirschmann et al., 2013). According to Hasinger (2008), the obscuration fraction is dependent on z and is found to increase with the redshift up to $z = 2$:

$$f_{\mathrm{obsc}}(z, L_{\mathrm{SXR}}) = -0.281(\log(L_{\mathrm{SXR}}) - 43.5) + 0.279(1+z)^{\alpha} \tag{77}$$

with $\alpha = 0.62$. For $z > 2$ the obscuration fraction is approximately the same as for $z = 2$:

$$f_{\mathrm{obsc}}(z, L_{\mathrm{SXR}}) = -0.281(\log(L_{\mathrm{SXR}}) - 43.5) + 0.551. \tag{78}$$

This model was included in the calculation of the SXR luminosities.
Figure 7 shows the luminosity functions for AGN with $\log L > 42$ of the bolometric and the SXR luminosities in comparison to the observational data at different redshifts. These luminosity functions have been published by Hirschmann et al. (2013). For $z = 0.0$ and $z = 1.0$ the simulation is in excellent agreement with the observations. For $z = 2.0$ there are slightly too many AGN at $\log L_{\mathrm{bol}} \approx 45 - 46$ and $\log L_{\mathrm{SXR}} \approx 43.5 - 44.5$ in comparison to both observations. At $z = 3$, for $\log L_{\mathrm{bol}} \approx 44$ and $\log L_{\mathrm{SXR}} \approx 42$ there are too little AGN. By comparing this with figure 6 and 4 one can interpret that the rapid decrease of the accretion rate occurs a little bit too late. Thus, the overestimation might be a consequence of the fact that also low massive galaxies are over-estimated because of a too inefficient stellar feedback. The AGN feedback might also be too low.

4.3 Evolution of the AGN Number Density

The evolution of the AGN number density for different SXR luminosity bins was observed by Hasinger et al. (2005). These observations are plotted in figure 8 (stars) in comparison to Box3 hr (dots). The observations show a peak around $z \gtrsim 2$ for $\log L_{\mathrm{SXR}} > 44$.

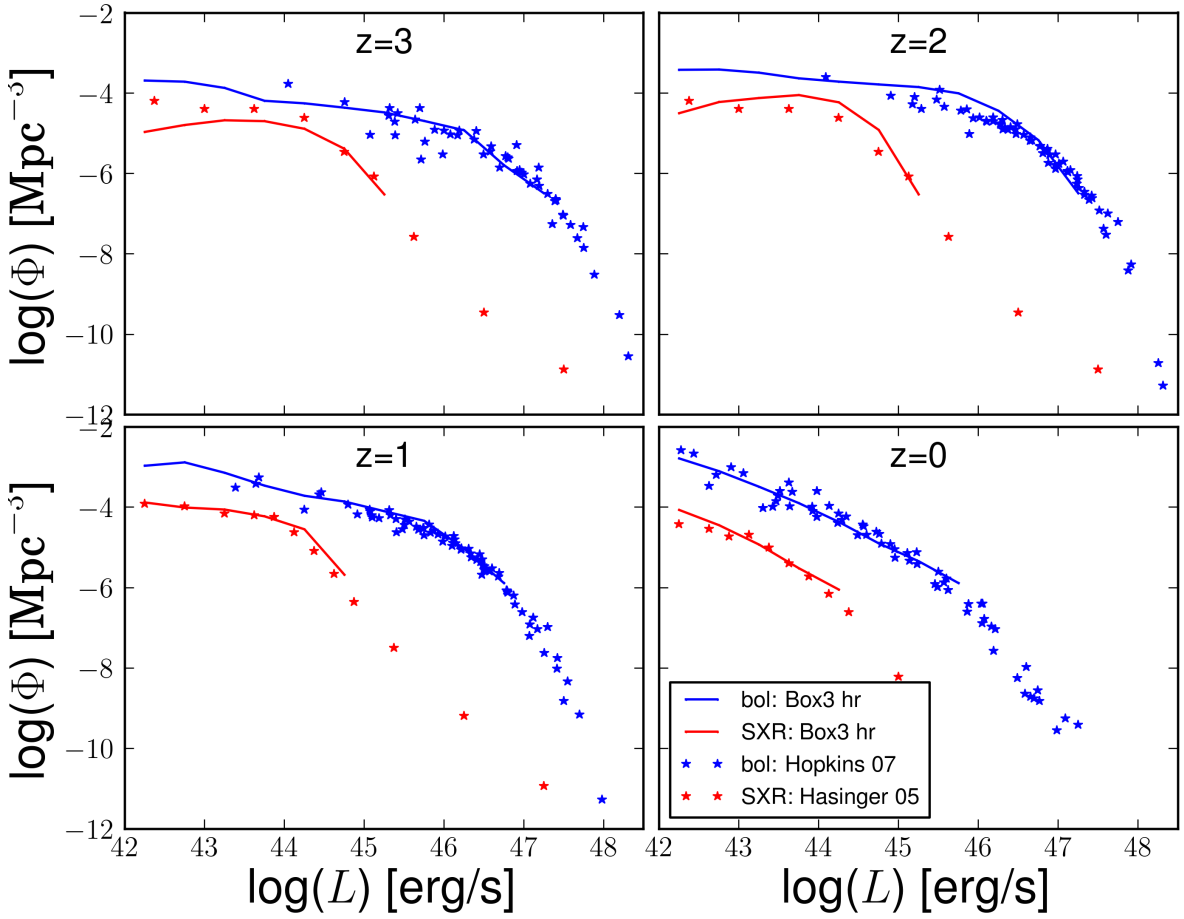

Figure 7: Bolometric and SXR luminosity functions for different redshifts in Box3 hr of the Magneticum Simulation in comparison to observations.

For smaller luminosities the maximum is shifted towards smaller redshifts. This time evolution is the typical anti-hierarchical behaviour, which was observed by several authors like Hasinger et al. (2005) and Miyaji et al. (2000).
In figure 8 the simulation is in excellent agreement with the observations at redshifts $z \lesssim 1.5$ (as in figure 7). For larger redshifts the simulation can not reproduce the observations due to the black hole seeding.
Besides the luminosity, the black hole mass is another parameter which is very useful to study the evolution of black holes. Figure 9 shows the co-moving number density evolution of the black holes in Box3 hr for different mass ranges. For $z \gtrsim 5$ there are no black holes with masses larger than $10^{10} M_{\odot}$. This is the moment when the black holes are seeded. Then the black holes grow while further new black holes are seeded. Thus, there is an increase of the number density of black holes for all mass ranges. Up to $z \approx 2.5$ the smaller the mass, the larger the number density of black holes. This behaviour changes at redshift $z \approx 2.5$. Here lines start to intersect with each other because the mass evolution of the black holes is not monotonic anymore (in contrast to the luminosity evolution). First the blue and the green curves cross, followed by the blue and the red graph lines. Finally, at redshift $z \approx 1.5$ the green and the red curve intersect. At $z \approx 0.8$ an opposing development begins and the blue and the green graph lines cross again. One might guess that the other lines might also intersect in the future. The redshift range at which there are more black holes with masses between 10^8 and $10^9 M_{\odot}$ than in the two mass ranges below are the times when most AGN exist due to figure 8. This is consistent with the relation between black hole masses and their luminosities as shown in figure 6.
But there is a significant difference between figure 8 and 9: Binned by the luminosity the number density has a maximum, whereas binned by the mass the number density increases up to $z = 0$. The reason is that in figure 9 all black holes are included whereas in figure 8 only the most luminous ones are included. This means that for redshifts $z \lesssim 1.0$ SMBHs still exist. But they are less active.

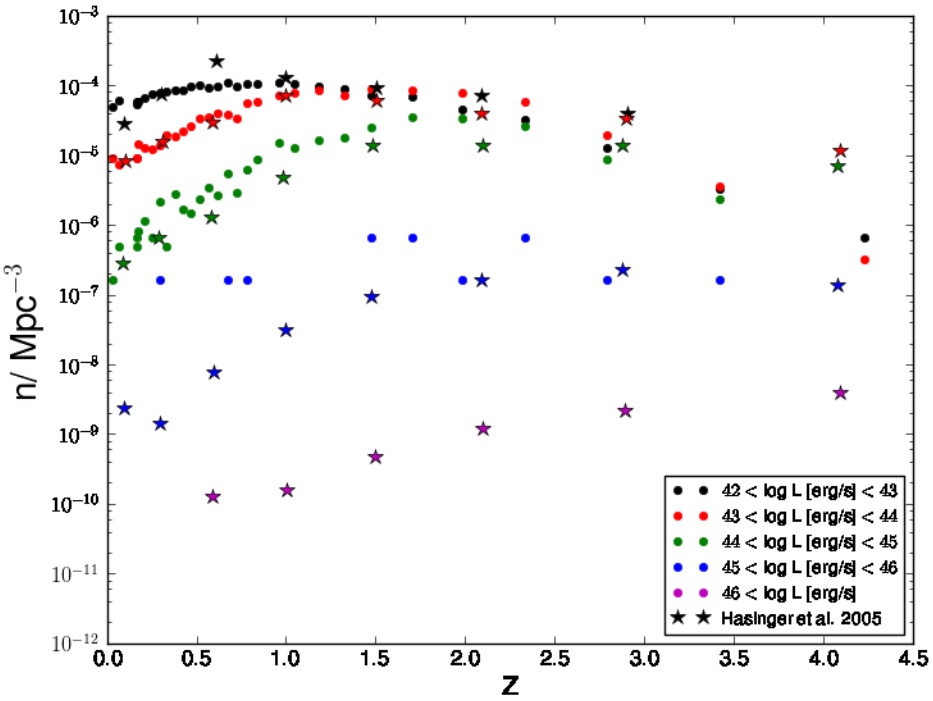

Figure 8: Co-moving number density evolution in different luminosity bins of Box3 hr (dots) in comparison to observations (stars).

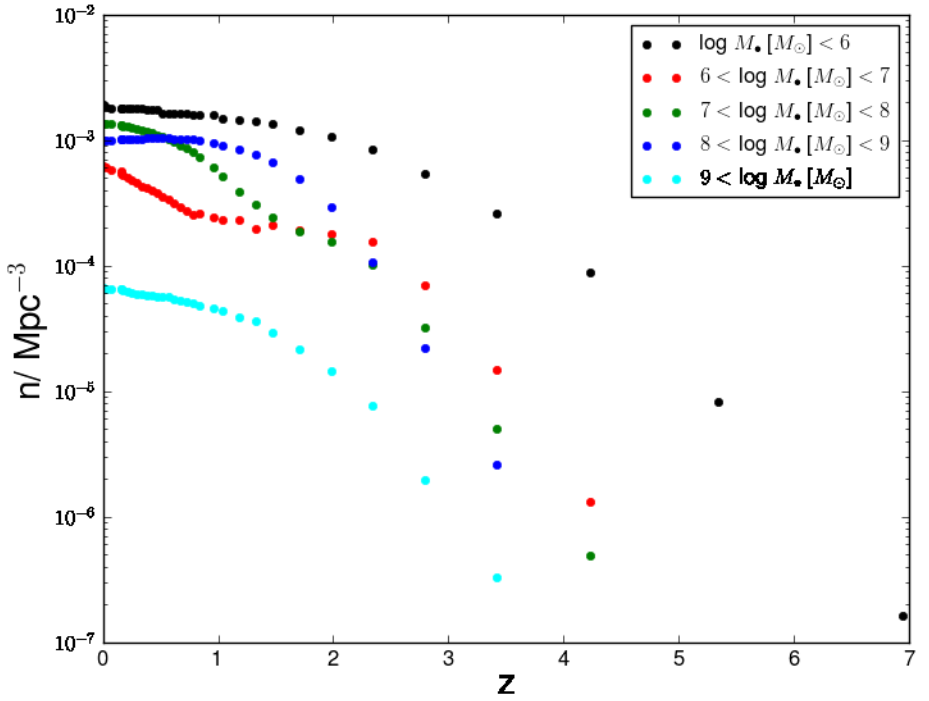

Figure 9: Co-moving number density evolution in different mass bins for Box3 hr.

5 Structure and Morphology of Galaxies

Since AGN have a significant impact on their host galaxies, the morphology and dynamics of galaxies are studied in this section. In Box4 uhr of the Magneticum simulations the resolution is high enough to study the structure of galaxies and to classify them morphologically. A first version of this box ran up to $z \approx 0.6$. At $z = 0.6$ the box contains 675 halos with total masses larger than $5 \cdot 10^{11} M_{\odot}/h$. In this thesis the expressions MS0 - MS675 will be used as names for the galaxies, where 'MS' means Magneticum simulations and the number decreases with the total mass of the halo.
The resolution of the Box4 uhr allows a qualitative analysis of the structure and dynamics of galaxies. This will help to study the connections between the properties of black holes and their host galaxy. The classification of galaxies is automated, which is described in the next sections. Thus, a quantitative description is possible.

5.1 The Face-on and Edge-on-Perspective

To get an idea of the shape of a galaxy two different viewing angles are generally used: the edge-on and the face-on perspective. If you look on a galaxy edge-on, it is easy to identify a disk if present. The face-on perspective shows potential spiral arms or a ring. To get these views it is necessary to rotate the halo such that the x- and y-axis lie in the galactic plane in the case of a disk. Therefore, the halo is rotated such that the total angular momentum of the gas, which lies inside 10 % of the virial radius, shows in z-direction. Furthermore, the coordinates are centered on the center of the galaxy.
Figure 10 shows two galaxies at $z = 1$ after the rotation. The stars are white, the cold gas is blue and hot gas is red. The upper pictures show the elliptical galaxy MS85, which has a stellar mass of $M_* = 2.5 \cdot 10^{11} M_{\odot}$ and a total halo mass of $M_{halo} = 4.7 \cdot 10^{12} M_{\odot}$. Here the stars and the gas look elliptical in the x-y-plane as well as in the x-z-plane, even though the major axis of the stars is not aligned with the major axis of the angular momentum of the gas. There is a black hole of around $10^8 M_{\odot}$ near the center of the galaxy which heats the gas.
The lower panels show the spiral galaxy MS22. Its stellar mass is $M_* = 5.1 \cdot 10^{11} M_{\odot}$ and the total halo mass is $M_{halo} = 1.1 \cdot 10^{13} M_{\odot}$. Like in in MS85 a black hole is located near the center and heats the gas. Its mass is around $2 \cdot 10^8 M_{\odot}$. The face-on perspective of MS22 shows spiral arms and the edge-on perspective shows a warped disk. Warped galaxies are very common in the real universe. This was described e.g. by Binney & Tremaine (2008). For example the Milky Way, M31 and M33 are warped, which are all

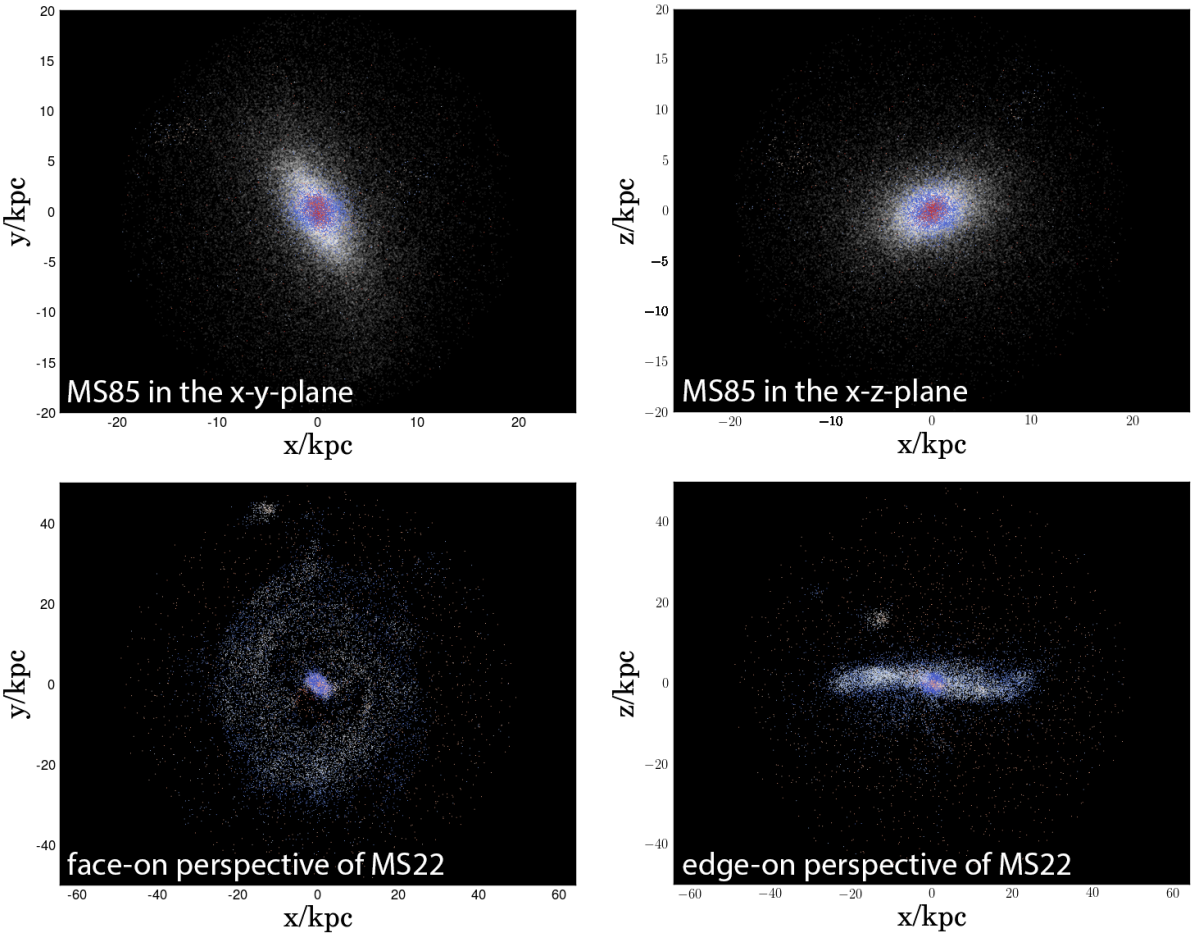

Figure 10: Stars (white), hot (red) and cold (blue) gas of the elliptical galaxy MS85 and the spiral galaxy MS22 in Box4 uhr at $z = 1$ after the rotation.

spiral galaxies in the Local Group. This already indicates that with a sufficient resolution the code is able to produce realistic disks.

5.2 Galaxy Classification

To examine the difference of black holes in different galaxy types it is necessary to classify the galaxies morphologically. There were two different classification methods used in this thesis: The first one is to calculate the surface density, which is shown in section 5.2.2. For disks it should follow an exponential law, whereas in ellipticals as well as in the bulges of disks the surface density can be described by a (single) power law. The other method is to test whether the particles move on a circle in the x-y-plane. In that case they are significantly rotation supported and thus form a disk. This can be tested

by calculating the circularity, which is described in section 5.2.3.
For both methods it is important to exclude substructures around the central galaxy as it is described in section 5.2.1, because they appear as stray peaks in the overall surface brightness and also cause additional, but offset peaks in the circularities. A subhalo grid helps to speed the calculations of the surface density and the circularities up because the data of the subhalos have to be read only once.

5.2.1 Subhalo Mask

An easy solution to exclude subhalos is to define a mask in form of a grid. This was done inside one half-mass radius of the central galaxy. The grid was only calculated for the face-on perspective, because it will be used for the galaxy classification. In contrast to observations it does not matter which viewing angle is used, because simulations contain the three dimensional velocity data. Therefore, one is not limited to the line-of-sight velocity. The size of one grid cell is chosen to be 1 kpc^2. The coordinates of the center of every subhalo are known from the standard post-processing files. To estimate the radius of the subhalos, two times the half-mass radius of the substructure was used. This value is an acceptable compromise between cutting out as much as possible and not loosing too much information about the central galaxy. For every subhalo the corresponding places in the grid are marked with the number 1 such that every grid point contains the information if there is a substructure or not. The coordinates of all grid points containing a substructure are saved in a file sorted by the radius. For the calculations of the surface density and the circularity this file was used to exclude the subhalos. Using a grid size of 1 kpc^2 allows to investigate whether the integers of the coordinates of the particles can be found in the file.
Figure 11 shows MS1 and its subhalo mask. This galaxy is the second largest halo in Box4 and hence having a variety of substructures. There are many small gas clouds around the central galaxy which contain only gas and are not identified as subhalos. Therefore, one should concentrate on the stars (white) for the comparison with the subhalo mask. Most of the located subhalos are visible. Nevertheless, there are a few subhalos which are not visible, because they consist mainly of dark matter. The amount of particles inside these subhalos is very small. That is why it should not affect the calculation of the surface density and the circularity.

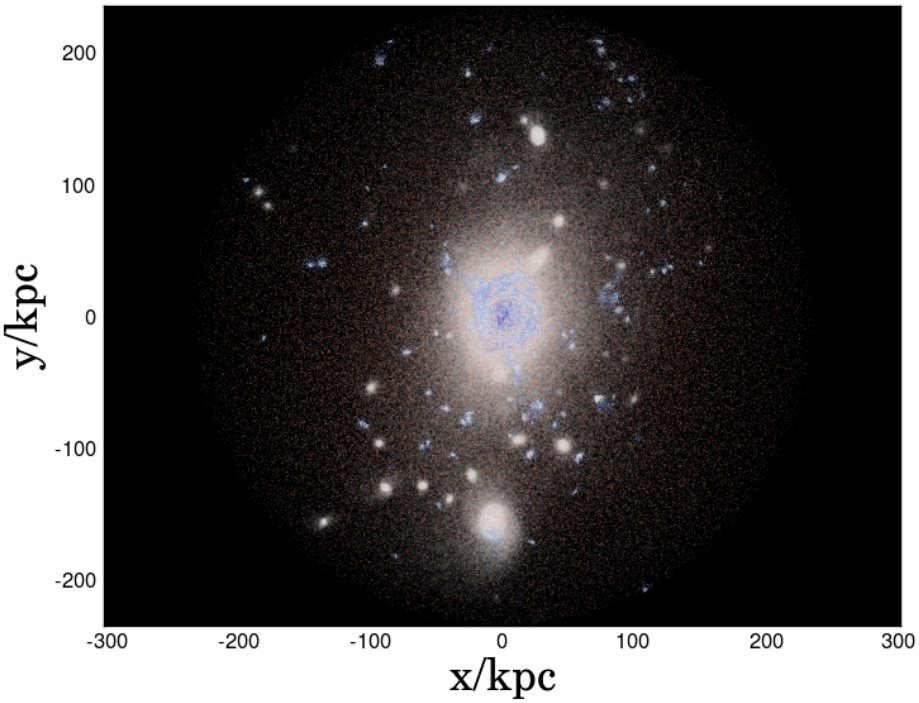

(a) cold gas (blue), hot gas (red) and stars (white)

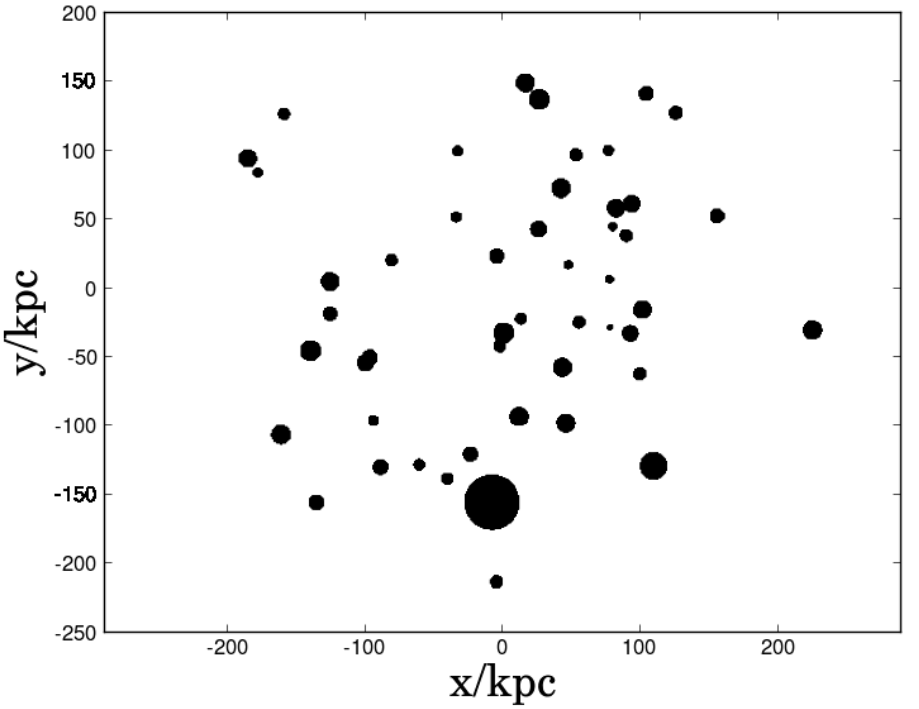

(b) subhalo grid

Figure 11: MS1 inside one half-mass radius of the main galaxy and the corresponding subhalo grid.

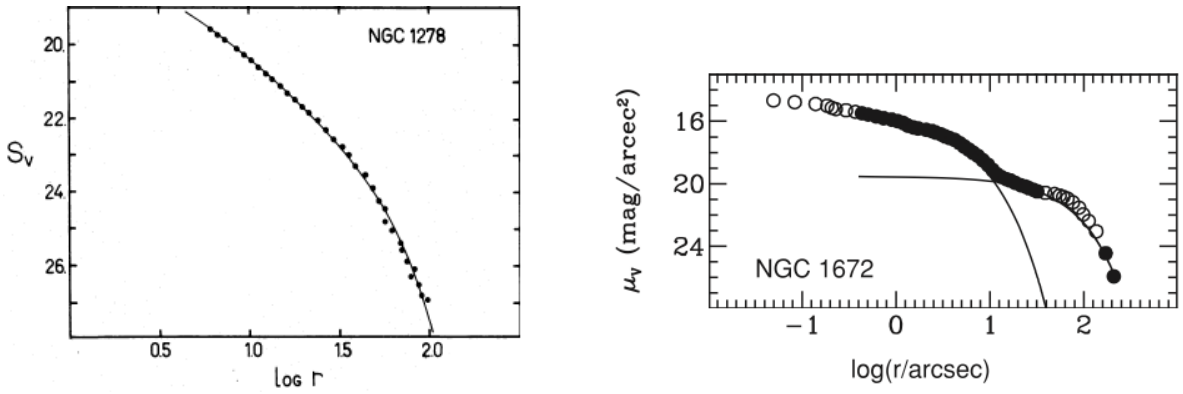

(a) elliptical galaxy

(b) spiral galaxy

Figure 12: Surface brightness profile of the elliptical galaxy NGC 1278 (copy from Oemler, 1976) and the spiral galaxy NGC 1672 (copy from Fisher et al., 2009). For both graphs the radius r is given in arcsec. S_V and μ_V are both expressions for the surface brightness in mag/acrsec^2.

5.2.2 Surface Density

A standard method which observers use to analyse the structure of galaxies, is to plot their surface brightness profiles. For elliptical galaxies it follows an exponential law. This was already observed by Oemler (1976). One of his results is shown in figure 12 (a), where the dots represent his data, whereas the graph line represents the fit of an exponential law. For disk galaxies it is more complicated, because they generally consist of two components: the bulge and the disk. The surface brightness of the bulge follows an exponential law like elliptical galaxies, whereas the disk can be fitted with a power law. This was observed amongst others by Fisher et al. (2009). Figure 12 (b) shows their results for the spiral galaxy NGC 1672, where the dots represent their observations and the two lines represent the fit of an exponential law in the inner part and a power law in the outer part.

After all, the galaxies in Box4 uhr of the Magneticum simulations can be classified morphologically by plotting their surface density profile and fitting it with a combination of an exponential law and a power law. This was done in figure 13 separately for the cold gas and the stars of MS85 and MS22. The surface density profiles were fitted with the sum of an exponential law and a power law. The exponential law should represent a disk component and the power law an elliptical component.

The stars can be fitted very well with a power law and an additional small exponential component. This means that both galaxies have an elliptical stellar distribution.

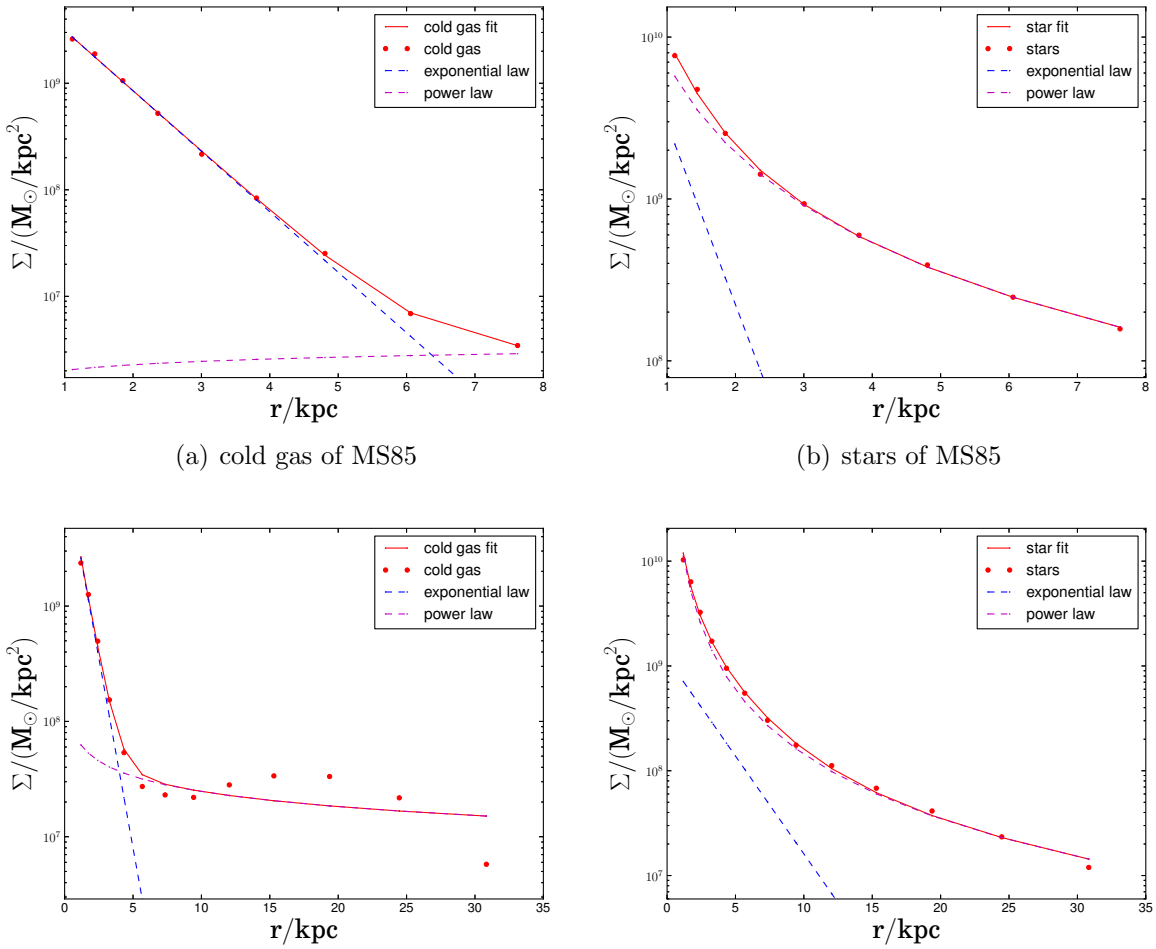

(a) cold gas of MS85

(b) stars of MS85

(c) cold gas of MS22

(d) stars of MS22

Figure 13: Surface densities of the cold gas and the stars of MS85 and MS22 at $z = 1$.

The cold gas is much more difficult to fit. The fit in figure 13 (a) is unphysical because of a rising power law component. Due to figure 10 the cold gas should be elliptical. The reason for that fitting mistake might be that the density profile flattens for very small radii due to the limited resolution. Figure 13 (c) shows another problem which can appear when studying disks. Obviously, the surface density does not decrease exponentially. Instead, there is a gap between the bulge and the disk in the cold gas component. At around 15 to 20 kpc there is a maximum in the density profile. This can also be seen in figure 10. Such a ring structure can not be fitted.

For these reasons, fitting the surface density is not sufficient enough for classifying all 675 galaxies. Nevertheless, surface density profiles are useful to describe the structure of galaxies in detail.

5.2.3 Circularity

The circularity ϵ is the angular momentum of a specific SPH particle in z-direction divided by the angular momentum it would have if it moved exactly on an orbit in the x-y-plane. Its definition was extrapolated from Scannapieco et al. (2009):

$$\epsilon = \frac{j_z}{j_c} \quad , \tag{79}$$

where j_c is given by

$$j_c(r) = r \cdot v_c(r) = r \cdot \sqrt{\frac{GM(<r)}{r}} \quad . \tag{80}$$

The circularities have been calculated for all particles inside three times the half-mass radius of the central galaxy. $f(\epsilon)$ is the fraction of the particles with ϵ in a range $\Delta\epsilon = 0.1$. A peak around $\epsilon = 0$ means that the particles do not prefer moving in the x-y-plane. Due to Scannapieco et al. (2009), this would mean that the galaxy is an elliptical galaxy. A smaller peak at $\epsilon \approx 0$ can also represent a bulge. If this peak is shifted towards $\epsilon = 1$, the bulge rotates. This might also be a hint for a bar.
If the galaxy is a disk, $|j_z|$ and $|j_c|$ should be equal, which means that there is a peak at ± 1. Since the galaxies were rotated such that the maximum angular momentum goes in z-direction, the peak is always at 1. To be able to distinguish between different components the plots of the circularities were fitted with one, two or three Gaussians. In the end the possibility with the smallest χ^2-value was chosen.
Because of the many degrees of freedom for two or three Gaussian it was not possible to fit the data at once. Therefore, at first only one part of the data was fitted by one Gaussian. To select the data corresponding to that Gaussian the data was selected in four ways:

- using all data,
- using only the maximum and the values $< f_{max}/3$ (to get rid of a second maximum near the global maximum),
- using only the right side of the peak (this side was mirrored to the left),
- using only the left side of the peak (this side was mirrored to the right).

The version with the smallest χ^2-value was used to fit the remaining data with another Gaussian.
In the next step, two Gaussians were fitted. The results of the first two fits were used as

initial parameters. The same procedure was used for a third Gaussian.
Figure 14 shows the results for the cold gas and the stars of MS85 and MS22. The Gaussian fits work very well and the plots are in agreement with the expectations, that

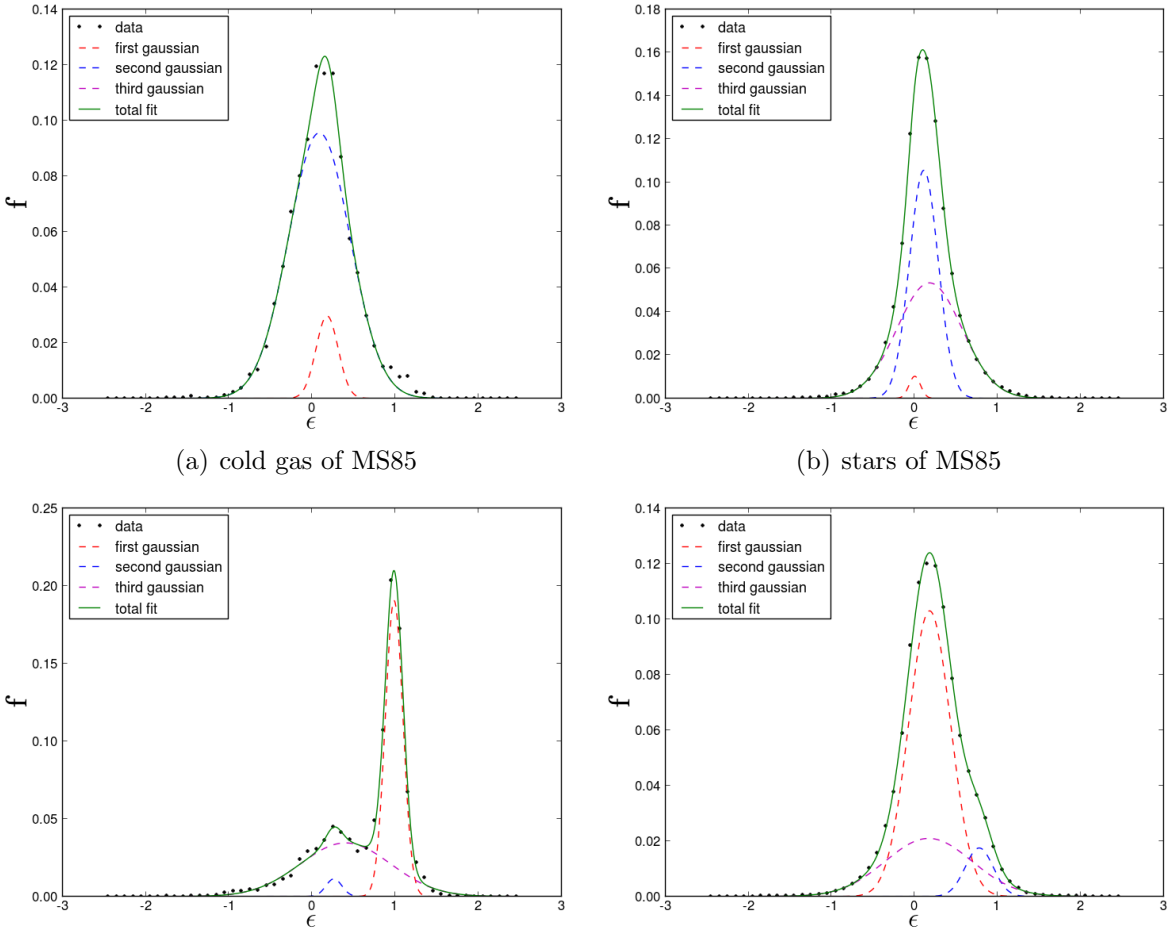

(a) cold gas of MS85

(b) stars of MS85

(c) cold gas of MS22

(d) stars of MS22

Figure 14: Circularities of the cold gas and the stars of of MS85 and MS22 at $z = 1$. $f(\epsilon)$ is the fraction of the particles with ϵ in a range $\Delta\epsilon = 0.1$.

there is a peak at $\epsilon \approx 0$ for MS85. This confirms that it is an elliptical galaxy. For both cold gas and stars there are two major elliptical components. The reason for these two kinematic components is unclear, but it might refer to a merger, which could have occurred in earlier times. The small red Gaussian in figure 14 (b) might be a part of a substructure which was not cut out completely.
The stars of MS22 (figure 14 d) also have a peak around $\epsilon = 0$, whereas a small fraction of the stars move into the disk (blue curve). The cold gas of MS22 (figure 14 c) forms a disk. So there is a peak at $\epsilon \approx 1$. MS22 also has a bulge which is represented by the

purple curve in figure 14 (c). It has a peak between $\epsilon = 0$ and $\epsilon = 1$. This means that the bulge rotates slightly. MS22 is a representative example for a gas disk with elliptic stellar dynamics. This is very common in the Magneticum simulations. Interestingly figure 10 shows that the stars of MS22 nonetheless lie in the plane of the cold gas disk. This means that the cold gas is the most important component for the classification of galaxies, assuming M_*/M_{gas} is small enough.
The Gaussian fits were made for all 675 galaxies at $z = 0.6$. To classify them the different Gaussians were related to three different ranges:

- The mean value $\bar{\epsilon}$ is smaller than 0.3: The Gaussian represents an elliptical component.
- The mean value $\bar{\epsilon}$ is larger than 0.7: The Gaussian represents a disk component.
- The mean value $\bar{\epsilon}$ lies between 0.3 and 0.7: This region was set to make the attribution to the other two regions more accurate. Nevertheless, it might represent an own class of galaxies, which is described later.

The result of this classification is shown in figure 15. It shows the number of galaxies which have the fraction M/M_{tot} of the total mass in bins of 0.1 in the three different ranges. It was distinguished between stellar masses M_* of the central galaxy being smaller or larger than $2 \cdot 10^{11} M_\odot$. This is the threshold above which Cappellari et al. (2013) found only ellipticals. Obviously, this is not the case in the Magneticum simulation. Perhaps this is due to the estimation of the stellar mass. For the Magneticum simulation the stellar mass inside one half-mass radius of the stars was used. Cappellari et al. (2013) measured the stellar mass inside the observed effective radius. Figure 15 can be interpreted as follows:

- $\bar{\epsilon} < 0.3$:
  There are many galaxies which have no component with a peak around $\epsilon = 0$. All in all there are around 70 galaxies which are elliptical and have no rotating component. As expected for $M_* > 2 \cdot 10^{11} M_\odot$ it is more likely to find such a galaxy than for lower masses. There are also a significant amount of galaxies with 70-80% of their mass being non-rotating. Since such huge bulges are not expected, it might be that there are in-falls of substructures which produce a peak at $\epsilon = 1$. Only a few galaxies have a non-rotating bulge, especially for small stellar masses. Very small bulges with less than 30% of the total mass are also common.

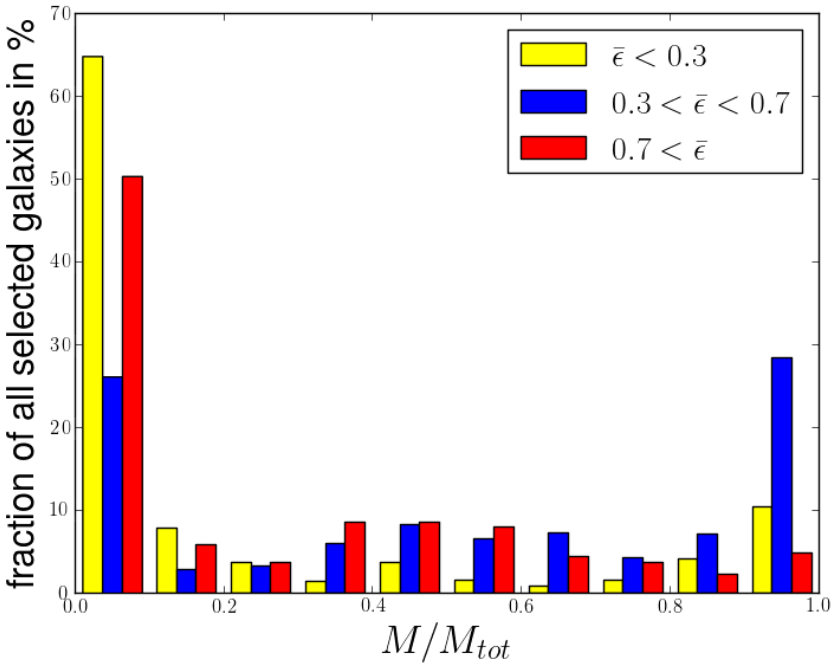

(a) Halos with stellar masses $M_* < 2 \cdot 10^{11} M_\odot$

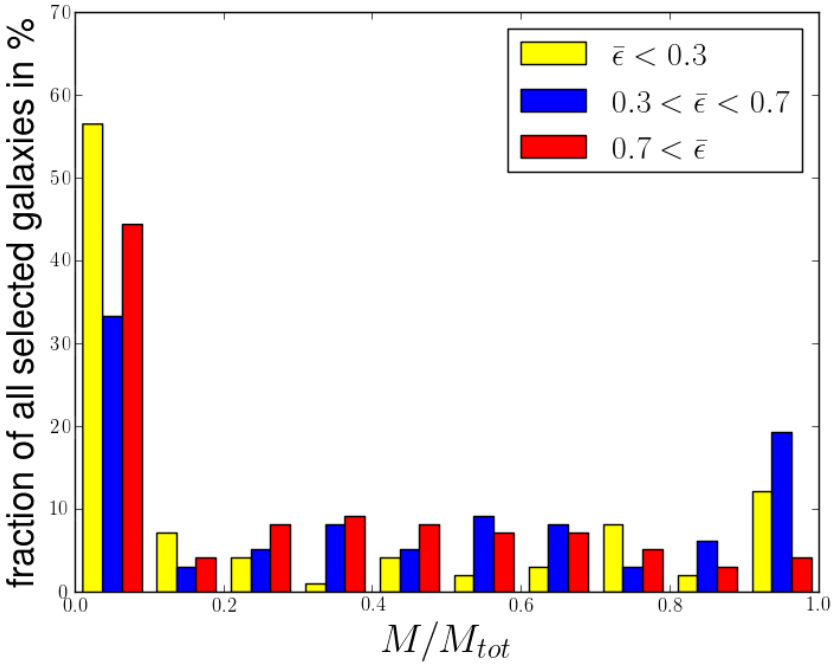

(b) Halos with stellar masses $M_* > 2 \cdot 10^{11} M_\odot$

Figure 15: Components of the cold gas which belong to Gaussian with the mean value $\bar{\epsilon} < 0.3$ (elliptical), $\bar{\epsilon} > 0.7$ (disk) or between at $z = 0.6$.

- $\bar{\epsilon} > 0.7$:
  Against the expectations due to the observations by Cappellari et al. (2013) disks can be found in both mass ranges. Typically only a fraction of the cold gas is in the disk. This fraction can be very different. Mostly it lies between 30% and 70%. This was expected, because the other part should form a bulge. There are few small disk components with 20-30%. They could be the counterpart of the elliptical components of 70-80%

- $0.3 < \bar{\epsilon} < 0.7$:
  Interestingly, by far the most galaxies have one component in the circularity distribution with a peak between 0.3 and 0.7. This means that the particles clearly have a preferred direction of rotation. Nevertheless, these galaxies also have elliptical properties. Actually there is a galaxy type with these properties, namely lenticular (S0) galaxies. There are more S0 galaxies than ellipticals, which was constrained by the Cappellari et al. (2011) for the ATLAS^{3D} sample. The Magneticum Simulation confirms these observational results.
  It is also very common that only one part of the cold gas forms a component with $0.3 < \bar{\epsilon} < 0.7$. These components could be rotating bulges or even bars. This is for example the case for the galaxy which will be analysed in section 5.3.

Overall, most galaxies have different components like a disk component and a bulge, but it might still be that substructures distort the results of figure 15, because only two times the half-mass radius of the substructures has been cut out. There are many S0 galaxies, but also ellipticals. These results are in agreement with the results of Cappellari et al. (2011), who observed a large sample of galaxies (the ATLAS^{3D} sample) and classified them. 70% of their sample are spiral galaxies, 22% are lenticular galaxies and 8% ellipticals. To compare this with the Magneticum simulation one can make the following assumptions:

- All galaxies with an elliptical component ($\bar{\epsilon} < 0.3$) of 100% are elliptical galaxies.

- All galaxies with a lenticular component ($0.3 < \bar{\epsilon} < 0.7$) of 100% are lenticular galaxies.

- The other galaxies are spiral galaxies.

Then the sample of galaxies in the Magneticum Simulation consists of ∼10% ellipticals, ∼25% lenticular galaxies and ∼65% spirals. Of course there are discrepancies because

the redshift of the simulation is $z = 0.6$, which can not be compared with observations of the local universe. Nevertheless, these results are very similar, which is an evidence for the success of the Magneticum simulations in reproducing the real universe.
Having classified the galaxy types, it is interesting to explore how black hole growth is correlated with the different galaxy types. Therefore, in figure 16 the accretion rate was plotted versus the black hole mass. Furthermore, the fraction of mass inside a disk component is represented by a color bar. To exclude unphysical cases, only black holes which are less than 5 kpc away from the center were included. Figure 16 shows that very large disk components are more common for larger black holes. The black holes in disks as well as their accretion rates are larger at $z = 0.6$ than at $z = 1$. This indicates that the black holes in disks grow more than in elliptical galaxies, which might be due to the fact that spiral galaxies generally have a higher gas fraction than elliptical galaxies. For these two galaxy types the accretion rate seems to decrease over time.
In figure 16 there are more black holes for $z = 1$ than for $z = 0.6$. This is due to the fact that for smaller redshifts more black holes are far away from the center of the galaxy. This is true especially for spiral galaxies, because around 65% of all galaxies should contain a disk component. The reason might be that black holes do not behave correctly during merger events, especially during early mergers, which form a disk. Thus, it might be, that too small substructures already contain black holes. Another problem might be that after a black hole merger the 'new' black hole is not positioned correctly. In fact, in later test runs of the Magneticum Simulation the merging of black holes could be improved such that most of the black holes now stay in the center of galaxies. But this works only when they are not seeded too early. In that case the black holes can be seeded in too small substructures and thus could be dislocated during the whole run.

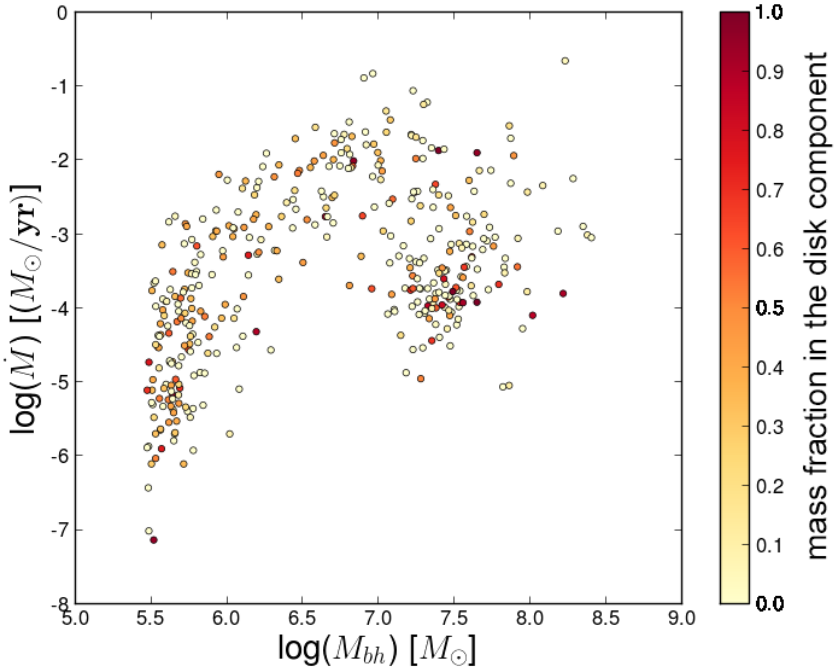

(a) $z = 1$

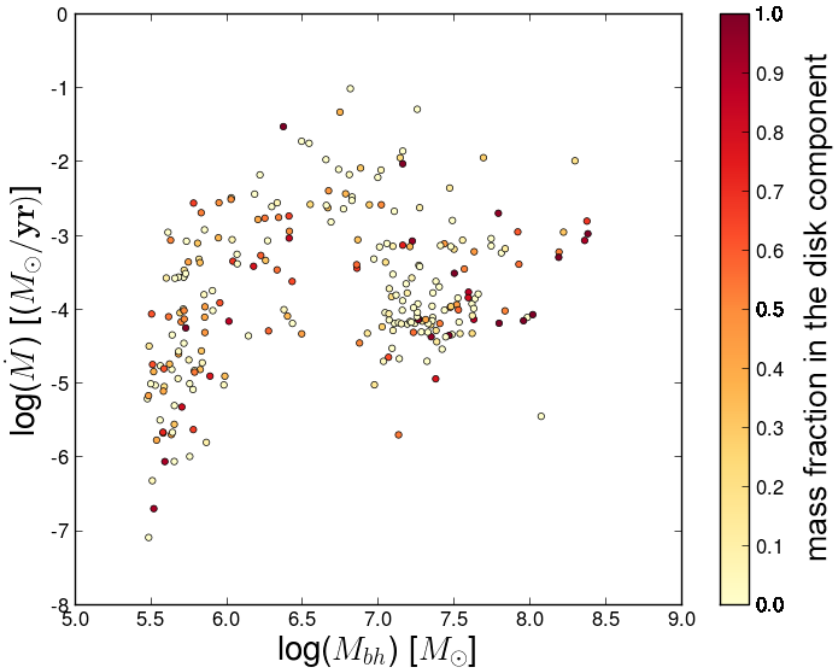

(b) $z = 0.6$

Figure 16: Accretion rate over black hole mass for Box4 uhr_bao for two different redshifts. The color bar represents the fraction of mass in the disk component. Only black holes which are less than 5 kpc away from the center were included.

5.3 The 'Ring Galaxy'

In this section one specific interesting galaxy will be studied in detail. It has a ring structure in the gas component. Therefore, we call it the 'ring galaxy'. In this chapter, the formation of the ring and the dynamics of the ring galaxy will be examined.

5.3.1 Structure and Evolution

Figure 17 and 18 show the cosmic evolution of the ring galaxy in the face-on view. In figure 17, one can see that the galaxy was a small elliptical before $z = 2$. At $z = 2.8$ many cold gas clumps are visible. Only a few of them already have formed stars. Two of them have a black hole in their center. The substructures fall into the galaxy, but they do not disturb the elliptical structure.
At $z = 2$ a major merger occurs. This merger forms the disk. At $z = 1.7$ the disk structure is visible. The galaxy has a cold gas bulge. There are two black holes which have not yet merged with each other and are dislocated form the center. This is an evidence that black holes are kicked away from the center during mergers. So the merging of black holes in this run of the Magneticum Simulations does not yet describe reality correctly. Since the black holes move around the bulge, it might be that they have created the density gap between the bulge and the ring in the gas component due to gas accretion and AGN feedback. Thus, the ring might be an artefact, which was only formed because of the dislocated black holes.
Later on, the bulge develops to a bar. The ring structure is stable during the whole simulation. One can also see that the amount of stars is getting larger with time. At $z = 0.6$ there are still substructures falling into the galaxy, but their number is decreasing with time.
Figure 19 shows the edge-on view of the ring galaxy for $z \leq 1.2$ inside 30 kpc. It clearly shows the gas disk, whereas the stars are shaped elliptically. As in figure 18 one can see that there is fewer gas at smaller redshifts. The central black hole is mostly not located in the disk plane. Thus, it is unclear, if it really could have formed the ring. The second black hole is mostly far away from the center and thus should not affect the structure of the galaxy. At $z = 0.6$ the bulge has two components and is even box-shaped. In the next section we will see that this is due to dynamics.

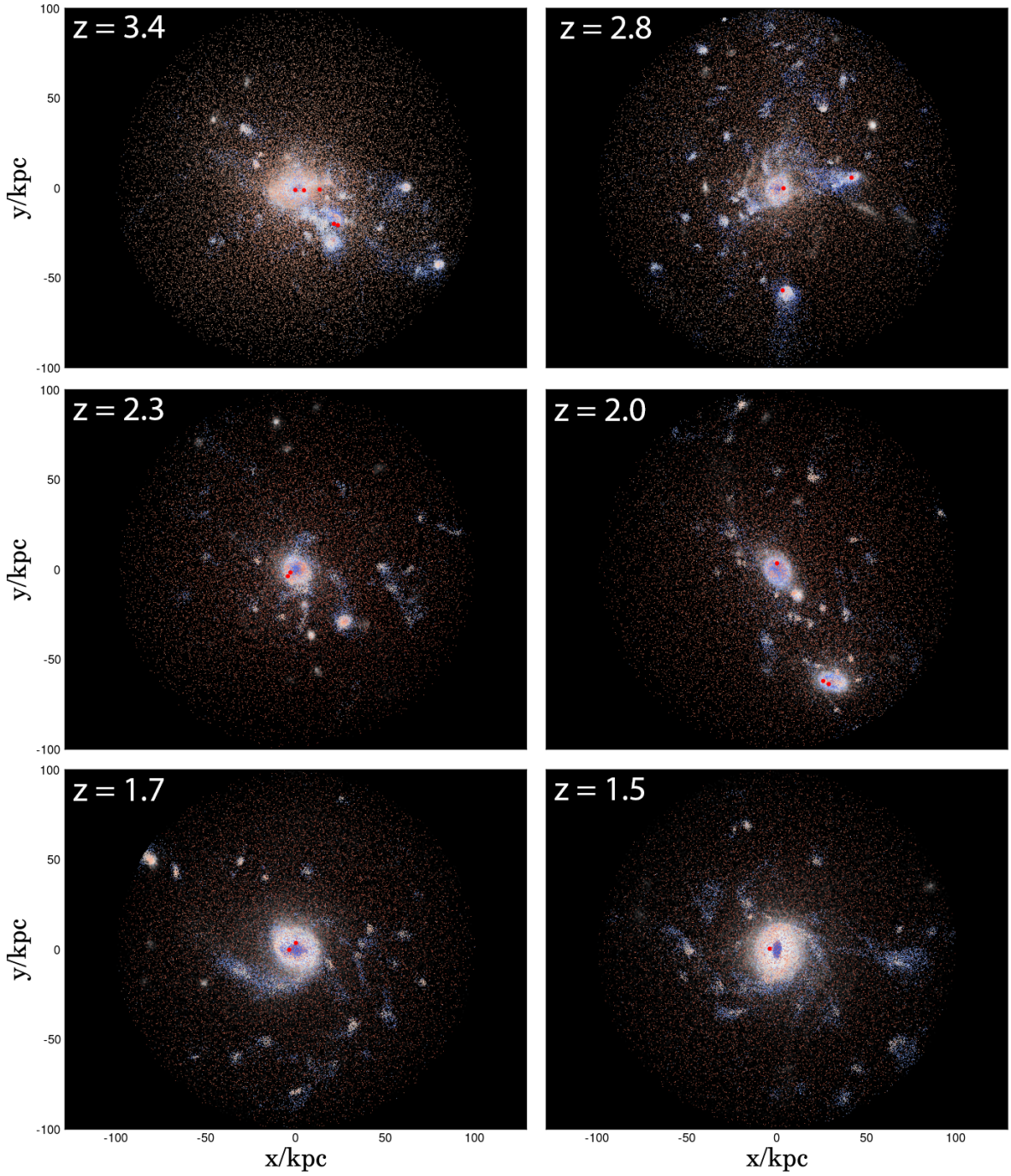

Figure 17: Evolution of the ring galaxy for $z \geq 1.5$ in the face-on perspective. Stars are white, cold gas is blue and hot gas is red. The large red dots mark the positions of the black holes.

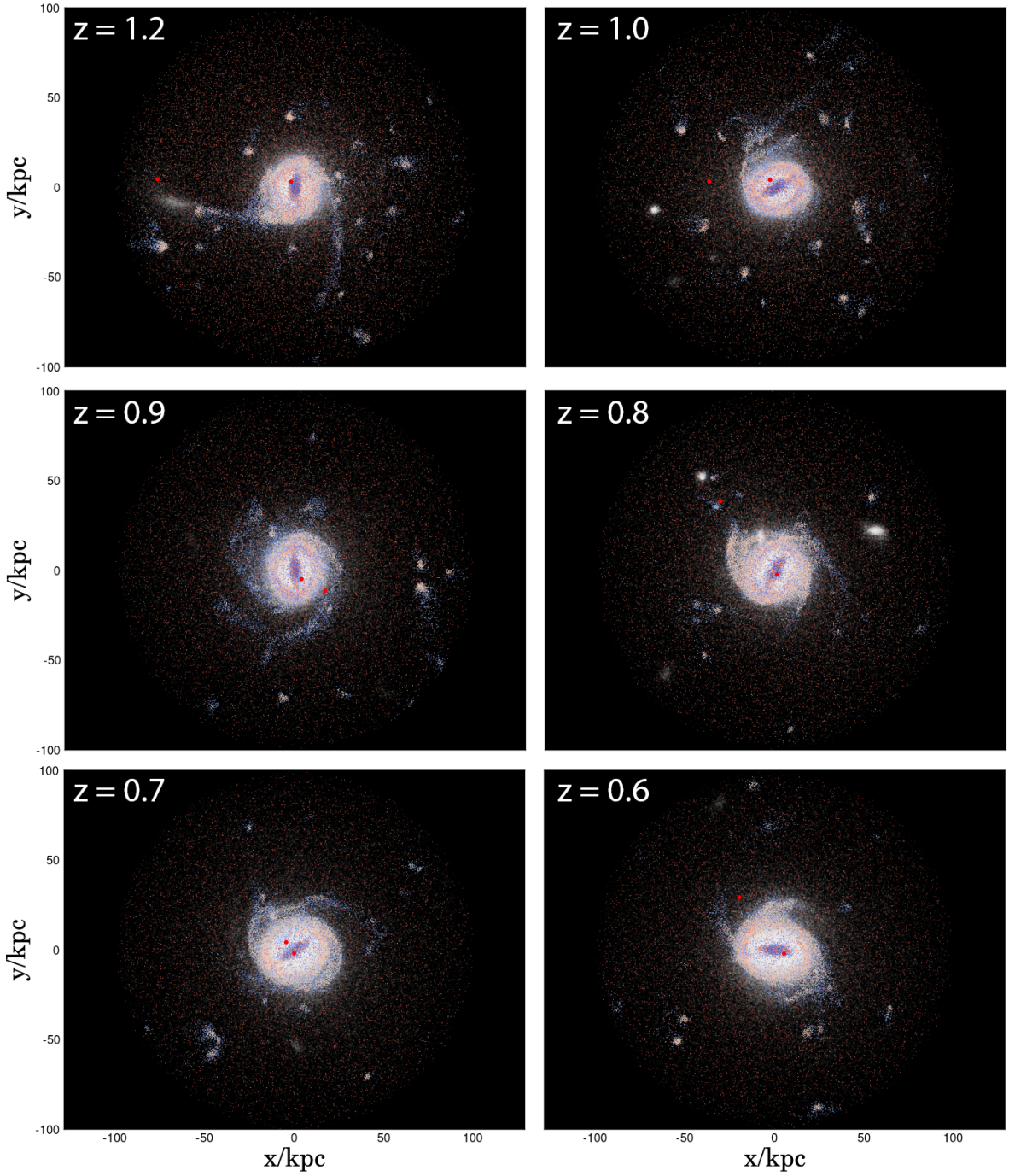

Figure 18: Evolution of the ring galaxy for $z \leq 1.2$ in the face-on perspective. Stars are white, cold gas is blue and hot gas is red. The large red dots mark the positions of the black holes.

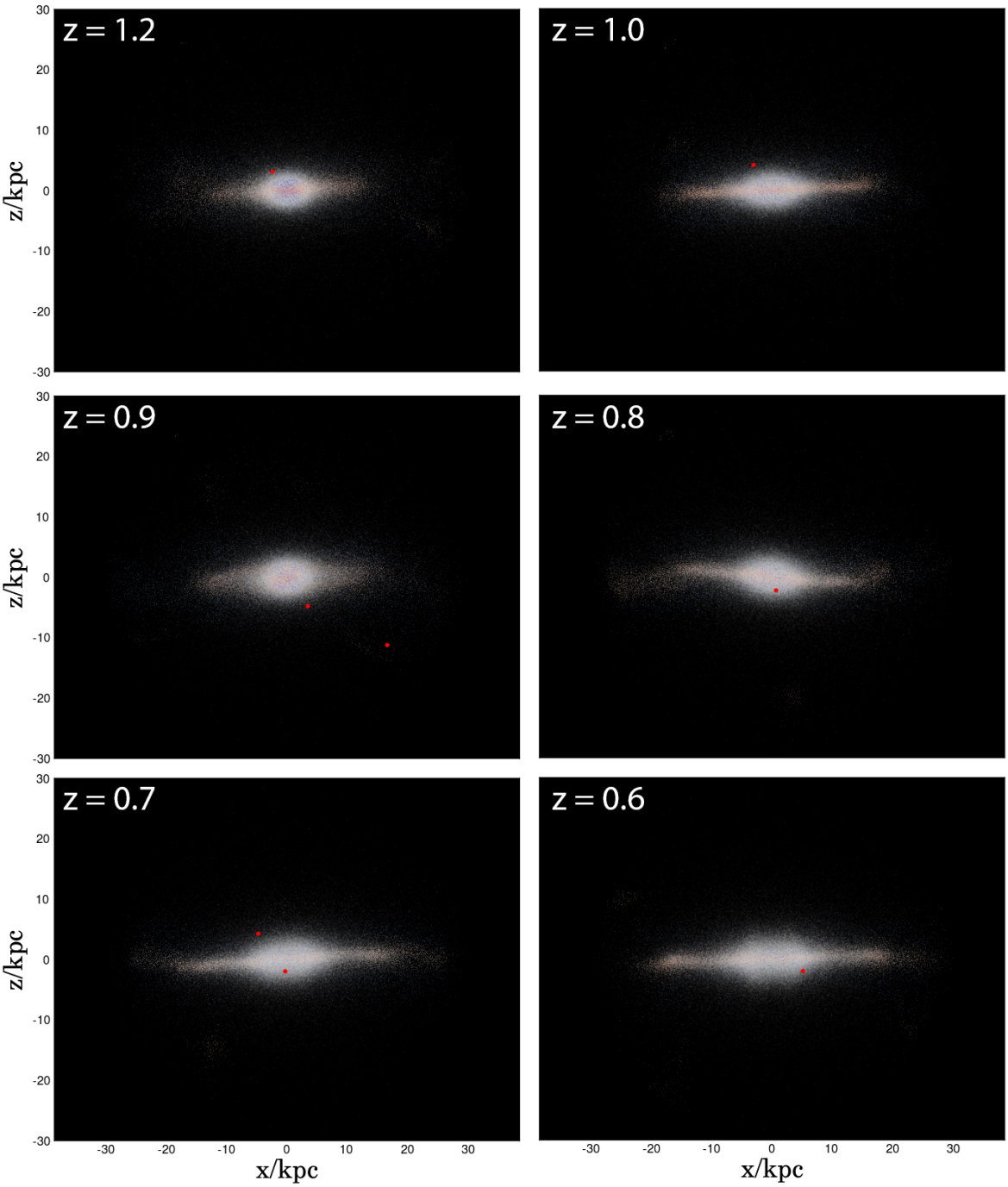

Figure 19: Evolution of the ring galaxy for $z \leq 1.2$ in the edge-on perspective. Stars are white, cold gas is blue and hot gas is red. The large red dots mark the positions of the black holes.

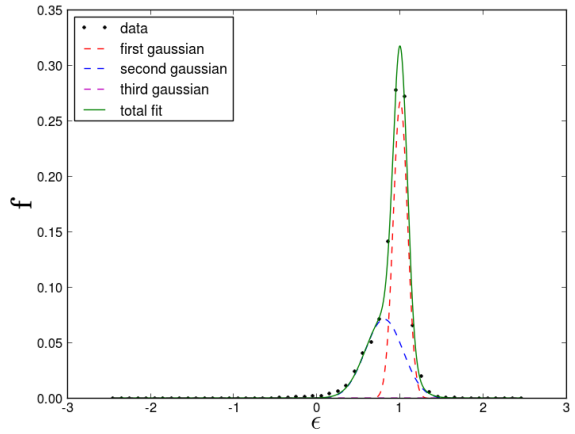

(a) circularitiy distribution of the cold gas

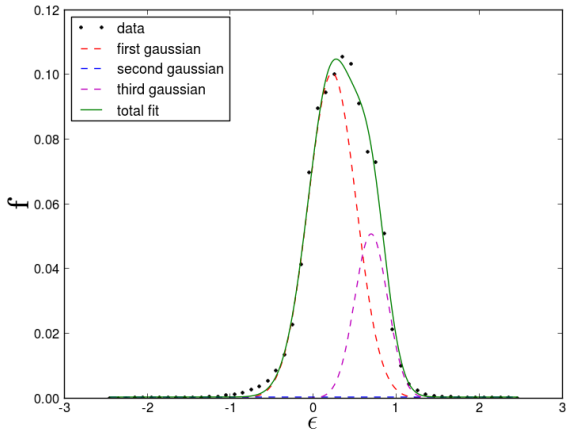

(b) circularity distribution of the stars

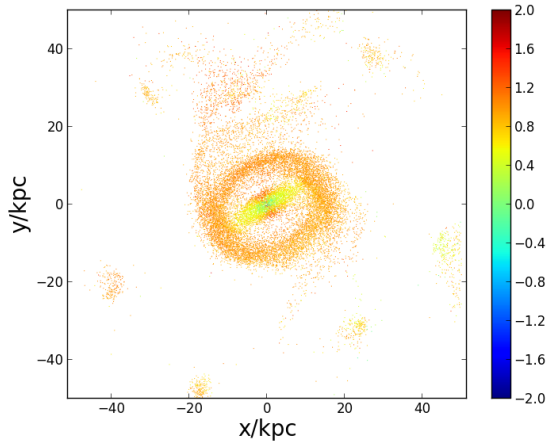

(c) circularity of the cold gas at $z = 1$

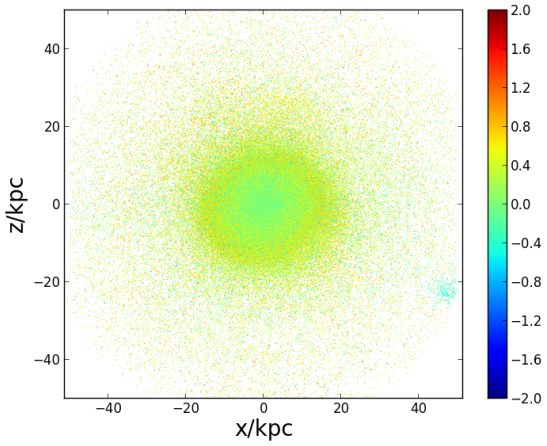

(d) circularity of the stars at $z = 1$

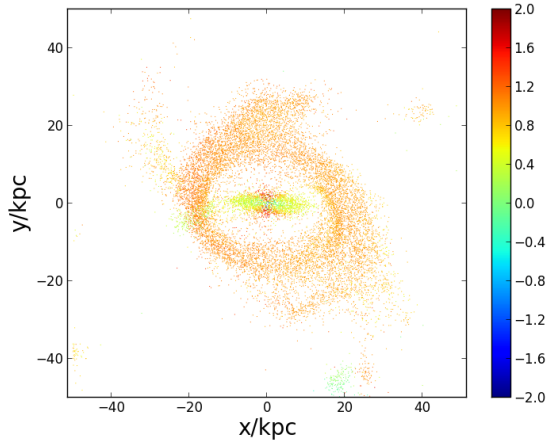

(e) circularity of the cold gas at $z = 0.6$

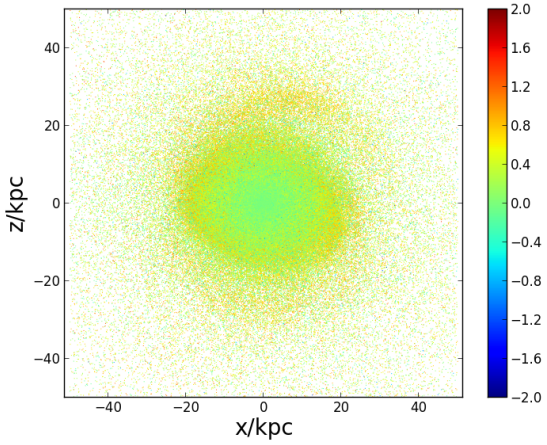

(f) circularity of the stars at $z = 0.6$

Figure 20: Circularities of the ring galaxy. The upper panels show the distributions of the epsilon values at $z = 1$. The lower panels show the face-on perspective with the epsilon values on the color bar at $z = 1$ and $z = 0.6$.

5.3.2 Dynamical Analysis

One way to study the dynamics of a galaxy is to look at the circularities of the particles as described in section 14. The circularity distribution of the cold gas is plotted in figure 20 (a). It shows a clear peak at $\epsilon \approx 1$. Figure 20 (c) shows that these values belong to the particles in the ring. So the particles move on the ring around the center of the galaxy. In the bar the mean value is around $\epsilon = 0.8$ and the range of epsilon values is much larger. In the distribution in figure 20 (a) this is represented by the standard deviation of the second Gaussian. Figure 20 (c) also shows that the circularities in the middle of the bar are much lower than at its edge. There the particles have the same circularities as in the ring. So these particles follow the rotation of the bar.
The stars have two different components. The larger one has a peak near $\epsilon = 0$ constituting an elliptical structure. The small shift of the peak towards $\epsilon = 1$ might be a fingerprint of the cold gas. The smaller Gaussian shows that there are also stars belonging to the ring as shown by figure 20 (d). Here the particles in the region of the ring have a higher circularity than in the central parts.
Now the question is how the circularities evolve during time. The figures 20 (e) and (f) show the circularities of the cold gas and the stars at $z = 0.6$. As expected, there is less cold gas available than at $z = 1$ due to star formation. Consequently the ring and the two spiral arms are very well visible in the stellar component.
It is also interesting to investigate how the bar evolves: The radius of the ring and the gap between the ring and the bulge have become bigger since $z = 1$. Furthermore, the two parts of the cold gas at the edges of the bar with $\epsilon \approx 1$ in figure 20 (c) have moved inwards. Here the circularities are even larger than 1.0. So the angular momentum is larger than it would be if the gas particles moved on a circle. This means that the gas moves towards the center. Moreover, the particles with smaller circularities are further outside. This leads to the box-shaped structure, which can be seen in the last panel of figure 19.
Another common method to study the dynamics of galaxies is to analyse the velocities and the velocity dispersions. Figure 21 shows the mean velocity and the mean velocity dispersion for the face-on perspective in grid cells of the size 1kpc^2. The mean velocity dispersion was calculated for all grid cells containing five or more particles.
The differences of the velocity in the upper right and lower left part of the disk show that the ring lies not exactly in the x-y-plane. The face-on perspective was calculated by maximizing the angular momentum in z-direction. These very small differences could be an effect of precession.

The velocity dispersion of the cold gas is much larger in the bulge than it is in the ring. This leaves a mark in the velocity dispersion of the stars. Here one can see a ring, which is not visible in the velocity map of the stars. The black holes are not found to have a significant impact on the velocity dispersion.

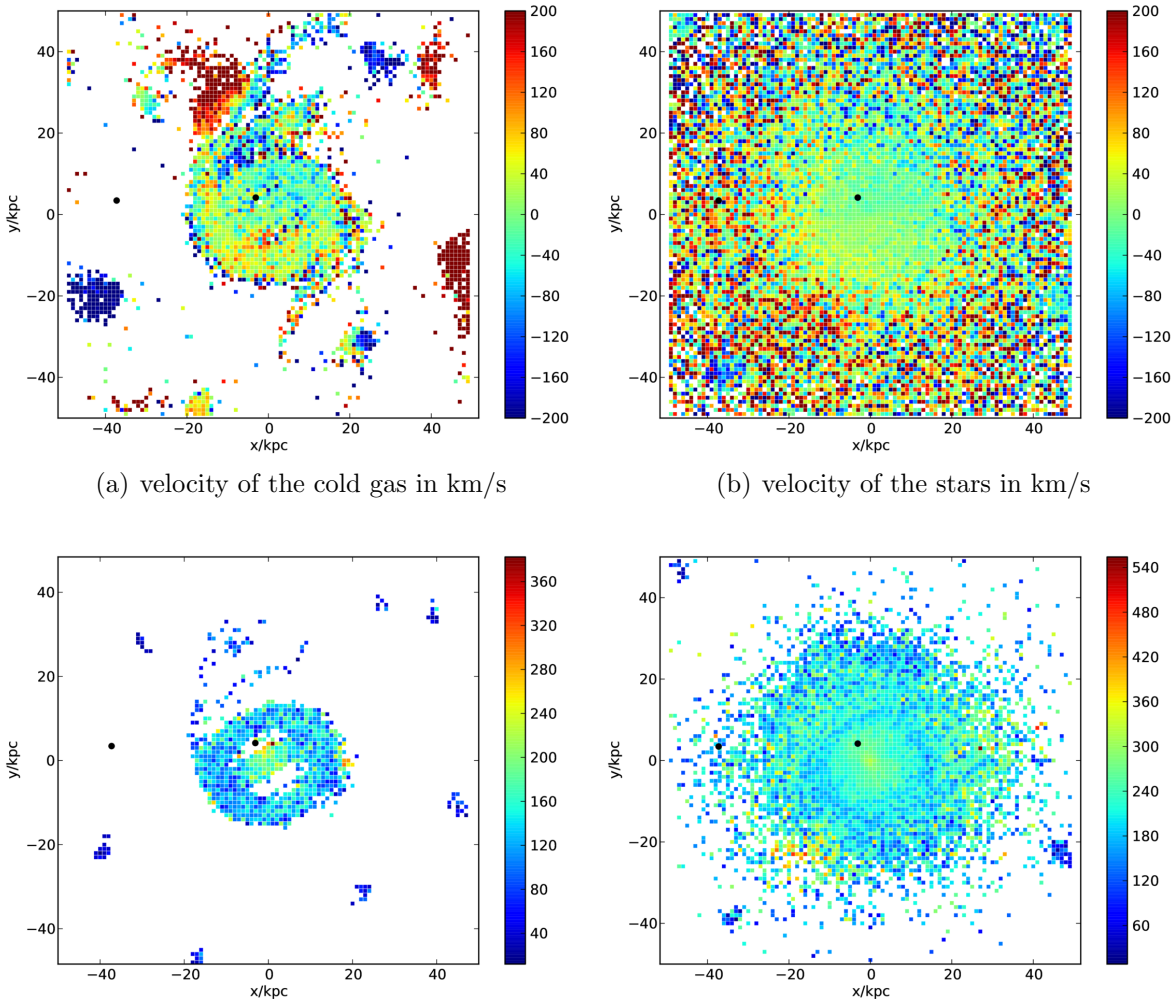

(a) velocity of the cold gas in km/s

(b) velocity of the stars in km/s

(c) velocity dispersion of the cold gas in km/s

(d) velocity dispersion of the stars in km/s

Figure 21: Velocity and velocity dispersion of the stars and the cold gas of the ring galaxy in the x-y-plane at $z = 1$. The black dots represent the black holes.

5.4 The M-σ-Relation

One fundamental relation between black holes and their host galaxies is the M-σ-relation. It has been found by several authors. There are discrepancies between different observational results. For example, Binney & Tremaine (2008) found

$$\log_{10}\left(\frac{M_{\mathrm{bh}}}{M_{\odot}}\right) = 4.0 \cdot \log_{10}\left(\frac{\sigma}{200km/s}\right) + 8.2, \tag{81}$$

whereas McConnell & Ma (2013) derived

$$\log_{10}\left(\frac{M_{\mathrm{bh}}}{M_{\odot}}\right) = 5.06 \cdot \log_{10}\left(\frac{\sigma}{200\mathrm{km/s}}\right) + 8.07. \tag{82}$$

Churazov et al. (2005) could confirm the M-σ-relation theoretically. They introduced a feedback model which differs from the model described in section 3.3.4 such that the feedback is splitted into two components:

- **Outflow:** The outflow is a mechanical feedback, which dominates at accretion rates below $\sim 0.01\dot{M}_{\mathrm{Edd}}$ and is getting very low above $\sim 0.1\dot{M}_{\mathrm{Edd}}$. Its power is the gas heating power
$$P_{\mathrm{o}} = \epsilon_{\mathrm{o}}\dot{M}_{\mathrm{B}}c^2, \tag{83}$$
where ϵ_{o} is the outflow efficiency.

- **Radiation:** The radiation dominates near the Eddington limit and has the luminosity
$$L = \epsilon_{\mathrm{r}}\dot{M}_B c^2. \tag{84}$$

Churazov et al. (2005) proposed that when a black hole accretes at the Eddington rate, it is in equilibrium with the surrounding gas. This means that the cooling loss

$$C \approx \frac{3}{2}kT\frac{\dot{M}_{\mathrm{cool}}}{\mu m_{\mathrm{p}}} \tag{85}$$

and the outflow power P_{o} of the AGN feedback are equal:

$$\epsilon_{\mathrm{o}}c^2\dot{M}_{\mathrm{Edd}} \approx \frac{3}{2}kT\frac{\dot{M}_{\mathrm{cool}}}{\mu m_{\mathrm{p}}} \tag{86}$$

with

$$\dot{M}_{\rm cool} = \frac{2}{\sqrt{3\pi}} \frac{f_{\rm gas}^{3/2} \sigma^2 \Lambda(T)^{1/2}}{m_{\rm p} G^{3/2} t^{1/2}} \tag{87}$$

(White & Frenk 1991). $\mu m_{\rm p}$ is the mean molecular weight with the proton mass $m_{\rm p} = 1.6726 \cdot 10^{24}$g and $\mu \approx 1$. $k = 1.38066 \cdot 10^{-16}$erg K^{-1} is the Boltzmann constant, $\sigma_{\rm T} = 6.6525 \cdot 10^{-25}$cm^2 the Thompson scattering cross section, $c = 2.9979 \cdot 10^{10}$cm s^{-1} the speed of light and $G = 2.9979 \cdot 10^{10}$cm^{3}g^{-1}s^{-2} is the gravitational constant. For the gas fraction $f_{\rm gas}$ the cosmic baryon fraction 0.17 was used. Inserting the equations (71) and (87) into equation (86) gives

$$\epsilon_{\rm o} c^2 \frac{4\pi G M_{\rm bh} m_{\rm p}}{\eta \sigma_{\rm T} c} \approx \frac{3}{2} \frac{kT}{\mu m_{\rm p}} \frac{2}{\sqrt{3\pi}} \frac{f_{\rm gas}^{3/2} \sigma^2 \Lambda(T)^{1/2}}{m_{\rm p} G^{3/2} t^{1/2}}. \tag{88}$$

$$\Leftrightarrow M_{\rm bh} \approx \frac{\eta}{\epsilon_{\rm o}} \frac{3}{4\pi\sqrt{3\pi}} \frac{k \sigma_{\rm T} f_{\rm gas}^{3/2} \sigma^2}{c G m_{\rm p}^3 G^{3/2}} \frac{T \Lambda(T)^{1/2}}{t^{1/2}} \tag{89}$$

Churazov et al. (2005) use $\Lambda(T) = \Lambda_{23} \cdot 10^{-23}$erg s^{-1} cm^{-3}, $\sigma = \sigma_{200} \cdot 200$ km s^{-1} and $t = t_9 \cdot 10^9$yr. They assume $T \approx 3 \cdot 10^6 \sigma_{200}^2$K, which is the virial Temperature. Equation (89) then can be written as

$$\frac{M_{\rm bh}}{10^8 M_\odot} \approx \frac{\eta}{\epsilon_{\rm o}} \cdot 3.3 \cdot 10^{-4} \cdot \Lambda_{23}(T)^{1/2} t_9^{-1/2} \sigma_{200}^4. \tag{90}$$

This is comparable to the M-σ-relation of Binney & Tremaine (2008). Equation (81) can be written as

$$\frac{M_{\rm bh}}{10^8 M_\odot} \approx 2.26 \cdot \sigma_{200}^4. \tag{91}$$

Thus, the M-σ-relation is fulfilled when black holes accrete with the Eddington accretion rate and $\eta/\epsilon_{\rm o}$ is constant:

$$\frac{\eta}{\epsilon_{\rm o}} \approx 6.85 \cdot 10^3. \tag{92}$$

Figure 22 shows the M-σ-relation of Box4 uhr for $z = 0.6$. In figure 22 (a) black holes which are less than 20 kpc away from the center were plotted. Due to the black hole seeding, there are many low mass black holes, which can be neglected. But there are also larger black holes which lie below the relation. In these cases, the black holes might not have evolved correctly. In figure 22 (b) only black holes which are less than 5 kpc away from the center were plotted. Here, less objects are below the relation. This means

that there are several black holes, which are not in the center of the galaxy and thus can not accrete enough matter. In figure 22 (b) most of the other black holes lie above the relation observed by McConnell & Ma (2013). So the velocity dispersions are too low.
As already mentioned there are many different observational estimations of the M-σ-relation. Kormendy & Ho (2013) showed that the scattering around the relation is large and depends on the type of the galaxy and the bulge. By comparing the Magneticum simulation with the results of Binney & Tremaine (2008) there is a better agreement confirming the calculation by Churazov et al. (2005). But the velocity dispersions still are far too high. Perhaps, the resolution does not allow a correct prediction of the velocity dispersions.
The color bar shows the fraction of mass in a disk due to the method described in section 5.2.3. There are a few high mass black holes in disks which lie clearly above the relation. In this region the black holes in ellipticals are in much better agreement with the observations. So the problem of too low velocity dispersions appears mainly in disks. One can also see that mainly black holes with masses below $10^8 M_\odot$ in disks are far away from the center.

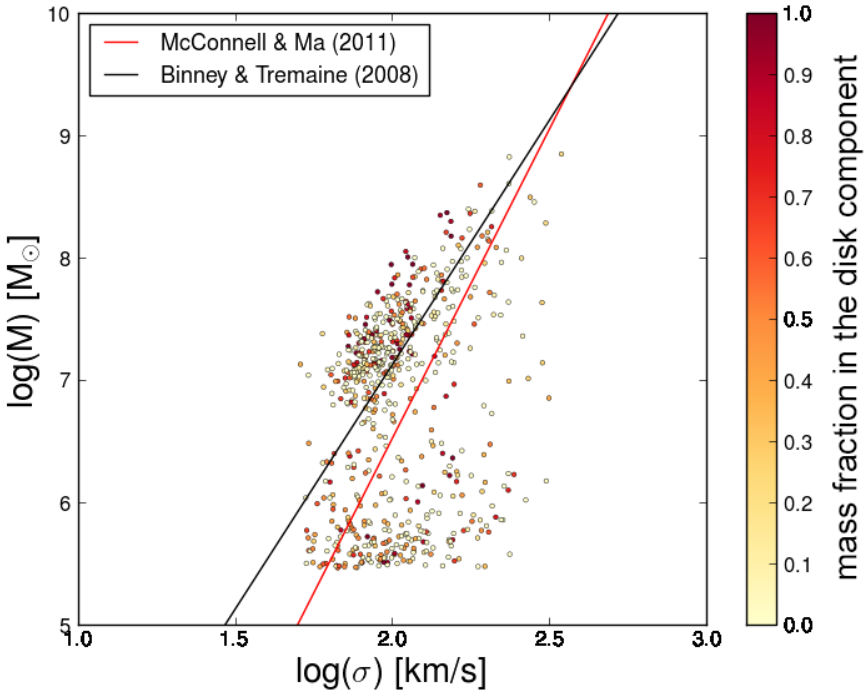

(a) less than 20 kpc away from the center

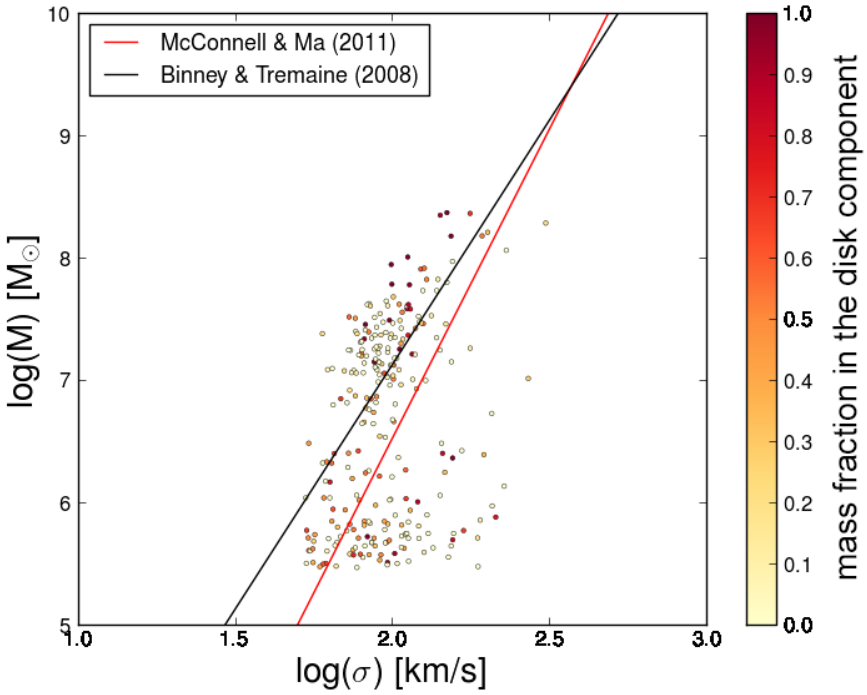

(b) less than 5 kpc away from the center

Figure 22: M-sigma-relation for Box4 uhr at $z = 0.6$. The color bar represents the amount of mass inside a disk component.

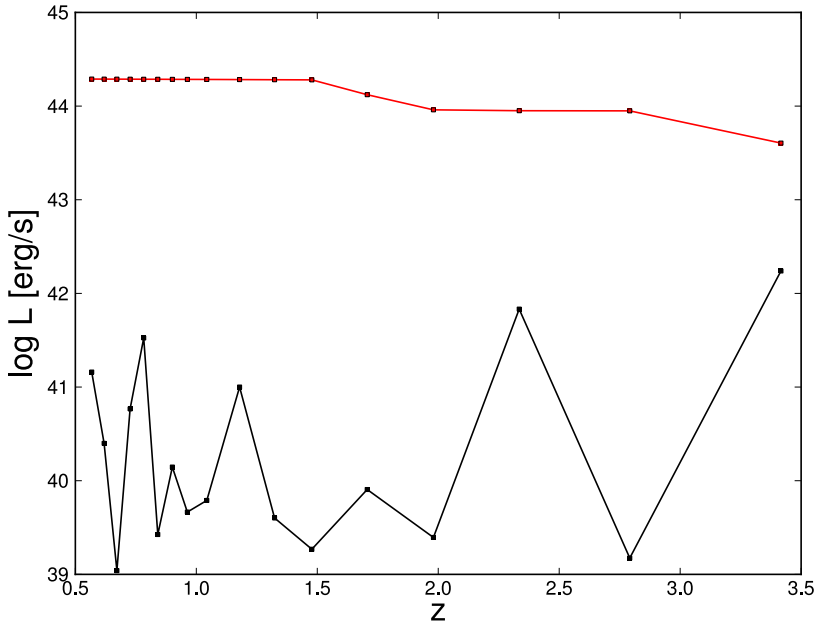

Figure 23: Light curve (black) and Eddington luminosity (red) of the black hole which is the central one of the ring galaxy at redshift $z \approx 0.6$

6 AGN Trigger Mechanisms

To understand the processes driving gas into the centers of galaxies and thus feeding their black holes and triggering AGN activity, the mass and luminosity evolution of single black holes as well as the merger history have to be studied. For this analysis, the IDs of the central black holes were traced backwards in time so that the evolution of the luminosity and the black hole masses could be studied.

Figure 23 shows the light curve of the central black hole of the ring galaxy. It is conspicuous that there are many fluctuations in the light curve. But the luminosity is relatively low, not larger than $2 \cdot 10^{42}$erg/s.

The mass of the black hole is plotted in figure 24. In agreement with the small luminosity, the mass growth is also low. The black hole mainly grows in two eras. The first one is between $1.5 \lesssim z \lesssim 2.0$ and the second one for $z \gtrsim 2.8$. At first sight there seems to be no connection between these growth eras and the peaks in the light curve.

For further conclusions, one has to take the distance to the halo center into account. For most cases the black holes are not in the center and sometimes even move far away from it. So it might be possible that a black hole can not accrete enough matter because there are too few surrounding particles. The distance to the halo center as well as the distance

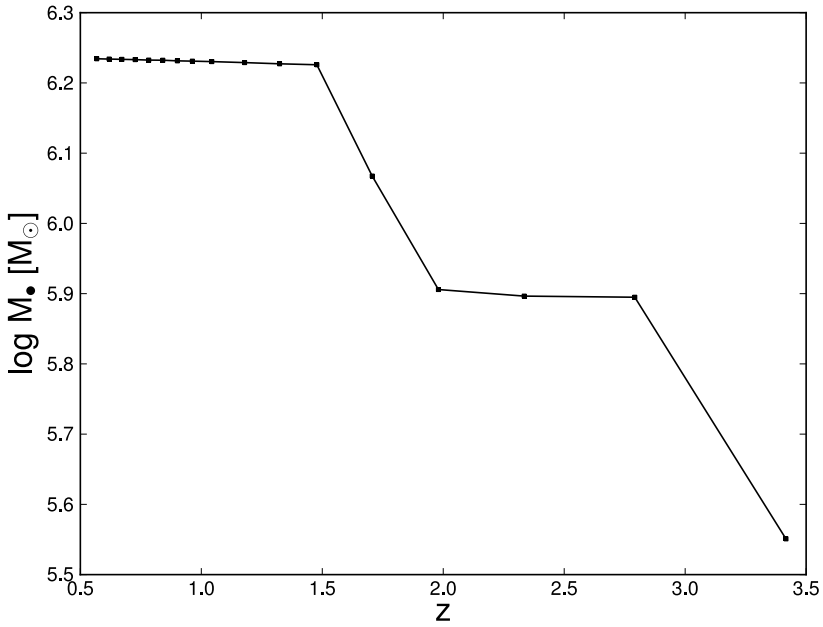

Figure 24: Mass of the black hole which is the central one of the ring galaxy at redshift $z \approx 0.6$

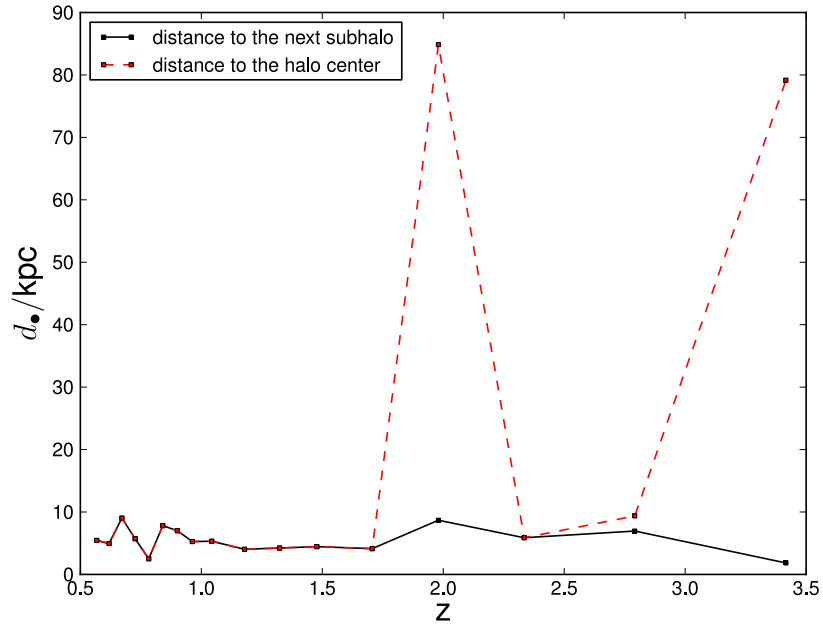

Figure 25: Distance to the halo center of the black hole which is the central one of the ring galaxy at redshift $z \approx 0.6$.

to the next subhalo are plotted in figure 25. There are two large peaks at $z \approx 2.0$ and $z \approx 3.4$. These peaks appear only in the distance to the halo center but not in the distance to the center of the next subhalo. The reason for these peaks are major mergers because just before a merger event the halo contains two major subhalos. At such a peak another subhalo was chosen as the central one than the one before. The two peaks appear exactly when the two main mass gains in figure 24 start. This means that the main growths of black holes is due to merger events.

With that knowledge in mind it is obvious to argue that the fluctuations in the luminosity for $z \lesssim 1.5$ might also be the consequence of merger events. This would also explain the fluctuations of the distance to the center. By taking a closer look on figure 23 and 25 one can conclude that a maximum in the distance often causes a minimum in the light curve and a minimum in the distance leads to a maximum in the light curve. This was expected because there is generally more gas at the center which can be accreted. But probably this is not describing reality because the black hole is too far away from the center.

Figure 26 shows two other examples which describe a strong connection between the mass growth of the black hole and mergers. The example on the right side shows a clear mass growth during the merger at $z \approx 0.8$. Right after the merger event there is a large peak in the luminosity. This is another example for an AGN driven by a major merger. Before the merger, there is a continuous mass growth which might be driven by smooth gas accretion. It is also connected to the luminosity because the AGN is brighter for $z \gtrsim 2.5$ when the mass growth is larger.

In figure 26 (b) there is a peak in the luminosity at redshift $z \approx 0.8$ which does not correlate with the distance. Figure 27 shows the halo right before the peak. Evidently, there is a merger which increases the luminosity. The distance of the black hole to the center does not change much during the merger because it belongs to the more massive galaxy. The mass of the black hole increases somewhat. This is further evidence for a merger driven black hole growth.

The left panels in figure 28 depict the mass growth of a very massive black hole which is also merger driven. Figure 29 shows the evolution of this halo for $z \geq 0.9$. It was traced back by searching the ID of the central black hole (pink circles). All black holes are marked with red dots. In figure 29 at $z = 1.71$ one can observe the in-fall of the substructure which is between 60 and 70 kpc away from the center. After the merger the black hole is thrown outwards. This is also seen due to the strong decrease of the luminosity. Later it falls back into the center. As in the previous examples, this leads to

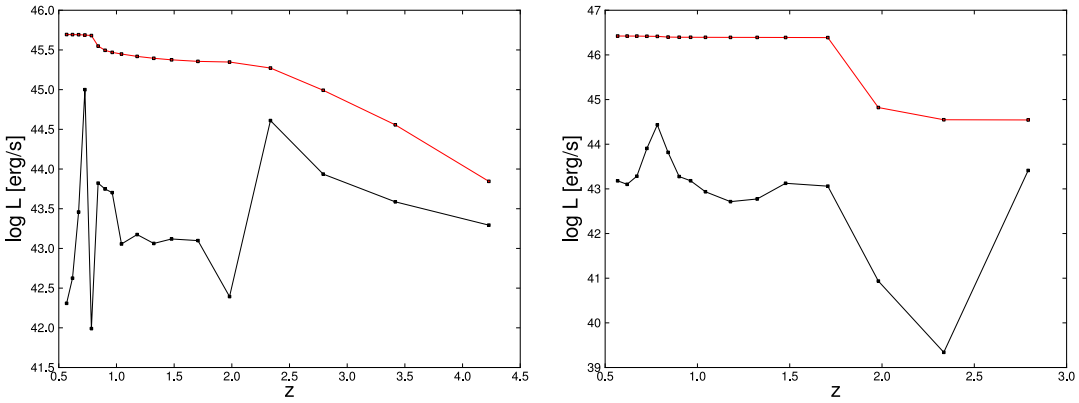

(a) light curve (black) and L_{Edd} (red)

(b) light curve (black) and L_{Edd} (red)

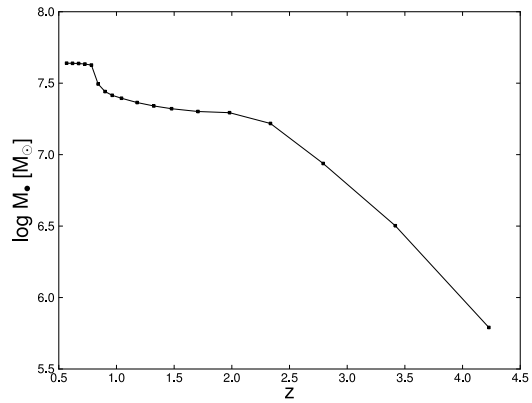

(c) mass

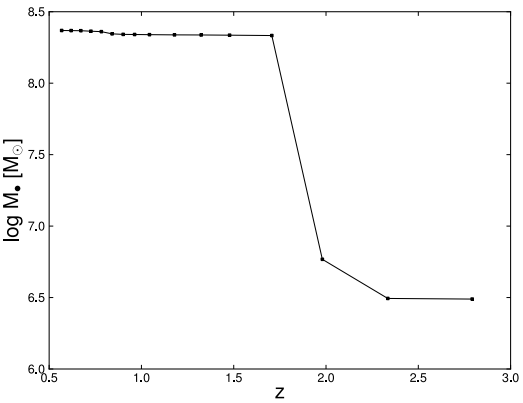

(d) mass

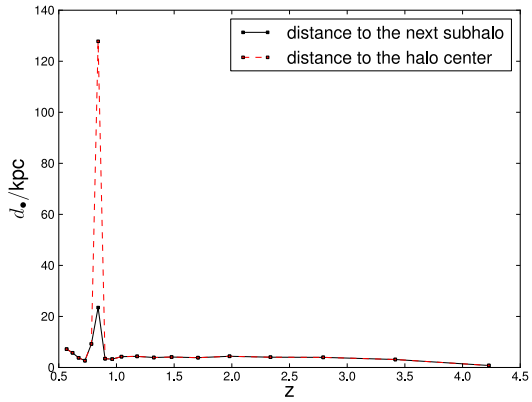

(e) distance

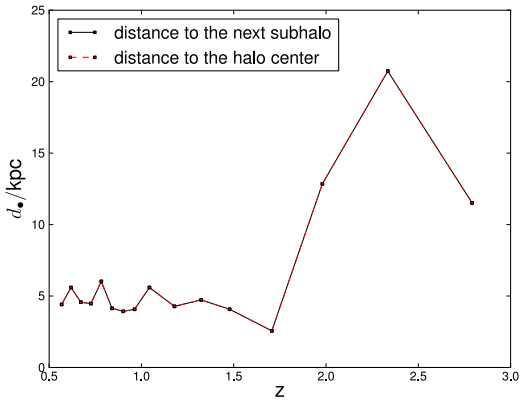

(f) distance

Figure 26: Comparison of the light curve, the mass and the distance to the halo center for two different halos.

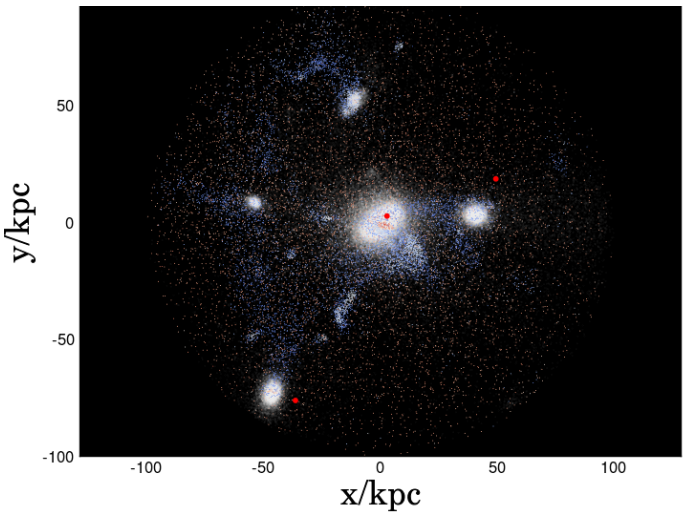

Figure 27: Black holes (red), stars (white), cold gas (blue) and hot gas (red) of the galaxy belonging to the right panels in figure 26 at redshift $z = 0.84$.

a rapid mass growth and to a very high luminosity. Afterwards the luminosity decreases. Between $z = 0.84$ and $z = 0.90$ there is a smaller jump in the mass. This is probably due to the in-fall of a smaller substructure as one can see in figure 29 at $z = 0.90$. The merger shown at $z = 0.96$ causes only a small mass growth.
The right side of figure 28 shows another example for a continuous mass growth. There are a few large peaks in the light curve which are connected to the distance to the center. So the mass growth might be the consequence of minor mergers and smooth gas accretion.
Overall the results of this section can be summarized as follows:

- Very luminous AGN are major merger driven. This is in agreement with recent studies, e.g. by Hirschmann et al. (2012) and Hayward et al. (2013). In observational studies, e.g. by Hopkins et al. (2008) and Silverman et al. (2011) a higher AGN fraction is also found in pairs of galaxies.

- Fainter AGN can be triggered by major or minor mergers as well as by smooth gas accretion. The fact that they are not necessarily merger driven is explained by observational studies finding a large fraction of moderately luminous AGN without a significant merger event. For example, 85% of the galaxies with AGN observed by Cisternas et al. (2011) show no distortion. In this respect, a further statistical analysis for AGN trigger mechanisms will be needed.

- Smooth gas accretion can explain a continuous mass growth but it is not able to produce large black hole masses.

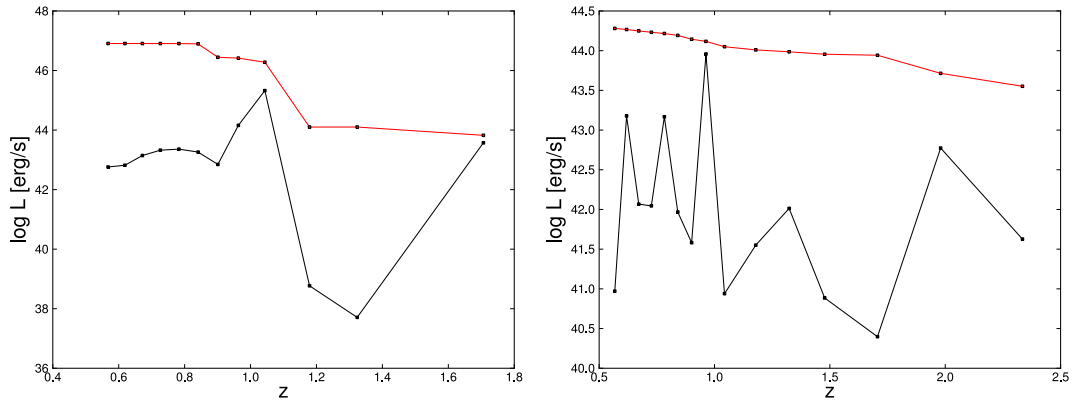

(a) light curve (black) and $L_{\rm Edd}$ (red)

(b) light curve (black) and $L_{\rm Edd}$ (red)

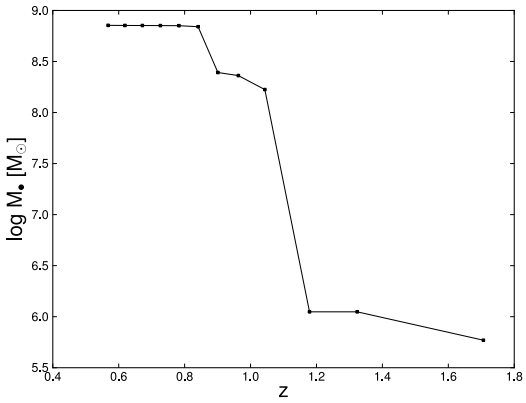

(c) mass

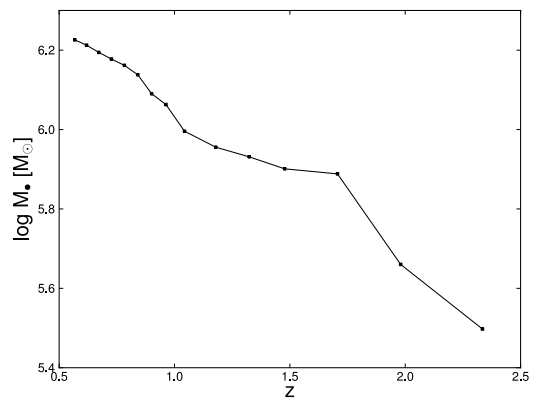

(d) mass

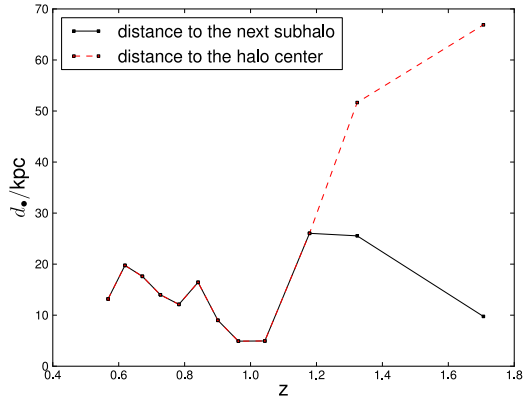

(e) distance

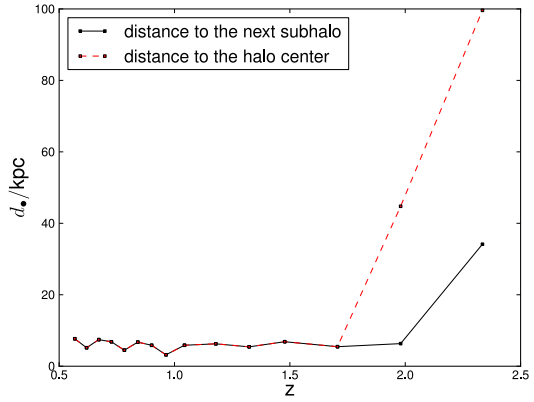

(f) distance

Figure 28: Comparison of the light curve, the mass and the distance to the halo center of a very massive black hole (left) and a black hole with a varying luminosity triggered by minor mergers or smooth gas accretion (right).

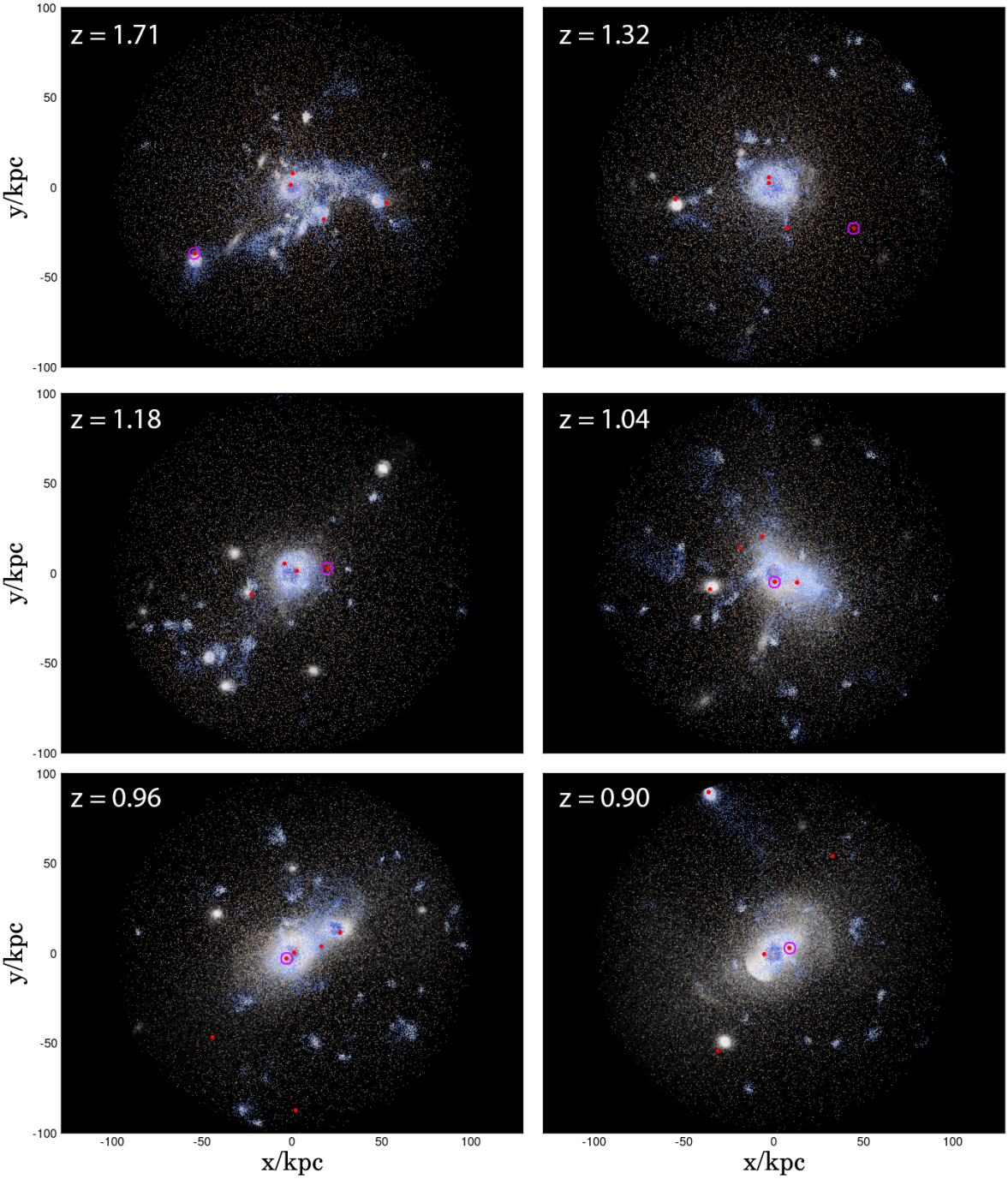

Figure 29: Evolution of a very massive halo for $z \geq 0.9$. The figures show the stars (white), hot gas (red) and cold gas (blue). The red dots represent the black holes. The ones marked with the pink circles belong to the left panel of figure 28.

7 Parameterstudy

In this thesis two problems of the black hole model used until today have already been mentioned:

- In section 3.3.4 it is described that the choice of the values for ϵ_r and ϵ_f is still unclear.
- In section 3.3.2 it is mentioned that $\dot{M}_B$ is multiplied by a boost factor α. The physical or numerical origin of this parameter is still a matter of debate.

These problems are discussed in more detail in this section. For this analysis, Box4 hr was used to perform several test runs to study the influence of different parameters regulating black hole growth onto the properties of the black holes and their host galaxies. Testing the quality of a simulation, the relation between the black hole mass and the stellar mass of the bulge was used as an observational constraint. Here we use the result of McConnell & Ma (2013):

$$\log_{10}\left(\frac{M_\mathrm{bh}}{M_\odot}\right) = 1.05 \cdot \log_{10}\left(\frac{M_*}{10^{11} M_\odot}\right) + 8.46. \tag{93}$$

Another indicator for the reliability of the simulation are the stellar mass functions (SMFs) at different redshifts, which describe the amount of galaxies of a certain stellar mass M_*, observed amongst others by Muzzin et al. (2013). In their studies, the SMFs are characterized by a Schechter function (Schechter, 1976):

$$\Phi(M) = (\ln 10)\hat{\Phi}[10^{(M-\hat{M})(1+\alpha)}] \cdot \exp[-10^{(M-\hat{M})}], \tag{94}$$

where $M = \log(M_*/M_\odot)$, $\hat{M} = \log(\hat{M}_*/M_\odot)$ is the characteristic mass, α is the low-mass-end slope and $\hat{\Phi}$ is the normalization.

7.1 Radiative and Outflow Efficiency

Due to equation (90) the outflow efficiency is indirectly proportional to the black hole mass at the Eddington limit. The parameter η is assumed to be constant and the parameter ϵ_o in the model by Churazov et al. (2005) corresponds to $\epsilon_\mathrm{f}\epsilon_\mathrm{r}$ in equation (74), which was used to calculate the feedback energy in the Magneticum simulations. Thus, if $\dot{M} = \dot{M}_\mathrm{Edd}$, the black hole mass should be reduced by 50% when either ϵ_r or ϵ_f is doubled. This is discussed in section 7.1.1.

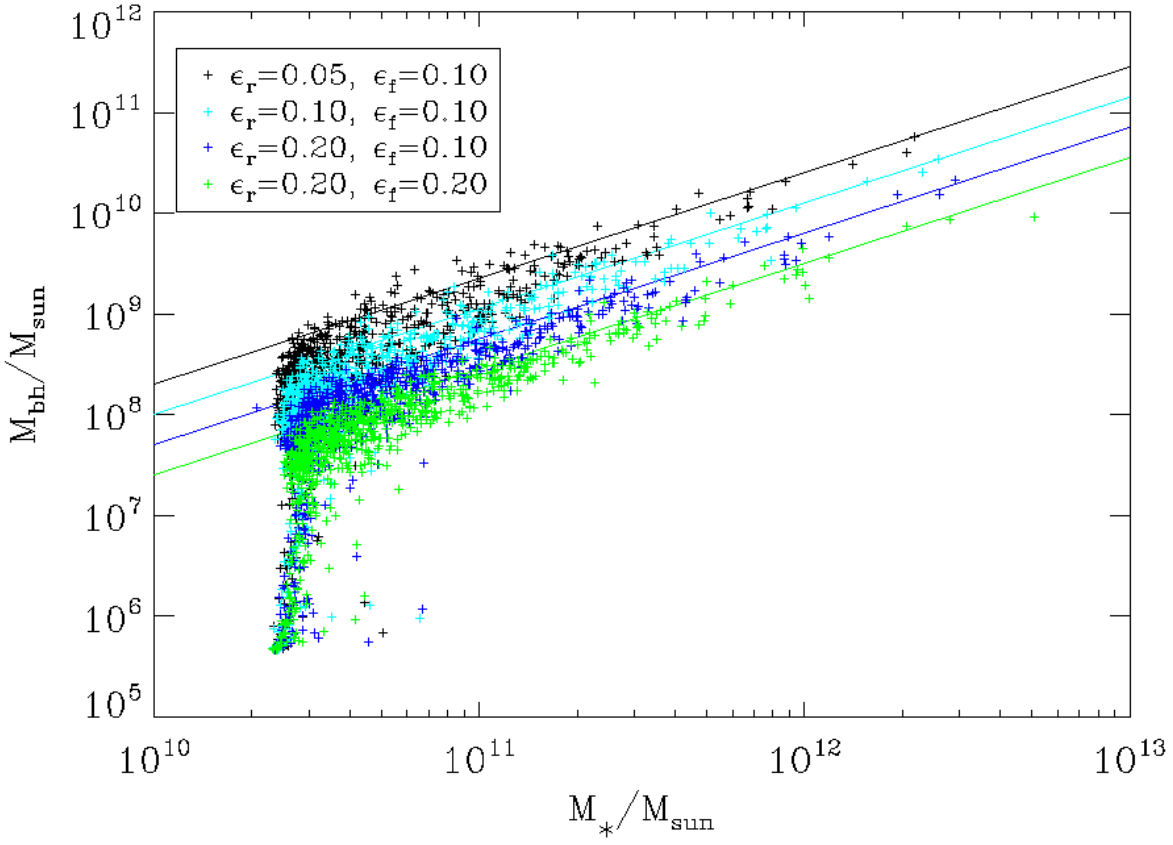

Figure 30: $M_{\rm bh} - M_*$-relation at $z = 0$ for different values for the radiative and the feedback efficiency. The green graph line represents the observational result by McConnell & Ma (2013). This was multiplied by 2 (blue line), 4 (cyan line) and 8 (black line), which are the inverse values by which $\epsilon_{\rm r}\epsilon_{\rm f}$ was changed.

Because of the significant influence of $\epsilon_{\rm r}$ and $\epsilon_{\rm f}$ onto the evolution of black holes and their host galaxies it is worthwhile to have a closer look at these parameters. As it was illustrated in section 2, the radiative efficiency of a black hole depends on its spin and thus on its mass. This was constrained by the observations of Davis & Laor (2011) and Chelouche (2013). In section 7.1.2, the results for such an implementation will be shown and discussed.

7.1.1 Constant Efficiencies

To show the proportionality $M_{\rm bh} \propto (\epsilon_{\rm r}\epsilon_{\rm f})^{-1}$, four simulations with different constant values for $\epsilon_{\rm r}$ and $\epsilon_{\rm f}$ were performed. Figure 30 shows the $M_{\rm bh} - M_*$-relations for these runs. The green graph line corresponds to the results by McConnell & Ma (2013) in equation (93). Obviously, the simulation is in very good agreement with the observations

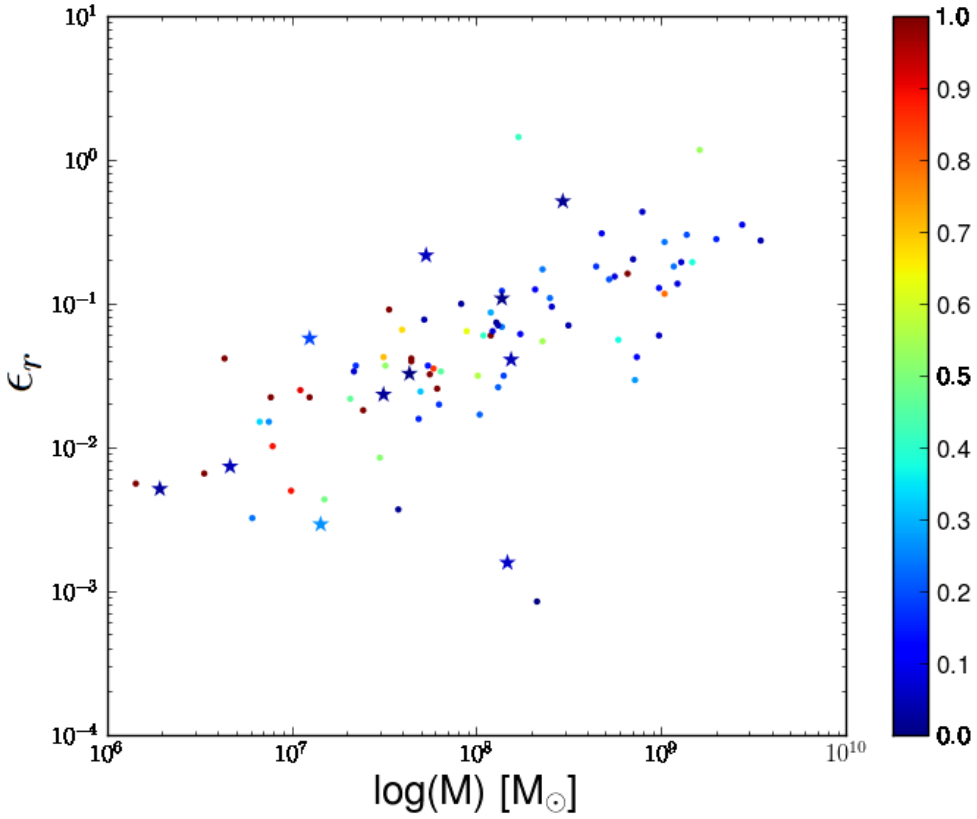

Figure 31: Observations by Davis et al. (2011) (dots) and Chelouche et al. (2013) (stars) of the radiative efficiency over the black hole mass.The color bar represents the Eddington ratio $\dot{M}/\dot{M}_{\rm Edd}$.

for $\epsilon_{\rm r} = 0.20$ and $\epsilon_{\rm f} = 0.20$. This is significantly higher then the values $\epsilon_{\rm r} = 0.05$ and $\epsilon_{\rm f} = 0.10$, which have been originally used by Springel et al. (2005).
Figure 30 shows that the black hole masses are reduced by 50% when either $\epsilon_{\rm r}$ or $\epsilon_{\rm f}$ is doubled. This verifies equation (90).

7.1.2 Mass Dependent Radiative Efficiency

Figure 31 shows observational estimates for the radiative efficiency versus the black hole masses. Davis & Laor (2011) for example find that the radiative efficiency of quasars (illustrated by the dots in figure 31) follows the formula:

$$\epsilon_{\rm r} = 0.089 \left(\frac{M}{10^8 M_\odot} \right)^{0.52} . \tag{95}$$

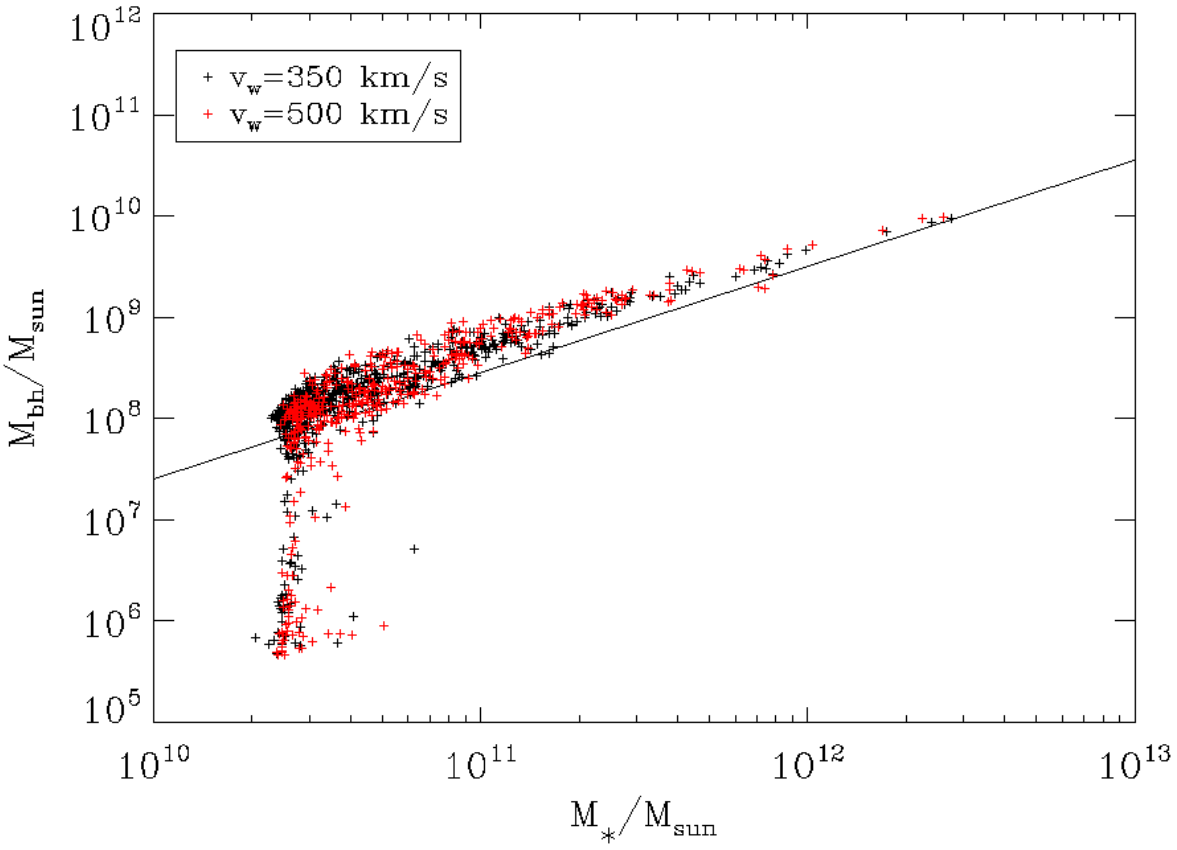

Figure 32: $M_{\mathrm{bh}} - M_*$-relation for a mass dependent radiative efficiency at $z = 0$ for two different wind velocities. The feedback factor is $\epsilon_{\mathrm{f}} = 0.2$. The black graph line corresponds to equation (93).

Chelouche (2013) observed Seyfert 1 galaxies (stars in figure 31) and found that the mass dependency is the same as for quasars.

The color bar in figure 31 represents the Eddington ratio $f_{\mathrm{Edd}} = \dot{M}/\dot{M}_{\mathrm{Edd}}$. It shows that low mass black holes typically have higher Eddington ratios. Due to figure 4 this was expected because with higher mass values more black holes are already relaxed and thus have left the quasar-mode. Nevertheless, the Eddington ratio does not influence the mass dependency.

Thus, it is reasonable to implement equation (95) into the GADGET code. Figure 32 shows the $M_{\mathrm{bh}} - M_*$-relation for the resulting simulation (black crosses). It shows that most black hole masses are slightly too high. For higher stellar masses the simulation is in a better agreement with the observations. Nevertheless, it is an improvement in comparison to figure 30, where only the simulation with $\epsilon_{\mathrm{r}} = 0.2$ is in agreement with the observations. But this value is significantly different from the theoretical (chapter 2)

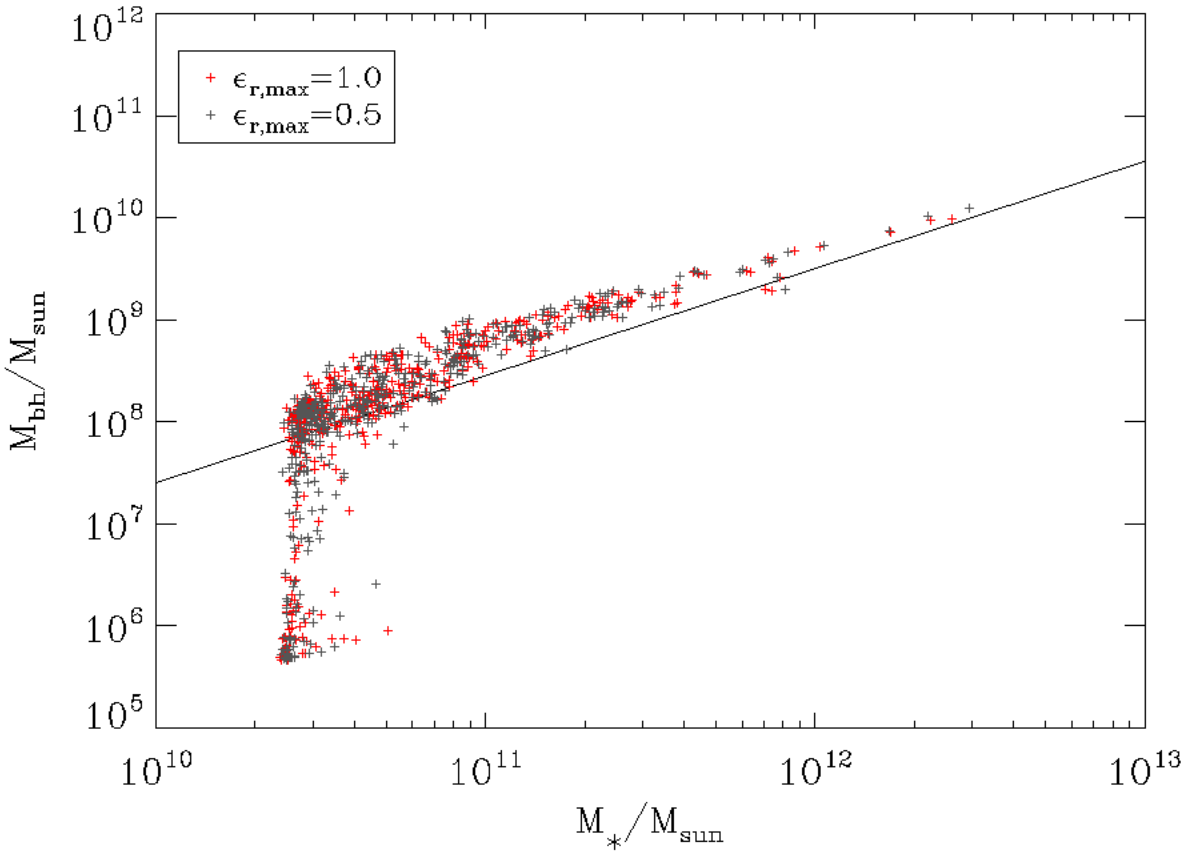

Figure 33: $M_{\rm bh} - M_*$-relation for a mass dependent radiative efficiency at $z = 0$ for two different maximum values. The feedback factor is $\epsilon_{\rm f} = 0.2$ and the wind velocity is $v_{\rm w} = 500$km/s. The black graph line corresponds to equation (93).

and observed (Shakura & Sunyaev, 1973) mean value $\epsilon_{\rm r} = 0.1$.

One possibility to decrease the accretion rate follows from equation (64). By choosing a higher wind velocity $v_{\rm w}$, the gas velocity is increased. The commonly used value is $v_{\rm w} = 350$km/s. The red crosses in figure 32 show the result for $v_{\rm w} = 500$km/s. This indeed can decrease the black hole masses, but only for low stellar masses.

To avoid that $\epsilon_{\rm r}$ is estimated too high, a maximum value has to be defined. Figure 33 shows the $M_{\rm bh} - M_*$-relation for $\epsilon_{\rm r,max} = 1$ and $\epsilon_{\rm r,max} = 0.5$. Obviously, there is no significant difference between these two runs.

Now it is interesting to see how the mass dependent radiative efficiency and the increased wind velocity influence the SMFs at different redshifts. They are plotted for the different runs in figure 34. The dashed graph lines correspond to the Schechter mass functions found observationally by Muzzin et al. (2013), whereas the histograms belong to the simulations. Figure 34 (a) shows the result for a constant radiative efficiency $\epsilon_{\rm r} = 0.2$

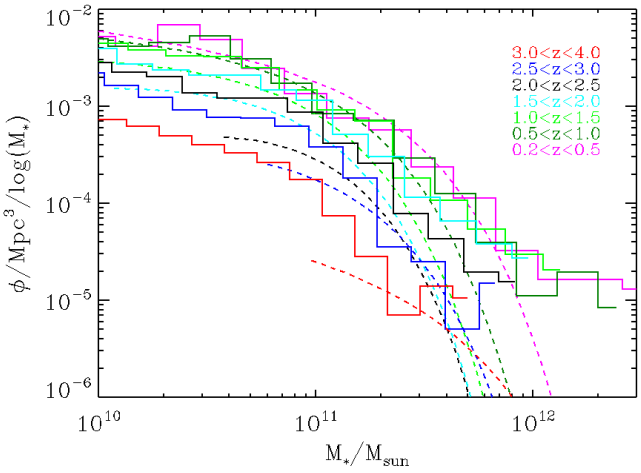

(a) $\epsilon_{\rm r} = 0.2$, $\epsilon_{\rm f} = 0.2$, $v_{\rm w} = 350$km/s

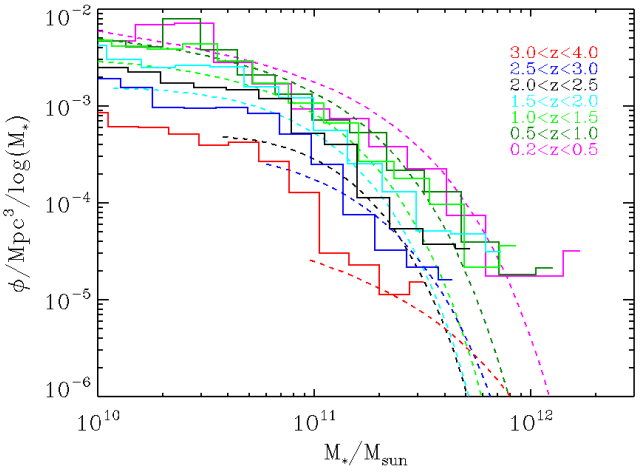

(b) $\epsilon_{\rm r} = \epsilon_{\rm r}(M_{\rm bh})$, $\epsilon_{\rm f} = 0.2$, $v_{\rm w} = 350$km/s

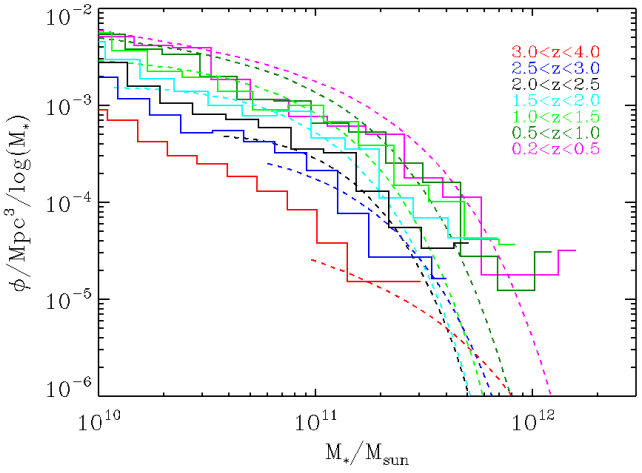

(c) $\epsilon_{\rm r} = \epsilon_{\rm r}(M_{\rm bh})$, $\epsilon_{\rm f} = 0.2$, $v_{\rm w} = 500$km/s

Figure 34: SMFs for three different runs in different redshift ranges. The dotted lines indicate the Schechter mass functions observationally found by Muzzin et al. (2013), whereas the histograms illustrate the simulation results.

and $\epsilon_{\mathrm{f}} = 0.2$, which was found in section 7.1.1. Obviously, there are far too many galaxies at the high mass end as a consequence of a too inefficiently working AGN feedback, especially at low redshifts. Figure 34 (b) shows that the implementation of a mass dependent radiative efficiency can prevent this. Furthermore the SMFs for $z > 1.0$ are in better agreement with the observations when using a mass dependent efficiency. But at lower redshifts there are far too little galaxies in the intermediate mass range, especially for $0.2 < z < 0.5$ the range between $\sim 5 \cdot 10^{10}$ and $\sim 4 \cdot 10^{11}$ is not consistent with the observational results. The higher wind velocity even worsens this problem, which can be seen in figure 34 (c). But in the range $2 \cdot 10^{10} M_{\odot} \lesssim M_{*} \lesssim 10^{11} M_{\odot}$, there are less galaxies. This improves the stellar mass functions for $z \gtrsim 1.0$. To reproduce the low-mass end of the observed SMFs is often found to be a failure in simulations. Only recently researchers have overcome this problem, e.g. Davé et al. (2013) were able to reproduce the observations by using momentum-driven outflows for larger galaxies and energy-driven outflows for dwarf galaxies.

7.2 Accretion Factor

Besides the radiative efficiency there is another parameter, which is not fully understood: the accretion factor α in equation (64). First the arguments by Booth & Schaye (2009) mentioned in section 3.3.2 were tested using the simulation code of this thesis. Secondly, a run with $\alpha = 10$ was performed to study the influence of the accretion factor with respect to the black hole growth.

7.2.1 Phase Diagrams

Booth & Schaye (2009) argued that the accretion rate has to be multiplied by a boost factor due to the limited resolution. Thus, the density ρ near the black hole is underestimated, whereas the temperature T should be overestimated. To verify this statement, the phase diagram of all gas particles was plotted for two boxes with exactly the same settings, but with different resolutions. Therefore runs of Box3 hr and Box4 uhr at $z = 2$ have been analysed as shown in figure 35. Above the density cut between $\rho = 10^{7} M_{\odot}/\mathrm{kpc}^2$ and $\rho = 10^{8} M_{\odot}/\mathrm{kpc}^2$ the gas particles can form stars. The conture plots clearly show the star forming branch in red. These star-forming particles as well as the cold gas particles below $T = 10^{5}\mathrm{K}$ are the most relevant ones for the accretion onto black holes.
Indeed a comparison of these particles in the two phase diagrams at different resolutions confirms the expectations from Booth & Schaye (2009): for the lower resolution the

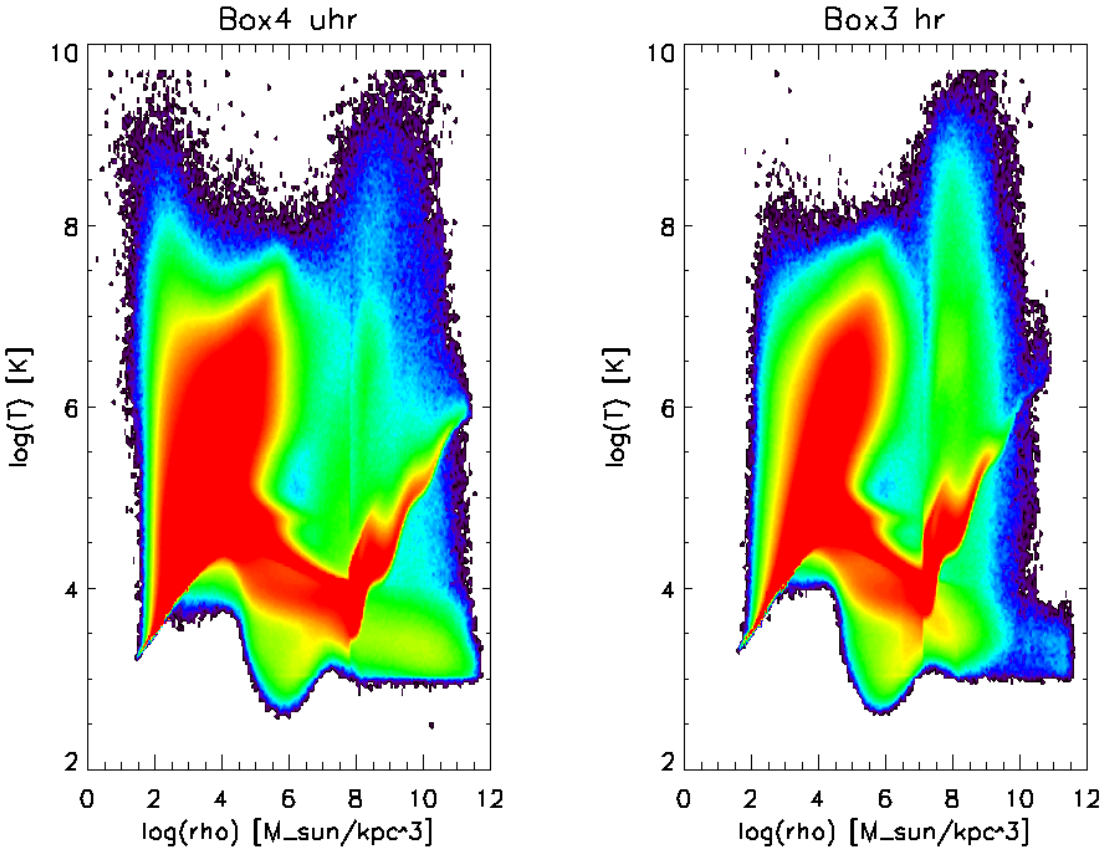

Figure 35: Phase diagrams of all gas particles of Box3 hr and Box4 uhr at $z = 2$.

densities are smaller and the temperatures are slightly higher. This satisfies the usage of the boost factor α. Nevertheless, its value is still unknown.

7.2.2 The Effect of the Accretion Factor onto the Black Hole Growth

To investigate how the value of α influences the black hole growth, a run with $\alpha = 10$ was performed in comparison to the commonly used value $\alpha = 100$. The $M_{\mathrm{bh}} - M_*$-relation for these simulations is plotted in figure 36. Obviously, the simulation with $\alpha = 10$ does not reflect reality, but it illustrates the importance of the right choice of α. It shows that the black holes grow much slower for $\alpha = 10$. Some black holes seem to have stopped growing very early, possibly because they drifted away from the galaxy due to the low mass. Nevertheless, most black holes reach the observed $M_{\mathrm{bh}} - M_*$-relation. Their masses are even in better agreement with the observations. Although the path of the black holes towards the $M_{\mathrm{bh}} - M_*$-relation is different for different boost factors, the influence of α onto the $M_{\mathrm{bh}} - M_*$-relation seems to be very small.
Since α is a parameter which is necessary but not fully understood, it will be important for further research to explore and understand the importance of this parameter. Indeed Gaspari et al. (2013) showed that turbulence might increase the accretion rate by a factor of the order of 100. Since turbulence is only relevant for cold gas it might be necessary to differentiate between hot and cold gas accretion. For hot gas the Bondi model could predict more realistic accretion rates because the assumptions of an isotropical sphere are better fulfilled than for cold gas, which typically falls into the galaxy as streams or clumps. This can be seen e.g. in figure 17.

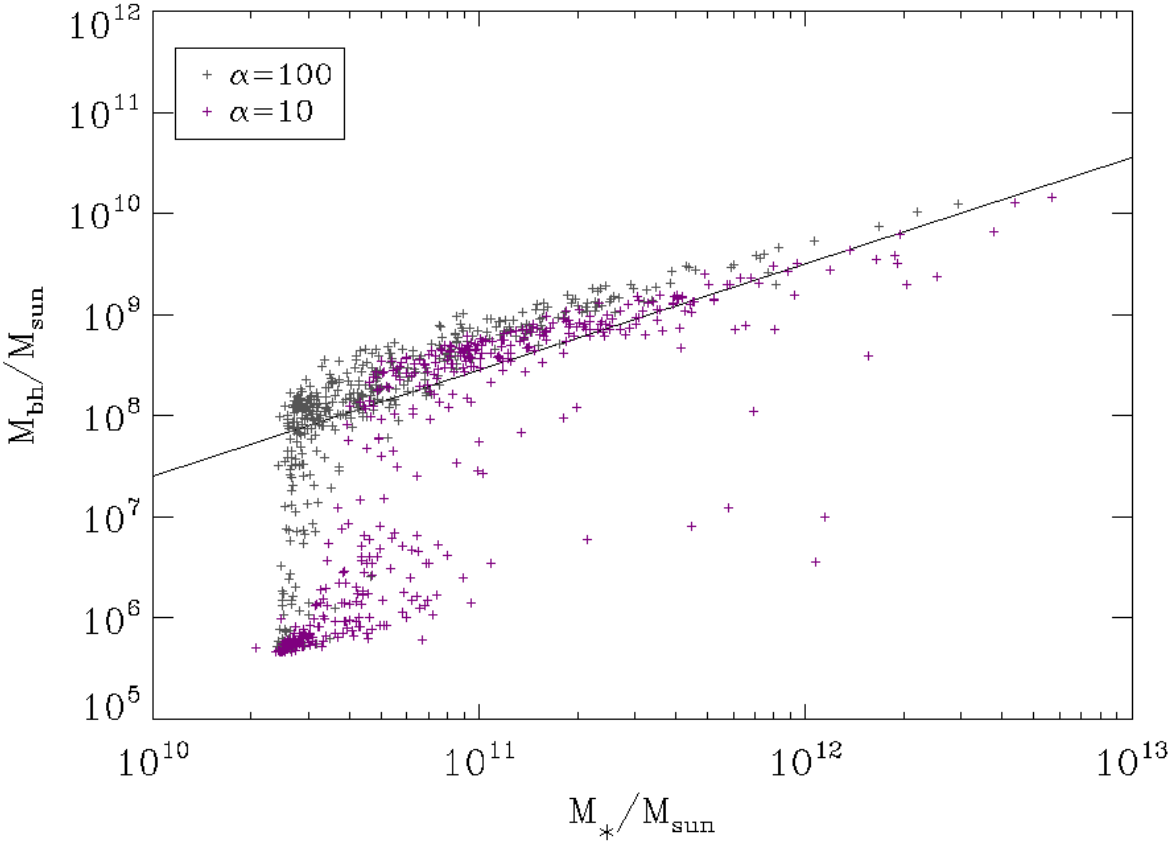

Figure 36: $M_{\mathrm{bh}} - M_*$-relation for at $z = 0$ for two different accretion factors. The black graph line corresponds to equation (93).

8 Conclusions

The results of this thesis contribute to the understanding of black holes and their role during the evolution of galaxies, because the Magneticum simulations afford the largest statistical analysis with respect to black hole growth and AGN evolution (Box3 hr). In a smaller box (Box4 uhr) the resolution is high enough to classify galaxies morphologically and to study AGN trigger mechanisms. Using the smaller box with a lower resolution (Box4 hr) it is possible to perform several test runs and thus to test the influence of different parameters of the black hole model. Therefore, this study contains an analysis of the first implementation of a mass dependent radiative efficiency.
The reliability of the simulations can be verified by reproducing several observational results:

- The bolometric and SXR black hole luminosity functions of the simulation are in reasonably good agreement with the observational data, especially at $z < 1$.
- The observed AGN number density evolution can be reproduced for $L \lesssim 10^{45}$ erg/s and $z \lesssim 2$.
- The Box4 uhr of the Magneticum simulations is successful in forming both disk galaxies and elliptical galaxies.
- By calculating circularities, the morphology of the galaxies in Box4 uhr was classified. The statistical frequency of pure ellipticals and S0 galaxies is similar to the observations by Cappellari et al. (2011).
- After varying the radiative efficiency and the feedback factor, the observed M_{bh}-M_*-relation could be reproduced.
- The stellar mass functions of the simulation are similar to observations. For small redshifts there are discrepancies in the range of $2 \cdot 10^{10} M_\odot \lesssim M_* \lesssim 10^{11} M_\odot$.

Since in simulations the time evolution can be traced, the origin of AGN could be studied:

- The Magneticum simulations reproduce the observed downsizing behaviour successfully, i.e. the black holes grow hierarchically, whereas AGN evolve anti-hierarchically. A comparison of figure 8 and 9 shows that less luminous AGN always occur more frequently, whereas the most frequent black hole masses change with time.

- It could be shown that very luminous AGN are mostly merger triggered. For less luminous AGN this is not necessarily the case, as they can also be triggered by the in-fall of small substructures or smooth gas accretion.

Furthermore, this thesis shows that it is worthwhile to implement more black hole physics into the GADGET code, because the original code contains a simplified black hole model. It contains empirical parameters, which have not been fully understood. But due to the limited resolution, the physics, which can be implemented, is also limited.
In this study, it was shown that the Bondi accretion model predicts too low accretion rates due to the limited resolution and due to the very rough assumption of an isotropical sphere. The Bondi model can be justified only for modelling the hot gas accretion, but not the cold gas accretion, where turbulence may be relevant. Thus, one should differentiate between hot and cold gas during the calculation of the accretion rate and take a closer look at cold gas accretion to find a physical motivation for the boost factor α.
Furthermore, the feedback model can still be improved. The radiative efficiency was originally set to a constant value. Already in this study a dependency on the black hole mass was implemented, which could significantly improve the high mass end of the stellar mass functions.
As a next step the feedback model of Churazov et al. (2005) should be implemented as described in section 5.4. Thus, one could differentiate between mechanical feedback and radiation. The efficiencies would then depend on the accretion rate in terms of $\dot{M}_{\mathrm{Edd}}$.
These implementations would bring the Magneticum simulations forward by another step, because they would both constrain theoretical models and be even more consistent with recent observations.

9 Bibliography

References

H. Alvarez, J. Aparici, J. May, and P. Reich. The radio continuum spectrum of Centaurus A's large-scale components. *A&A*, 355:863–872, March 2000.

J. M. Bardeen, W. H. Press, and S. A. Teukolsky. Rotating Black Holes: Locally Nonrotating Frames, Energy Extraction, and Scalar Synchrotron Radiation. *ApJ*, 178: 347–370, December 1972. doi: 10.1086/151796.

R. Bender, J. Kormendy, and W. Dehnen. Improved Evidence for a 3 x10 6 M_{sun} Black Hole in M32: Canada-France-Hawaii Telescope Spectroscopy with FWHM = 0 -8pt. 47 Resolution. *ApJ*, 464:L123, June 1996. doi: 10.1086/310098.

J. Binney and S. Tremaine. *Galactic Dynamics: Second Edition*. Princeton University Press, 2008.

H. Bondi. On spherically symmetrical accretion. *MNRAS*, 112:195, 1952.

H. Bondi and F. Hoyle. On the mechanism of accretion by stars. *MNRAS*, 104:273, 1944.

C. M. Booth and J. Schaye. Cosmological simulations of the growth of supermassive black holes and feedback from active galactic nuclei: method and tests. *MNRAS*, 398: 53–74, September 2009. doi: 10.1111/j.1365-2966.2009.15043.x.

M. Cappellari, E. Emsellem, D. Krajnović, R. M. McDermid, N. Scott, G. A. Verdoes Kleijn, L. M. Young, K. Alatalo, R. Bacon, L. Blitz, M. Bois, F. Bournaud, M. Bureau, R. L. Davies, T. A. Davis, P. T. de Zeeuw, P.-A. Duc, S. Khochfar, H. Kuntschner, P.-Y. Lablanche, R. Morganti, T. Naab, T. Oosterloo, M. Sarzi, P. Serra, and A.-M. Weijmans. The ATLAS^{3D} project - I. A volume-limited sample of 260 nearby early-type galaxies: science goals and selection criteria. *MNRAS*, 413:813–836, May 2011. doi: 10.1111/j.1365-2966.2010.18174.x.

M. Cappellari, R. M. McDermid, K. Alatalo, L. Blitz, M. Bois, F. Bournaud, M. Bureau, A. F. Crocker, R. L. Davies, T. A. Davis, P. T. de Zeeuw, P.-A. Duc, E. Emsellem, S. Khochfar, D. Krajnović, H. Kuntschner, R. Morganti, T. Naab, T. Oosterloo, M. Sarzi, N. Scott, P. Serra, A.-M. Weijmans, and L. M. Young. The ATLAS^{3D} project - XX. Mass-size and mass-σ distributions of early-type galaxies: bulge fraction drives

kinematics, mass-to-light ratio, molecular gas fraction and stellar initial mass function. *MNRAS*, 432:1862–1893, July 2013. doi: 10.1093/mnras/stt644.

D. Chelouche. The Case for Standard Irradiated Accretion Disks in Active Galactic Nuclei. *ApJ*, 772:9, July 2013. doi: 10.1088/0004-637X/772/1/9.

E. Choi, J. P. Ostriker, T. Naab, and P. H. Johansson. Radiative and Momentum-based Mechanical Active Galactic Nucleus Feedback in a Three-dimensional Galaxy Evolution Code. *ApJ*, 754:125, August 2012. doi: 10.1088/0004-637X/754/2/125.

E. Churazov, S. Sazonov, R. Sunyaev, W. Forman, C. Jones, and H. Böhringer. Supermassive black holes in elliptical galaxies: switching from very bright to very dim. *MNRAS*, 363:L91–L95, October 2005. doi: 10.1111/j.1745-3933.2005.00093.x.

M. Cisternas, K. Jahnke, K. J. Inskip, J. Kartaltepe, A. M. Koekemoer, T. Lisker, A. R. Robaina, M. Scodeggio, K. Sheth, J. R. Trump, R. Andrae, T. Miyaji, E. Lusso, M. Brusa, P. Capak, N. Cappelluti, F. Civano, O. Ilbert, C. D. Impey, A. Leauthaud, S. J. Lilly, M. Salvato, N. Z. Scoville, and Y. Taniguchi. The Bulk of the Black Hole Growth Since z ˜ 1 Occurs in a Secular Universe: No Major Merger-AGN Connection. *ApJ*, 726:57, January 2011. doi: 10.1088/0004-637X/726/2/57.

R. Davé, N. Katz, B. D. Oppenheimer, J. A. Kollmeier, and D. H. Weinberg. The neutral hydrogen content of galaxies in cosmological hydrodynamic simulations. *MNRAS*, 434: 2645–2663, September 2013. doi: 10.1093/mnras/stt1274.

S. W. Davis and A. Laor. The Radiative Efficiency of Accretion Flows in Individual Active Galactic Nuclei. *ApJ*, 728:98, February 2011. doi: 10.1088/0004-637X/728/2/98.

T. Di Matteo, J. Colberg, V. Springel, L. Hernquist, and D. Sijacki. Direct Cosmological Simulations of the Growth of Black Holes and Galaxies. *ApJ*, 676:33–53, March 2008. doi: 10.1086/524921.

K. Dolag, S. Borgani, G. Murante, and V. Springel. Substructures in hydrodynamical cluster simulations. *MNRAS*, 399:497–514, October 2009. doi: 10.1111/j.1365-2966.2009.15034.x.

R. Edgar. A review of Bondi-Hoyle-Lyttleton accretion. *New Astronomy Reviews*, 48: 843–859, September 2004. doi: 10.1016/j.newar.2004.06.001.

A. Einstein. *The Meaning of Relativity*. Princeton University Press, 1955.

D. Fabjan, S. Borgani, L. Tornatore, A. Saro, G. Murante, and K. Dolag. Simulating the effect of active galactic nuclei feedback on the metal enrichment of galaxy clusters. *MNRAS*, 401:1670–1690, January 2010. doi: 10.1111/j.1365-2966.2009.15794.x.

D. B. Fisher, N. Drory, and M. H. Fabricius. Bulges of Nearby Galaxies with Spitzer: The Growth of Pseudobulges in Disk Galaxies and its Connection to Outer Disks. *ApJ*, 697:630–650, May 2009. doi: 10.1088/0004-637X/697/1/630.

J. Frank, A. King, and D. Raine. *Accretion power in astrophysics.* 1992.

M. Gaspari, M. Ruszkowski, and S. P. Oh. Chaotic cold accretion on to black holes. *MNRAS*, 432:3401–3422, July 2013. doi: 10.1093/mnras/stt692.

K. Gebhardt, R. M. Rich, and L. C. Ho. An Intermediate-Mass Black Hole in the Globular Cluster G1: Improved Significance from New Keck and Hubble Space Telescope Observations. *ApJ*, 634:1093–1102, December 2005. doi: 10.1086/497023.

G. Hasinger. Absorption properties and evolution of active galactic nuclei. *A&A*, 490: 905–922, November 2008. doi: 10.1051/0004-6361:200809839.

G. Hasinger, T. Miyaji, and M. Schmidt. Luminosity-dependent evolution of soft X-ray selected AGN. New Chandra and XMM-Newton surveys. *A&A*, 441:417–434, October 2005. doi: 10.1051/0004-6361:20042134.

C. C. Hayward, P. Torrey, V. Springel, L. Hernquist, and M. Vogelsberger. Galaxy mergers on a moving mesh: a comparison with smoothed-particle hydrodynamics. *ArXiv e-prints*, September 2013.

M. Hirschmann, R. S. Somerville, T. Naab, and A. Burkert. Origin of the antihierarchical growth of black holes. *MNRAS*, 426:237–257, October 2012. doi: 10.1111/j.1365-2966.2012.21626.x.

M. Hirschmann, K. Dolag, A. Saro, S. Borgani, and A. Burkert. Cosmological simulations of black hole growth: AGN luminosities and downsizing. *ArXiv e-prints*, August 2013.

S. F. Hönig, M. Kishimoto, K. R. W. Tristram, M. A. Prieto, P. Gandhi, D. Asmus, R. Antonucci, L. Burtscher, W. J. Duschl, and G. Weigelt. Dust in the Polar Region as a Major Contributor to the Infrared Emission of Active Galactic Nuclei. *ApJ*, 771: 87, July 2013. doi: 10.1088/0004-637X/771/2/87.

P. F. Hopkins, G. T. Richards, and L. Hernquist. An Observational Determination of the Bolometric Quasar Luminosity Function. *ApJ*, 654:731–753, January 2007. doi: 10.1086/509629.

P. F. Hopkins, L. Hernquist, T. J. Cox, and D. Kereš. A Cosmological Framework for the Co-Evolution of Quasars, Supermassive Black Holes, and Elliptical Galaxies. I. Galaxy Mergers and Quasar Activity. *ApJS*, 175:356–389, April 2008. doi: 10.1086/524362.

F. Hoyle and R. A. Lyttleton. The effect of interstellar matter on climatic variation. *Proceedings of the Cambridge Philosophical Society*, 35:405, 1939. doi: 10.1017/S0305004100021150.

P. Hoyng. *Relativistic astrophysics and cosmology : a primer*. 2006.

J. Kormendy and L. C. Ho. Coevolution (Or Not) of Supermassive Black Holes and Host Galaxies. *ArXiv e-prints*, April 2013.

J. Kormendy and D. Richstone. Inward Bound—The Search For Supermassive Black Holes In Galactic Nuclei. *ARAA*, 33:581, 1995. doi: 10.1146/annurev.aa.33.090195.003053.

N. Lützgendorf, M. Kissler-Patig, E. Noyola, B. Jalali, P. T. de Zeeuw, K. Gebhardt, and H. Baumgardt. Kinematic signature of an intermediate-mass black hole in the globular cluster NGC 6388. *A&A*, 533:A36, September 2011. doi: 10.1051/0004-6361/201116618.

J. Magorrian, S. Tremaine, D. Richstone, R. Bender, G. Bower, A. Dressler, S. M. Faber, K. Gebhardt, R. Green, C. Grillmair, J. Kormendy, and T. Lauer. The Demography of Massive Dark Objects in Galaxy Centers. *AJ*, 115:2285–2305, June 1998. doi: 10.1086/300353.

A. Marconi, G. Risaliti, R. Gilli, L. K. Hunt, R. Maiolino, and M. Salvati. Local supermassive black holes and relics of active galactic nuclei. In T. Storchi-Bergmann, L. C. Ho, and H. R. Schmitt, editors, *The Interplay Among Black Holes, Stars and ISM in Galactic Nuclei*, volume 222 of *IAU Symposium*, pages 49–52, November 2004. doi: 10.1017/S1743921304001437.

N. J. McConnell and C.-P. Ma. Revisiting the Scaling Relations of Black Hole Masses and Host Galaxy Properties. *ApJ*, 764:184, February 2013. doi: 10.1088/0004-637X/764/2/184.

T. Miyaji, G. Hasinger, and M. Schmidt. Soft X-ray AGN luminosity function from it ROSAT surveys. I. Cosmological evolution and contribution to the soft X-ray background. *A&A*, 353:25–40, January 2000.

A. Muzzin, D. Marchesini, M. Stefanon, M. Franx, H. J. McCracken, B. Milvang-Jensen, J. S. Dunlop, J. P. U. Fynbo, G. Brammer, I. Labbe, and P. van Dokkum. The Evolution of the Stellar Mass Functions of Star-Forming and Quiescent Galaxies to z = 4 from the COSMOS/UltraVISTA Survey. *ArXiv e-prints*, March 2013.

I. D. Novikov and K. S. Thorne. Astrophysics of black holes. In C. Dewitt and B. S. Dewitt, editors, *Black Holes (Les Astres Occlus)*, pages 343–450, 1973.

E. Noyola, K. Gebhardt, M. Kissler-Patig, N. Lützgendorf, B. Jalali, P. T. de Zeeuw, and H. Baumgardt. Very Large Telescope Kinematics for Omega Centauri: Further Support for a Central Black Hole. *ApJ*, 719:L60–L64, August 2010. doi: 10.1088/2041-8205/719/1/L60.

A. Oemler, Jr. The structure of elliptical and cD galaxies. *ApJ*, 209:693–709, November 1976. doi: 10.1086/154769.

P. J. E. Peebles. *Principles of Physical Cosmology*. 1993.

A. K. Raychaudhuri, S. Banerji, and A. Banerjee. *General Relativity, Astrophysics, and Cosmology*. 1992.

C. Scannapieco, S. D. M. White, V. Springel, and P. B. Tissera. The formation and survival of discs in a ΛCDM universe. *MNRAS*, 396:696–708, June 2009. doi: 10.1111/j.1365-2966.2009.14764.x.

P. Schechter. An analytic expression for the luminosity function for galaxies. *ApJ*, 203: 297–306, January 1976. doi: 10.1086/154079.

P. Schneider. *Einführung in die extragalaktische Astronomie und Kosmologie*. 2006.

C. K. Seyfert. Nuclear Emission in Spiral Nebulae. *ApJ*, 97:28, January 1943. doi: 10.1086/144488.

N. I. Shakura and R. A. Sunyaev. Black holes in binary systems. Observational appearance. *A&A*, 24:337–355, 1973.

E. Shima, T. Matsuda, H. Takeda, and K. Sawada. Hydrodynamic calculations of axisymmetric accretion flow. *MNRAS*, 217:367–386, November 1985.

J. D. Silverman, P. Kampczyk, K. Jahnke, R. Andrae, S. J. Lilly, M. Elvis, F. Civano, V. Mainieri, C. Vignali, G. Zamorani, P. Nair, O. Le Fèvre, L. de Ravel, S. Bardelli, A. Bongiorno, M. Bolzonella, A. Cappi, K. Caputi, C. M. Carollo, T. Contini, G. Coppa, O. Cucciati, S. de la Torre, P. Franzetti, B. Garilli, C. Halliday, G. Hasinger, A. Iovino, C. Knobel, A. M. Koekemoer, K. Kovač, F. Lamareille, J.-F. Le Borgne, V. Le Brun, C. Maier, M. Mignoli, R. Pello, E. Pérez-Montero, E. Ricciardelli, Y. Peng, M. Scodeggio, M. Tanaka, L. Tasca, L. Tresse, D. Vergani, E. Zucca, M. Brusa, N. Cappelluti, A. Comastri, A. Finoguenov, H. Fu, R. Gilli, H. Hao, L. C. Ho, and M. Salvato. The Impact of Galaxy Interactions on Active Galactic Nucleus Activity in zCOSMOS. *ApJ*, 743:2, December 2011. doi: 10.1088/0004-637X/743/1/2.

V. Springel. The cosmological simulation code GADGET-2. *MNRAS*, 364:1105–1134, December 2005. doi: 10.1111/j.1365-2966.2005.09655.x.

V. Springel, S. D. M. White, G. Tormen, and G. Kauffmann. Populating a cluster of galaxies - I. Results at [formmu2]z=0. *MNRAS*, 328:726–750, December 2001. doi: 10.1046/j.1365-8711.2001.04912.x.

V. Springel, T. Di Matteo, and L. Hernquist. Modelling feedback from stars and black holes in galaxy mergers. *MNRAS*, 361:776–794, August 2005. doi: 10.1111/j.1365-2966.2005.09238.x.

L. Tornatore, S. Borgani, K. Dolag, and F. Matteucci. Chemical enrichment of galaxy clusters from hydrodynamical simulations. *MNRAS*, 382:1050–1072, December 2007. doi: 10.1111/j.1365-2966.2007.12070.x.

C. M. Urry and P. Padovani. Unified Schemes for Radio-Loud Active Galactic Nuclei. *PASP*, 107:803, September 1995. doi: 10.1086/133630.

S. Weinberg. *Gravitation and Cosmology: Principles and Applications of the General Theory of Relativity*. July 1972.

S. D. M. White and C. S. Frenk. Galaxy formation through hierarchical clustering. *ApJ*, 379:52–79, September 1991. doi: 10.1086/170483.

10 Acknowledgements

First of all I would like to thank my supervisor PD Dr. Klaus Dolag for the excellent teaching. Thank you for many fruitful discussions, for answering so many questions day-to-day and for giving me the great opportunity to work with the Magneticum Pathfinder simulations!
I would also like to thank Dr. Michaela Hirschmann, because it is also due to her that I got this very interesting topic about black holes. Thank you for all interesting and helpful comments during my whole Master's thesis!
Furthermore, I would like to thank Rhea-Silvia Remus, who also answered many questions and made a great job in supervising me. Her expertise on galaxies was very helpful, especially for the analysis of the structure and morphology of galaxies.
Next, I want to thank Prof. Dr. Andreas Burkert for giving me the opportunity to work in his group and for many useful suggestions and comments on my work during the last year.
I also want to thank Dr. Alexander Beck for many useful comments.
Since English is not my first language I would like to thank Stefan Striegler for correcting the language in this thesis.
I also want to thank my parents Anja Bachmann and Udo Bachmann for their support.
After all I want to say thank you to my boyfriend Daniel Steinborn for many comments, for helping me to learn C/C++ and python and for supporting me so much during my whole studies!

Erklärung:

Hiermit erkläre ich, die vorliegende Arbeit selbständig verfasst zu haben und keine anderen als die in der Arbeit angegebenen Quellen und Hilfsmittel benutzt zu haben.

München,